Tissue Diagnosis Probe Based on Stiffness Measurement Using Vision and Force Sensing Modalities

Li, Jichun

Awarding institution:
King's College London

Tissue Diagnosis Probe Based on Stiffness Measurement Using Vision and Force Sensing Modalities

by

Jichun Li

This thesis is submitted to Centre for Robotics Research,
School of Natural and Mathematical Sciences, King's College London,
for the degree of Doctor of Philosophy in Mechanical Engineering.
2013

Abstract

This thesis presents the creation of a novel tissue diagnosis probe based on the measurement of stiffness and force during mechanical tool-tissue interactions. The probe using force and vision sensing modalities was created to be used for tissue diagnosis in medical applications, especially for robot-assisted minimallyinvasive surgery (MIS) to provide the necessary sensing modalities to allow for haptic feedback. By employing the developed prototypes, estimations of the mechanical properties of ex-vivo human prostate tissues were conducted using the finite element analysis (FEA) method and the Newton-Raphson algorithm.A clinical study of prostate tumour identification has been carried out on ex-vivo prostate samples and a study onrobotic palpation using a second prototype developed as part of this projectand comparing it to manual palpation was conducted.

With the aim of measuring the indentation depth and the corresponding tissue reaction force simultaneously to obtain stiffness information,aprototype of a stiffness probe was constructedconsisting of a commercial digitalcamera and a force sensor. The effectiveness and sensitivityof the designedprobe was validatedthrough experiments on silicone phantomsand animal organs.Theresults showed that the probe could perform stiffness measurementsand localize tissue abnormalitieswhen indenting or sliding over the target surfaces.

In order to investigate the mechanical properties of ex-vivo human prostate using the developed probe, a portable sliding indenter robot integrating the probe and the Phantom Omni device was created. Based on force-displacement measurements of the probe-soft tissue interaction, inversefinite element analysis (FEA)andthegeneralised

Newton-Raphson algorithm were used to estimateunknown parameters including the shear modulus ofthe ex-vivo human prostate. The prostate was modelled as a nonlinear hyperelastic material (utilizing Arruda-Boyce model) inthe finite element modelling software package, ABAQUS 6.8-1. The results indicated that the proposed model can estimate the mechanical properties of the ex-vivo human prostate effectively.

With the aim of identifying the stiffness of normal and cancerous prostate tissue, the prostates of 26 male patients were examinedusing the developed sliding indenter robot. Threedimensional (3D) stiffness maps of ex-vivo human prostate were created.The stiffness maps were correlatedwith other clinical examinations including Magnetic Resonance Imaging (MRI), Digital Rectal Examination (DRE), histology and Ultrosound-guided biopsy. The proposedprobe proved to be a promising platform to distinguish between cancerous and healthy tissue in prostate andto discriminate pathological tissue variations.In addition, the results provided quantitative information for the diagnosis and localization of prostate cancer.

To ensure the proposed probe is suitable for MIS applications, a furtherprototype of the stiffness probebased on optic-fibreforce sensing replacing the commercial available force sensor was created.A studyon robotic palpation using the developed probe and comparing it tomanual palpation was conducted. The results indicated that robotic palpation was more effective than manual palpation conducted by experienced surgeons.

Acknowledgments

The work would not have been possible without the guidance and direction of my supervisors. First, I would like to show my gratitude to Professor Lakmal D Seneviratne and Professor Kaspar Althoefer. They have been strongly supportive of my work and consistently given me encouragement as well as creative and wise advises. Their vast knowledge in the field of robotics and automation are invaluable to the success of the project.

I would like to thank Professor Prokar Daspupta at Guys Hospital and his assistants Ben Challacombe, Pardeep Qumar and Elhage Oussama for their brilliant assistance and ideal sharing for this project.

I give my special thanks to my friends and colleagues, Hongbin Liu, Ketao Zhang, Min Li, Jelizaveta Zirjakova, Allen Jiang ,Wei Yao, Xiaojing Song, Vahid, Ali, Helger and Guowu Wei for the fun and supportive environment they created all these years.

I further acknowledge the financial support from the DHPA Scholarship.

I want to dedicate this thesis to my mum and dad. They are the best parents I could have asked for. They have been giving me the endless supports and devoting all their love to me since I was born. The faith and hope they have in me are the driving force of my life. This thesis is also dedicated to my wife, Hongyan Guo, and my son Ruixuan Li for the happiness and inspiration they have brought to me.

.

Contents

Contents

Nomenclature

The following is a list of the main symbols used in this thesis, together with a brief description of their significance

2D	:	Two dimension
3D	:	Three dimension
3DS	:	Three dimension scanning
CCD	:	Charge-coupled device
CMOS	:	Complementary metal–oxide–semiconductor
CT	:	Computed tomography
DAQ	:	Data acquisition
DC	:	Direct current
DOF	:	Degree of freedom
DRE	:	Digital rectal examination
DS	:	Displacement sensor
FDA	:	American Food and Drag Association
FE	:	Finite element
FEA	:	Finite element analysis
FS	:	Force sensor
LVDT	:	Linear variable differential transformer
MEMS	:	Microelectromechanical systems
MIS	:	Minimally invasive surgery
MRI	:	Magnetic resonance imaging
MP	:	Megapixel

PC : Personal computer

PCI : Peripheral Controller Interconnect

PVDF : Polyvinylidene fluoride

PSA : Serum-prostate specific antigen

PZT : Lead zirconate titanal

RMI : Rolling mechanical imaging

RMIS : Robot assisted minimally invasive surgery

RMS : Root mean square

SISI : Sliding indentation based stiffness image

SPSS Statistics: A software package used for statistical analysis. It is now officially named "IBM SPSS Statistics

TRUS : Transrectal Ultrasound

USA : United States of America

List of abbreviations

The following is a list of the main symbols used in this thesis, together with a brief description of their significance

C	:	The Neo-Hookean constant
C_{10}	:	The Mooney-Rivlin constants
C_{01}	:	The Mooney-Rivlin constants
C_i	:	The Arruda-Boyce constant
D	:	A temperature-dependent material parameter
d_{ca}	:	Diameter of Contact area
d_i	:	Indentation depth
D_{sc}	:	Diameter of contact area under FE simulation
e	:	Residual error
E	:	Elastic modulus
f	:	Reaction force
F_{FE}	:	The force-displacement curves of finite element analysis
F_M	:	The force-displacement curves of experimental data
F_M	:	The force-displacement curves of experimental data
hsi	:	Indentation depth under FE simulation
I_1	:	The first deviatoric strain invariants
I_2	:	The second deviatoric strain invariants
J_{el}	:	The elastic volume ratio
k_{th}	:	Number of iteration
P	:	The updated parameter
r	:	The radius of the indenter sphere head

U : Strain energy function

α_i : The Ogden constants

β_i : The Ogden constants

δ : Threshold valve

ε : Strain

λ_1 : The stretch ratios $\lambda_1 = 1 + \varepsilon$

λ_2 : The stretch ratios $\lambda_2 = \frac{1}{\sqrt{\lambda_1}}$.

λ_3 : The stretch ratios $\lambda_3 = \frac{1}{\sqrt{\lambda_1}}$.

λ_i : The principal stretches

λ_m : Locking stretch

λ_{lim} : The limiting chain stretch

λ_u : The stretch in the loading direction

μ : Shear modulus

μ_0 : First initial guess of shear modulus

μ_1 : Second initial guess of shear modulus

σ_0 : True stress

σ_n : Normal stress

ν : The Poissons ratio

List of definitions

The following is a list of the main definitions of medical terms used in this thesis. The definitions are mainly referenced from Wikipedia:http://en.wikipedia.org/wiki :

Brachytherap :	A form of radiotherapy where a radiation source is placed inside or next to the area requiring treatment
Deviatoric stress:	A condition in which the stress components operating at a point in a body are not the same in every direction. Also known as differential stress.
Expostulation :	The act of exposing to radiation or the condition of being so exposed.
Ex-vivo :	That which takes place outside an organism. In science, ex-vivo refers to measurements done in or on tissue in a non-living environment outside the organism.
Haptic :	The process of recognizing objects through touch. It involves a combination of somatosensory perception of patterns on the skin surface (e.g., edges, curvature, and texture).
Kinaesthetic :	The study of body motion, and of the perception (both conscious and unconscious) of one‘s own body motions.
Modality :	A particular sense
Palpation :	Physical examination operated by hand to feel the stiffness of target tissue or organ.
Parenchyma :	The functional parts of an organ in the body.
Specular :	Mirror-like

Tactile : The process of recognizing objects through touch.

List of Figures

List of Figures

List of Figures

List of Tables

Chapter 1

Introduction

1.1 Introduction

During the past few decades there has been a rapid technical advancement in the medical field. The revolution in information technology has allowed tremendous developments in the use of new medical technologies since the mid 20th century, driving the development of new methods and modalities in diagnosis and surgery. This chapter presents an overview of the research described in this thesis. First, a motivation of the research is presented. The aim and objectives regarding the development and application of a stiffness probe for soft tissue diagnosis are introduced. Contributions and major achievements made during the research are summarised. The overall structure of this thesis is provided.

1.2 Motivation

Minimally invasive surgery (MIS) is one of the latest trends now widely used in different types of surgery on the brain, nerves, heart and prostate. MIS is a surgery performed through several small holes (typically with 5mm to 15mm) employing endoscopic or laparoscopic cameras and specialised surgical tools, Figure 1.1. Since a large incision needs to be created to access internal organs directly, traditional open surgery is highly invasive, with many disadvantages for the patient. In contrast, MIS offers distinct advantages in many respects, including the reduction of blood loss, tissue trauma, discomfort, recovery time and hospitalisation costs (Fuchs 2002). Nevertheless, MIS is usually faced with difficulties such as a limited view of the surgical area, a relatively long surgeon training period, lack of haptic feedback (“sense of touch”) and difficulties in handling the surgical tools due to the inversion of hand movements, when operating through a trocar port as well, and tremors (Tendick and Cavusoglu 1997). In

order to overcome these issues, computer controlled robots have been introduced in the medical field to improve the capabilities of

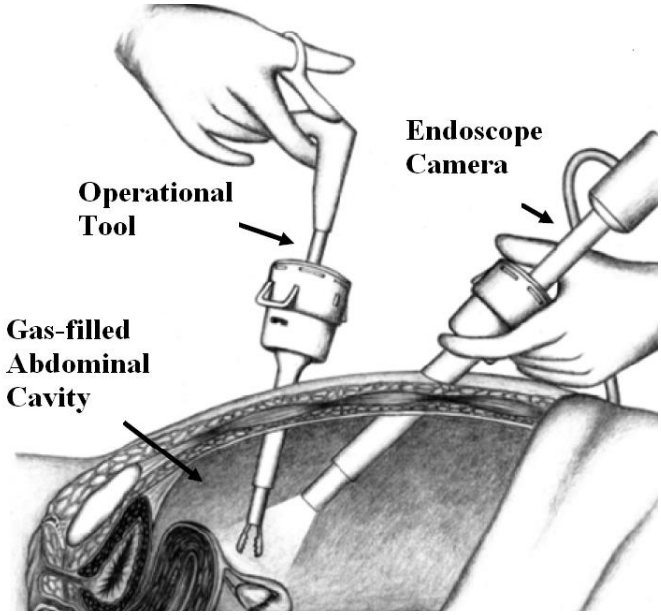

Figure 1.1: Traditional Minimally Invasive Surgery (Laparoscopic Surgery) (by Puangmali P, et al.)

surgeons when performing complex surgical procedures. The most well-known surgical robot appearing about a decade years ago is the da Vinci™ Surgical System (Intuitive Surgical, Inc. (Guthart and Salisbury 2000)), Figure 1.2. Such a surgical robot is advantageous in many aspects, including enhanced 3D vision, high distal dexterity, motion scaling and tremor filtering. However, while these robots provide significant improvements over traditional MIS, the surgeon does not receive any haptic feedback when performing surgery using such a system. The lack of the haptic feedback is still one of the most significant drawbacks, potentially leading to a reduced surgical outcome and the failure to identify tumours hidden beneath the tissue surface (Deml, Ortmaier et al. 2005).

Palpation is often used during open surgery or other medical applications for diagnosis since it provides clinicians rich information on the mechanical properties of soft tissue such as stiffness, mass distribution and texture. Since there is usually a

notable difference in compliance between benign and malignant tissue (a malignant tumour is typically stiffer than the surrounding parenchyma (M.Hossenini 2006)), clinicians often rely on palpation to differentiate benign tissues and malignant tissues without the need of determining its histology. Palpation is widely used in different

Figure 1.2: The da Vinci S HD Surgical System. (Intuitive Surgical, Inc.)

(a) (b) (c)

Figure 1.3: Clinical palpation. (a) Throat cancer diagnosis ((Asiancancer.com)) (b) Breast cancer diagnosis (Gaumard.com) (c) Recto-abdominal Palpation ((Woodall 1926))

circumstances, Figure 1.3, since it can give quick qualitative information without additional tools. However, it highly depends on the expertise of the clinician, and cannot provide quantitative data of the mechanical properties of soft tissue.

In the medical field, a wide range of imaging modalities, such as magnetic resonance imaging (MRI), computed tomography (CT) imaging, x-Ray and ultrasound imaging are used to detect the existence and location of cancer in the human body (Forstner R 1995; Sylvain Jaume 2003; Gou-Shiang Lin 2008). Although these methods are much preferred to invasive biopsies by clinicians and patients for cancer diagnosis, there are still some limitations. For example, tumours of the prostate or breast may be invisible or only partly visible in standard ultrasound examinations (Choye P.L. 1995; Carra B.S. 1997). In addition, due to low image resolution (e.g.in the case of ultrasound), it can be problematic to locate small tumours accurately. Furthermore, since the aforementioned techniques are generally used to identify tumour locations pre-operatively, it is difficult to accurately register the pre-operative images to the intra-operative tumour locations due to the deformability of soft tissue and/or tissue movement during the operation. To illustrate this, the location of lung tumours can be easily detected by using CT before an operation. However, during surgery the lung volume shrinks because the internal pressure decreases when a surgeon makes an incision to the lung. As a result, the tumours within the lung also shift with the shrinkage of the lung volume. Thus, during the surgery it is impossible to locate the tumour accurately based on the pre-operative images. Furthermore, some of these imaging methods (particularly in the case of MRI) are very expensive.

An endoscope camera provides direct visual information of the surface of soft tissue and is a convenient tool for examining cancer at the surface of soft tissue. However, endoscope cameras do not provide any information of the cancer below the tissue surface.

The development of a haptic feedback system would allow remote and quantitative diagnosis of soft tissues. Haptic feedback systems are employed in

biomedical applications to measure tissue stiffness. Since the malignant tissue such as a tumour is stiffer than the surrounding healthy tissue, it is reasonable for a surgeon to identify abnormal tissue using a stiffness measurement instrument.

Prostate cancer is the commonest diagnosed male cancer. There is an increasing prevalence of prostate cancer in elderly men in recent years (American Cancer Society 2011). In most cases, Digital Rectal Examination (DRE) and Serum-prostate specific antigen (PSA) determination comprise the most common methods for diagnosis. Since most prostate tumours are accessible from the posterior, and cancer tissue is harder than normal tissue, prostate cancer is detectable using a DRE, which means that the clinician inserts a gloved and lubricated finger into the patient's rectum, where a malignancy can be detected by searching for a stiffer area (Ahn BM 2010). Although DRE is low risk, promptly available and cost effective, the results of a DRE are not quantitative. In order to obtain a more accurate result, tissue diagnosis probed based on stiffness measurement have been developed and advanced in recent years. Indentation, performed by applying a deformation and observing the reaction forces of the tissue with the stiffness probe, is the most common approach to measure the variation in stiffness of prostate tissues and other soft tissue organs.

Mechanical property identification of ex-vivo prostate tissue based on the probe-prostate indentation approach is important for many applications including the modelling and control of surgical tool interactions during surgery, development of virtual reality surgical environments for simulation and training , and the detection and diagnosis of tumours. In recent years, the inverse finite element method has been widely used to identify soft tissue mechanical properties. Tests performed on ex-vivo organs of human beings is an important and necessary step for the evaluation of the performance

of newly developed medical devices. Only when the devise shows its feasibility in ex-vivo conditions, it is possible to explore its use during the real surgery.

This thesis presents a novel tissue diagnosis probe based on stiffness measurement using force and vision modalities. The probe-soft tissue interaction on ex-vivo human prostate tissue is investigated using the proposed probe. It will also be shown that proposed probe can be integrated with MIS instruments.

1.3 Aim and Objectives

The aim of this research is to create and study a probe for the stiffness measurement of soft tissue, and specifically to identify ex-vivo prostate tissue properties by using the proposed probe, and to apply it to procedures and systems as part of medical applications, such as interactive simulation for training, diagnosis of tumours inside of soft tissue. A comparative study of the proposed probe with manual palpation will also be investigated.

The main objectives of the research are:

a) To create a first generation tissue diagnosis probe using force and vision sensing, measuring the indentation depth and reaction force simultaneously to obtain an estimation of stiffness of scanned soft tissue.

b) To model tool-soft tissue interactions and to estimate parameters of ex-vivo human prostate samples using finite element analysis (FEA) and FEA.

c) To apply an optic-fibre sensing technique for force sensing advancing beyond earlier systems using commercially available force sensor to miniaturize the probe for use in MIS.

d) To validate the proposed probe through comparative study benchmarking against current clinical techniques.

1.4 List of Contributions

The following is a summary of the major contributions of this research:

1. The first contribution is the creation of a stiffness measurement probe for soft tissue examination based on the measurement of indentation depth and force during mechanical tool-tissue interactions. The proposed probe is based on force and vision measuring modalities. A first generation prototype made from a commercially available force sensor and digital camera was designed, developed and validated on simulated soft tissue and animal organs (Chapter 3).
2. The second contribution is the the creation of a portable, passive sliding indenter robot for three-dimensional scanning (3DS) of ex-vivo human prostate tissue. The device consists of a six degrees of freedom (DOF) passive robotic arm (Phantom Omni), a data acquisition system, and a stiffness probe for force and stiffness measurements (Chapter 4, 5 and 6).
3. The third contribution is the modelling of tool-tissue interactions using FEA and inverse FEA with the Newton-Raphson Method to identify mechanical properties of ex-vivo human prostate tissue (Chapter 4).

4. The fourth contribution is a validation study comparing the approach to current clinical techniques and the characterization of normal and malignant ex-vivo prostate tissue (Chapter 5).
5. The fifth contribution is the creation of a second generation prototype which has been miniaturized by integrating an optic-fibre force sensor, created as part of this research and replacing the commercial force sensor. The effectiveness of the proposed method for tissue abnormality is validated through a comparative study with manual palpations (Chapter 6).

1.5 Publications

The work discussed in this thesis was summarized in the publications listed below.

Journal Papers

1. Hongbin Liu, Jichun Li, Xiaojing Song, Lakmal D. Seneviratne, Kaspar Althoefer, "Rolling Indentation Probe for Tissue Abnormality Identification during Minimally Invasive Surgery ", **IEEE Transactions on Robotics**, vol. 27, no. 3, pp. 450-460, June 2011.
2. Jichun Li, Kaspar Althoefer and Lakmal D. Seneviratne., "Parameter Estimation using inverse finite element analysis of ex-vivo prostate", to be submitted to **IEEE Biomedical Engineering**.
3. Jichun Li, Lakmal D. Seneviratne and Kaspar Althoefer., "Stiffness probe using force and vision sensing for tissue abnormality identification", to be submitted to **Medical Engineering and Physics**.

4. Jichun Li, Kaspar Althoefer and Lakmal D. Seneviratne., "Mechanical properties of ex- vivo prostate tissue using rolling indenter robot ", to be submitted to **Part H: Journal of Engineering in Medicine.**

5. Jichun Li, Lakmal D.Seneviratne, Kaspar Althoefer, "Experimental evaluation of sliding indentation with manual palpation", to be submitted to **Medical & Biological Engineering & Computing.**

Conference Papers

6. Jichun Li, Hongbin Liu, Kaspar Althoefer and Lakmal D. Seneviratne.,"A Stiffness Probe Based on Force and Vision Sensing for Soft Tissue Diagnosis"., *34th Annual International IEEE /EMBS Conference,EMBC 2012*, San Diego,USA, August 2012. 944-947

7. Jichun Li, Hongbin Liu, Kaspar Althoefer and Lakmal D. Seneviratne.,"A Stiffness Probe for soft tissue abnormality identification during laparoscopic surgery", *World Automation Congress,WAC 2012*, Puerto Vallarta, Mexico, June 2012. 1-6.

8. Jichun Li, Jelizaveta Zirjakova, Kaspar Althoefer and Lakmal D.Seneviratne.,"A Passive Robotic Platform for 3D Mechnical Imaging of Soft tissue", *IEEE/ASME International Conference on Reconfigurable Mechanisms and Robots ,REMAR 2012*,Tianjin,China, July 2012, 477-485.

9. Jichun Li, H Liu, P Dasgupta, B Challacombe, L.D. Seneviratne and K Althoefer.," Clinical Study of Prostate Tumour Identification Using A Rolling Indenter Robot", *5th Hamlyn Symposium on Medical Robotics, 2012.* London, UK, July 2012.

10. Min Li, Hongbin Liu, Jichun Li, Lakmal D. Seneviratne and Kaspar Althoefer. "Tissue Stiffness Simulation and Abnormality Localization using Pseudo-Haptic Feedback". *IEEE Int. Conf. Robotics and Automation, ICRA2012,* Minnesota, USA, May 2012. 5359-5364.

11. Hongbin Liu, Jichun Li, Qi-ian Poon, Lakmal D.Seneviratne and Kaspar Althoefer., "Miniaturized Force-Indentation Depth Sensor for Tissue Abnormality Identification during Laparoscopic Surgery", *IEEE International Conference on Robotics and Automation, ICRA2010,*Anchorage,AK, 2010. 3654-3659.

12. J Li, H Liu, P Dasgupta, B Challacombe, L.D. Seneviratne and K Althoefer.," Results of Kidney Lesion Experiments with Haptic Probe", *the 59th annual meeting of Society of Academic & Research Urology, SARS 2011*., Dublin, Ireland, 2011, 166.

13. Pardeep Kumar, Jichun Li, Hongbin Liu, Ben Challacombe, Ashish Chandra, Lakmal D. Seneviratne, Kaspar Althoefer and Prokar Dasgupta., "Prostate Tumour Identification Using a Force-Sensitive Rolling Indentation Probe", *the 26th annual meeting of Engineering and Urology,EUS2011.* Wachington DC, USA. 2011. abstract is cited by Journal of Endourology. A45-A46.

14. Dinusha Zbyszewski, Benjamin Challacombe, Jichun Li, Lakmal D.Seneviratne, Kaspar Althoefer, Prokar Dasgupta and Declan Murphy .,"A Comparative Study Between an Improved Novel Air-Cushion Sensor and a Wheeled Probe for Minimally Invasive Surgery", *27th World Congress of Endourology. WCE2009*. Munich, Germany.2009. 1155-1159.

1.6 Structure of the Thesis

This PhD thesis consists of 7 chapters. The thesis structure is shown in a diagrammatic form in Figure 1.4. A summary of each chapter is provided below:

Chapter 1: Introduction

This chapter gives the overview of the thesis, including the motivation, the aim and objectives of the research, a list of contributions and the overall structure of the thesis.

Chapter 2: Literature Survey

This chapter reviews state-of-the-art stiffness sensing related technologies including medical robotics, haptic sensing and stiffness sensing, and modelling and finite element modelling for soft tissue in biomedical applications.

Chapter 3: A Stiffness Probe Based on Force and Vision Sensing Modalities

This chapter presents the design, model, calibration and validation of a first generation stiffness probe that is capable of measuring the indentation depth as well as the tissue reaction force at the same time.

Chapter 4: Parameter Estimation of Ex-vivo Human Prostate Tissue Using Inverse Finite Element Analysis and Newton-Raphson Method

This chapter describes the modelling of tool-tissue interaction using FEA and the estimation of mechanical properties of ex-vivo human prostate tissue using inverse FEA with the Newton-Raphson method. This chapter also presents a portable, passive robotic platform for measuring the deformation during probe-prostate interactions. The results show that the proposed model can estimate the stiffness of the ex-vivo human prostate effectively.

Chapter 5: Clinical Study of Ex-vivo Prostate Tissue Mechanical Characteristics for Prostate Tumour Identification

This chapter presents the working principle of the developed test rig, sliding for the three dimensional scanning of ex-vivo prostate tissue, for evaluating mechanical properties and geometry in ex-vivo conditions. A total of 126 sites from 21 radical human prostate samples were analysed using the developed test rig. The estimated stiffness from 6 regions was separated into normal and cancerous tissues according to pathological information. A three-dimensional sliding indentation stiffness image was also generated using the sliding indenter robot. Sensitivity, specificity, accuracy, and predictive value for data from stiffness image, MRI, DRE and transrectal ultrasound (TRUS) biopsy were calculated. Results show that the highest sensitivity (76.2%) and accuracy (62.7%) can be achieved from the biopsy. It was also observed that stiffness image has a higher sensitivity (45.9%) and accuracy (61.5%) than both DRE (34.8% and 50.0%, respectively) and MRI (34.9% and 58.7%, respectively).Results from the ex-vivo tests demonstrate the capability of the device to separate cancerous tissue from normal tissue based on stiffness and force measurements.

Chapter 6: Development and Validation of a Second Generation Probe Using Optic-Fibre Techniques

This chapter presents development of a second generation probe based on an optic-fibre force sensing techniques, which ensures the probe has the potential to be used in MIS. A comparative study of stiffness image with manual palpation by experienced clinicians is conducted in this chapter. Experimental results are given demonstrating that the stiffness image approach using the developed probe is more effective than manual palpations in this study.

Chapter 7: Conclusions and Future Work

In this chapter, conclusions are given and suggestions for future work are discussed.

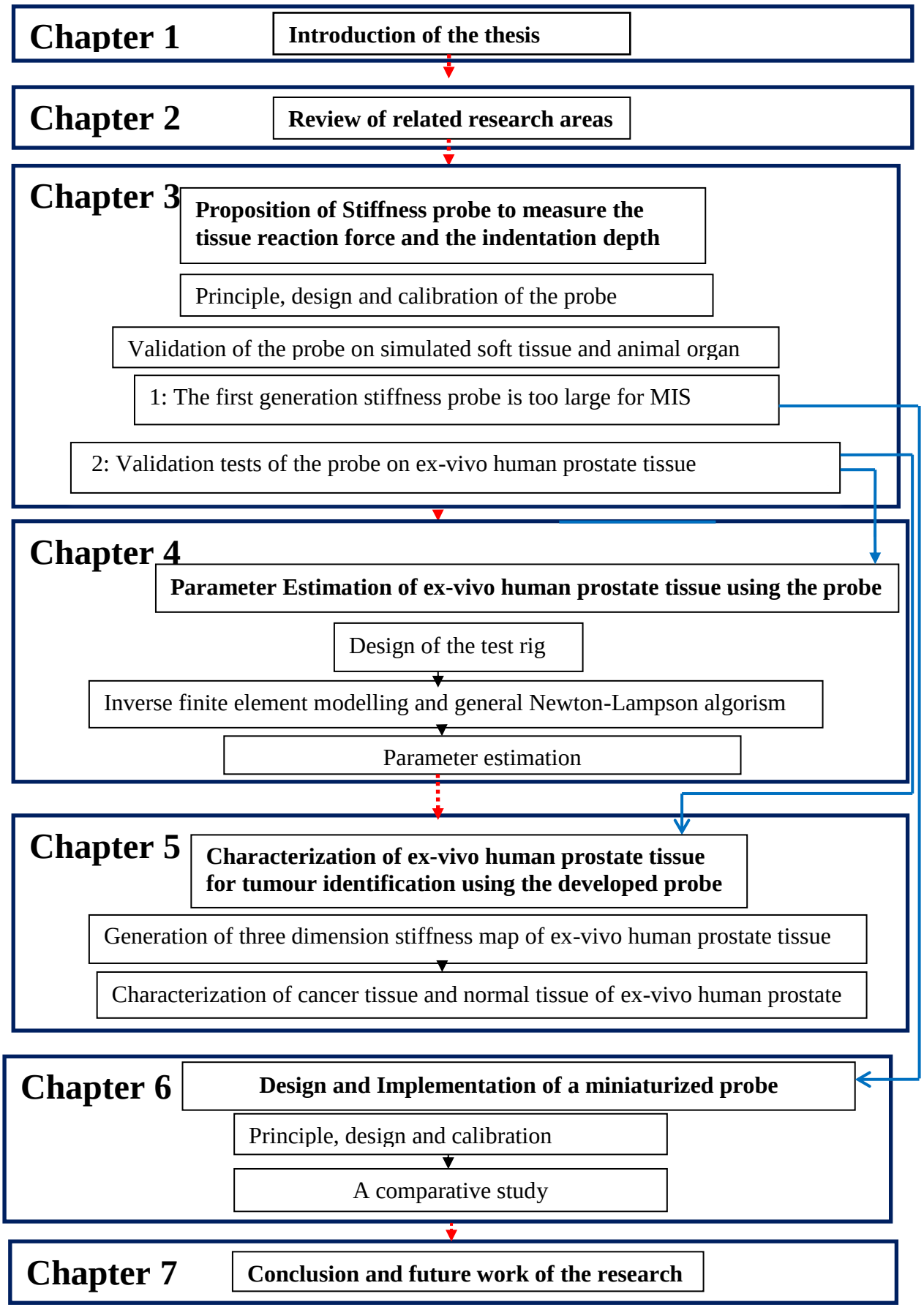

Figure 1.4: Structure of the thesis

Chapter 2

Literature Survey

2.1 Introduction

Chapter 1 establishes the technical areas of this research and highlighted its multidisciplinarity. Due to the broad range of technical areas encompassed, it is necessary to conduct a thorough literature review of previous research work related to the specific objectives of this project. First, surgical robots for MIS are reviewed. Next, haptic and stiffness measurement techniques for biomedical applications are discussed. Finally, modelling and finite element techniques for biological soft tissues are summarised.

2.2 Surgical robots for MIS

A Surgical robot can be defined as a robot designed to assist surgeons in carrying out delicate surgical procedures rather than an intelligent machine to replace humans in the operating theatre (Davies 2000; Rodriguez y Baena 2006). Surgical robots are widely used to assist the surgeons in performing a variety of minimally invasive surgeries including prostate surgery (Davies, Hibberd et al. 1989; M. Wolfram and Kramer 2003), bladder surgery (D. W. Miller 2004; J. Heemskerk 2005), orthopedic surgery (Love, Pillai et al. 2008), neurosurgery (Moore and Newell 2005), biopsy (Stoianovici, Cleary et al. 2003), knee replacement surgery (Jakopec, Rodriguez y Baena et al. 2003) and brachytherapy (Jain, Deguet et al. 2007). Surgical robots have shown distinctive advantages in carrying out various surgical tasks with high accuracy and repeatability while providing surgeons with enhanced visual feedback.

Most of the first generation of surgical robots are designed as positioning devices to guide surgical tools to the desired target in an anatomy or an operation site (Davies 2000). Although intended to be used as an industrial robot, the Puma was the first robot used as a stereotactic frame for neurosurgery in 1985 (Kwoh, Hou et al. 1988;

Davies 2000). Since then, surgical robots have been increasingly used in many critical surgical procedures listed below.

'Active' or automated robots are developed to follow a pre-operative plan based on pre-operative imaging (e.g. MRI or CT) and then to perform the operations without interventions of the surgeon. The *PROBOT* was the first surgical robot developed for urological surgery (Davies, Hibberd et al. 1989). Based on a well-defined preoperative planning and computer-guided control strategy, the robot achieved automatic removal of prostate without input from the surgeon. Other examples of automated robots are the *ROBODOC* (Integrated Surgical Systems Inc. USA), Caspar (Orto MAQUET, Germanay) and the *Minerva neurosurgical robot* (University of Lousanne, Switzerland). The *MiniAture Robot for Surgical procedures (MARS)* is a cylindrical 5×7 cm3, 200-g, six-degree-of-freedom parallel manipulator developed for spine and trauma surgery (Burman 2003). This robot is directly mounted on the patient's bony structure near the surgical site. The robot is designed to operate in a semi-active mode to precisely position and orient a drill or a needle in various surgical procedures.

'Passive' robots which are operated in a master-slave mode become more prevalent (Davies 2000), due to the complexity of soft tissue surgery and for those without image guidance. For these robots, the action of the robotic manipulators is remotely controlled by a surgeon. Visual feedback is achieved by endoscopic sight. The most well-known examples of these types of systems in recent years are the Da Vinci™ Surgical System (Intuitive Surgical, Inc.) and Zeus™ Surgical System. The DaVinci is a master-slave tele-manipulator with two robot arms controlling endoscopic instruments and a third arm guiding a laparoscopic camera. The Da Vinci system also incorporates "endo-wrists" to provide the surgeon with two extra degrees of freedom for cutting and suturing operations at the point of intervention (Dario, Hannaford et al. 2003; Taylor

and Stoianovici 2003). The surgeon operates the robot from a console with two hands controls steering the tools, a pedal and voice controls for the laparoscopic arm. The surgeon is completely separated from the patient receiving 3D feedback from a camera environment. Compared with traditional non-robotic MIS, the Da Vinci system is advantageous in many aspects, including enhanced 3D vision, high distal dexterity, motion scaling and tremor filtering (Dario, et al., 2003). These advances result in improved ergonomics and also allow complex surgical procedures such as coronary artery bypass grafting (Tabaie, Reinbolt et al. 1999) and mitral valve repair (Murphy, Miller et al. 2006).

With the aid of intra-operative imaging techniques such as CT and MRI (G.Dogangil 2010), the surgeon is able to view the operation site and track the instruments in real time. Image guided surgical robots are adapted to perform more accurate operations such as inserting a needle (Frasson, Parittotokkaporn et al. 2008), cutting and drilling into bone (Shoham, Burman et al. 2003).

The *AcuBot* developed for radiological percutaneous interventions is a six-degree-of-freedom robot using intra-operative fluoroscopy or CT images for image-guided steering. The *AcuBot* can manipulate a needle to conduct delicate procedures such as needle biopsy, radio frequency ablation and cryotherapy with high accuracy (Stoianovici, Cleary et al. 2003). The *Minerva neurosurgical robot* was designed to work autonomously with CT image guidance and conduct tool positioning and insertion. The system has 5 degrees of freedom and is mounted on a stereotactic frame (Kevin Cleary 2006). Another example is the *Neuromate* (Integrated Surgical Systems Inc., USA), which is a degree of freedom passive robot developed for use with CT image guidance. The *Neuromate* was the first image guided neurosurgical robot approved by the American Food and Drug Association (FDA) (Kevin Cleary 2006).

MRI is a recently introduced medical imaging modality. The first surgical robot for use with MRI was developed by Masamune et al. (K. Masamune 1995) at the University of Tokyo in Japan. The robot has 6 degrees of freedom and is actuated by ultrasonic motors. The optical encoders attached to the driven shafts of the motors provide positional feedback. The *MrBot* is another example of an intra-operative MRI image guided robot, which is designed to precisely insert a biopsy needle to the prostate gland. The body of this robot is exclusively constructed from the MRI compatible materials such as plastics, ceramics and rubbers. The robot is actuated using the pneumatic stepper motors (PneuStep)(Stoianovici, Song et al. 2007).

To improve the dexterity of an instrument's distal tip, a number of highly actuated, snake-like robots were developed by the research groups throughout the world (Salle, Bidaud et al. 2004; Simaan, Taylor et al. 2004; Degani, Choset et al. 2006; W Wei 2006; Xu and Simaan 2006; J. Shang 2011). The 'i-Snake' robot which is being developed at Imperial College London aims to extend the use of MIS techniques, employing a flexible, snake like structure, and incorporating state of the art imaging and intuitive manipulation technologies. The 'i-Snake' robot uses fully articulated joints powered by modular, micro-motors, with multiple sensing mechanisms and imaging tools at its 'head', to extend the vision and dexterity of the surgeon (J. Shang 2011).

With the aim of overcoming the limitations of camera vision, an implantable 5-DoFs imaging system is integrated into an endoscope and is able to provide the surgeon with stereoscopic visualisation to improve their performance (Miller, Allen et al. 2004). A mobile *in-vivo* robot was developed at the University of Nebraska, USA (Rentschler, Dumpert et al. 2006). The device is composed of an adjustable focus camera, a biopsy forceps for removing tissue samples and two independently drivable wheels.

In the future, it is expected that surgical robots will be more and more popular in modern surgery. However, while the current medical robots provide significant improvements over traditional MIS, the surgeon does not receive any haptic feedback from the operating site when performing surgery using as urgical robot. The lack of the haptic feedback could lead to a reduced surgical outcome and the failure to identify tumours hidden beneath the tissue surface. The development of haptic sensing systems could help the clinicians feel stiffness of soft tissue and measure the variation.

2.3 Haptic and Stiffness Measurement Technologies for Biomedical Applications

2.3.1 Haptic Measurement Technologies for Biomedical Applications

Haptic refers to the "sense of touch" by the human hand. The sense of touch is one of the most complicated human sensed; it includes sensations from the skin and from the muscles (D. De. Rossi 2006). The sense of touch from the skin is referred as the tactile sensing and the muscle sense of hand is referred as sense of force or kinaesthetic information (Okamura, Simone et al. 2004). The latter allows the determination of characteristics such as stiffness, mass distribution, texture, temperature and shape of objects in contact. It is readily available during open surgery and is only partially available during traditional laparoscopic procedures, enabling the surgeon to feel stiffness and roughness of tissues, classify mechanical tissue properties and evaluate anatomical structures such as nerves, vessels and ducts. The sense of touch plays an important role in the accuracy and efficiency of surgical procedure (Wagner, Stylopoulos et al. 2002; Bethea Okamura et al. 2004; Kitagawa Dokko et al. 2005; Tsagarakis, Gray et al. 2006).

Over the past years, many research groups have been working on the design and development of haptic systems using force feedback for tissue diagnosis during minimally invasive surgery. Current-based sensing methods were investigated with a specially designed laparoscopic grasper (G. Tholey 2004). Strain gauges were applied in the design of graspers in MIS for measuring force and tissue properties (Bicchi, Canepa et al. 1996) (B Hannaford 1998; J. D. Brown 2003; G. S. Fischer 2006). Prasad et al. from Johns Hopkins University have developed a 2-DOF force sensing sleeve which can be integrated with a laparoscopic device (S. K. Prasad 2003). Recent advances in the microelectromechanical systems (MEMS) technology allowed the development of force sensing instruments for MIS (G. F. Buess 2000; P. J. Berkelman 2000; Rebello 2004). A capacitive silicone pressure sensor with low temperature sensitivity was presented by Lee and Wise(Lee and Wise 1982). Fibre-optic-based sensing has also been proved to be a very promising technology for force measurement in MIS due to small sensing structures, high sensitivity and compatibility with magnetic resonance (Hirose and Yoneda 1990; Sutherland, McBeth et al. 2003; Lavoie, Ionescu et al. 2004; Polygerinos 2010; P. Puangmali 2008). A series of fibre optic sensors applied in MIS have been developed at Centre for Robotics Research, King's College London (D. Zbyszewski 2008; P. Puangmali 2008; P. Puangmali 2008; K. Althoefer 2010; Polygerinos 2010).

Another important type of haptic feedback is tactile sensing. Tactile sensing is the process of recognizing objects through touch. It involves a combination of somatosensory perception of patterns on the skin surface (e.g. pressure, curvature, and texture).A surgeon if provided with tactile sensing is able to detect surface textures and pressure distribution across the contacting area. Rather than measuring a single point force, tactile sensors are usually capable of measuring distributed forces over the

sensing surfaces concurrently. With the aid of tactile sensors, the surgeon is able to acquire valuable palpation information for the identification of tumours (Egorov, Ayrapetyan et al. 2006), classifying breast lesions (Miller, Peine et al. 2007) and identifying arteries (Beasley and Howe 2002).

A variety of materials and techniques have been used in the field of tactile sensing. To date, advances with regard to tactile sensors have been made using piezoelectric material (Hayward and Cruz-Hernandez 2000; G. Tholey 2004), shape memory alloys (Kontarinis, Son et al. 1995), electromagnetic actuators (Fukuda, Morita et al. 1997; Wagner, Lederman et al. 2002), pneumatic actuator (Caldwell, Tsagarakis et al. 1999; Moy, Wagner et al. 2000), and silicone-based balloon actuators (Culjat, King et al. 2008).

Based on the capacitance sensing principle, tactile array sensors have been developed to help the surgeon to detect arteries and tumors within soft tissues (Lee and Wise 1982; Suzuki, Najafi et al. 1990; R. D. Howe 1995). Advances in the piezoelectric technology allowed the development of tactile sensors for MIS (Dargahi, Parameswaran et al. 2000; Dargahi, Najarian et al. 2007; Sokhanvar, Packirisamy et al. 2007; Qasaimeh, Sokhanvar et al. 2009). Instead of using passive force sensing elements, another type of tactile sensors comprising a vibration unit is capable of measuring the dynamic response of soft tissues. In (E. Petter 1996; I. Baumann 2011), prototypes of the vibro−tactile sensors were used to examine various human tissues. The results showed that the sensor can help differentiating between healthy and unhealthy tissues.

2.3.2 Stiffness measurement technologies for biomedical applications

The sense of touch is also employed in biomedical applications to measure tissue stiffness. A change of tissue stiffness is one of the generally known characteristics in many tissue pathologies such as fibrosis, edema, and breast, liver and

prostate cancer (Mridha M 1986; Garra BS 1997; McKnight AL 2002; Brown 2003; Brown, Rosen et al. 2003; Davis AM 2003; Phipps and T.H.J. Yang 2005; Phipps, Yang et al. 2005). Since the stiffness of malignant tissue such as a tumour is typically higher than the surrounding healthy tissue, a surgeon can use the measurement of stiffness to identify abnormal tissue regions.

Stiffness is defined by the resistance of an rigid body to deformation by an external force (Nobuyuki Tanaka 2011). Young's modulus, which is defined as the ratio of stress over strain in a region, is widely used to describe the stiffness of soft tissue. Rather than only measuring the imparted force, both the deformation and indentation force need to be measured simultaneously to measure the stiffness of soft tissue. Many research groups have worked on measuring tissue stiffness using a variety of modalities including strain gauge-, capacitive-, piezoelectric-, ultrasound- , camera-, vibration-, and optic fibre-based sensing.

The strain gauge is usually bonded to a flexible structure. When a force causes strain to the flexible structure, the electrical resistance of the strain gauge will change, allowing the measurement of the applied force. Figure 2.1 shows an arthroscopic indentation probe based on a strain gauge sensing approach. The probe was used for the measurement of stiffness of articular cartilage in the human knee joint (T. Lyyra 1999). The probe consists of a stainless steel measurement rod joined to a handle. A cylindrical indenter (Ø1 mm, 300mm length) is positioned in the centre of an inclined reference plate of the distal end of the rod. During indentation, the rod is pressed against the cartilage surface at a constant force while the cylindrical indenter, which is perpendicular to the cartilage surface, generates a constant deformation of the tissue. The pressing force, which is monitored and kept to a predefined value, is measured by a strain gauge construction. The force generated by the tissue due to the constant

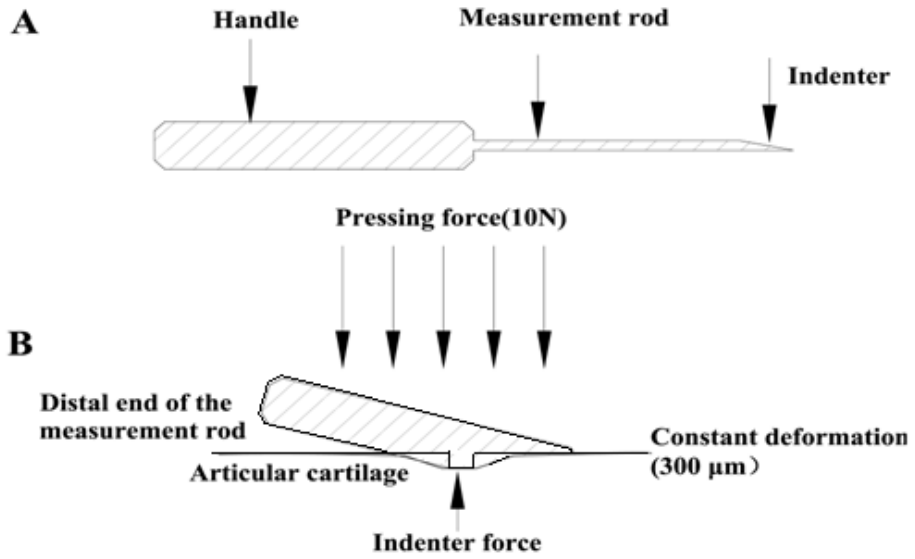

Figure 2.1: (A) the arthroscopic indentation instrument. (B) Distal end of the measurement rod with a cylindrical indenter is positioned in the centre of an inclined reference plate. The indenters were used to impose a constant deformation of bovine humeral head articular cartilage in situ (T. Lyyra 1999).

deformation produced by the indenter is measured by a strain gauge element. The experiments conducted showed that the instrument was capable of detecting the stiffness of the tissue. However, for strain gauge–based sensing, there is always a tradeoff between the stiffness of the flexible structure and the sensitivity of the measurement (Craig 2003).

Capacitive sensing is known as the most effective means for detecting extremely small deflections of structures among several sensing concepts (P. Puangmali 2008). A stiffness probe which employs MEMS capacitive sensing membranes was proposed by P. Peng et al (P. Peng 2010). The proposed approach utilise capacitive measurements form multiple nodes on the sensors and estimates tissue stiffness by manipulating the capacitive data from these nodes. However, the capacitive sensor is usually limited to applications that require precise measurements over a small range of structural deformations and is temperature dependent.

Piezoelectric materials have the potential to be used for effective force and stiffness sensing. Piezoelectric material is very sensitive to generate high resolution voltage when compressed. It can be used to detect very small deformations. Furthermore, it can work without a supply of electrical power.

A cantilever sensor that can self-excite and self-detect tissue stiffness measurements was developed (Szewczyk 2006). The instruments were facilitated by adding a sensing lead zirconate titanale (PZT) layer to the bottom side of the stainless steel of a piezoelectric cantilever, Figure 2.2. The piezoelectric cantilever is a sandwich of a piezoelectric layer, a non-piezoelectric layer, and a second piezoelectric layer. The top PZT layer is the driving layer and the second PZT layer is the sensing layer. Applying a DC voltage across the driving PZT layer causes the piezoelectric cantilever to bend. The resultant bending stress in the sensing PZT layer generates a piezoelectric voltage across the sensing PZT layer that rises rapidly to a maximum before it decays with time. The maximum induced voltage is used to measure the axial displacement of the piezoelectric cantilever. With its force generation and displacement sensing capability, the cantilever can measure the stiffness of tissues.

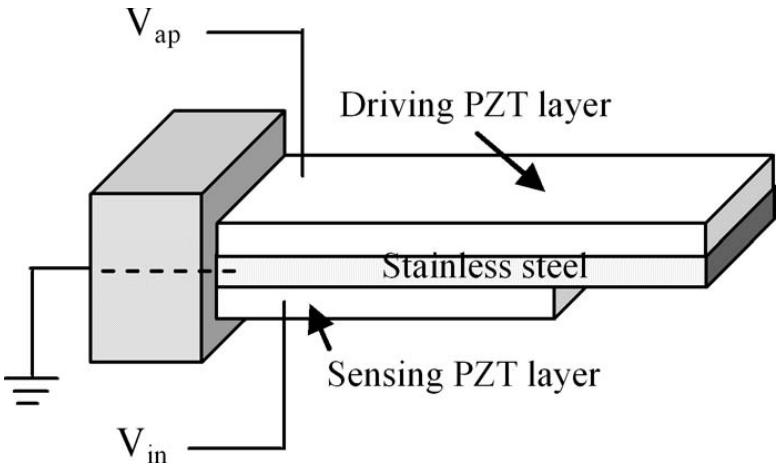

Figure 2.2: Schematic of a PZT/stainless steel piezoelectric cantilever with both a top driving PZT layer and a bottom sensing PZT layer (Szewczyk 2006).

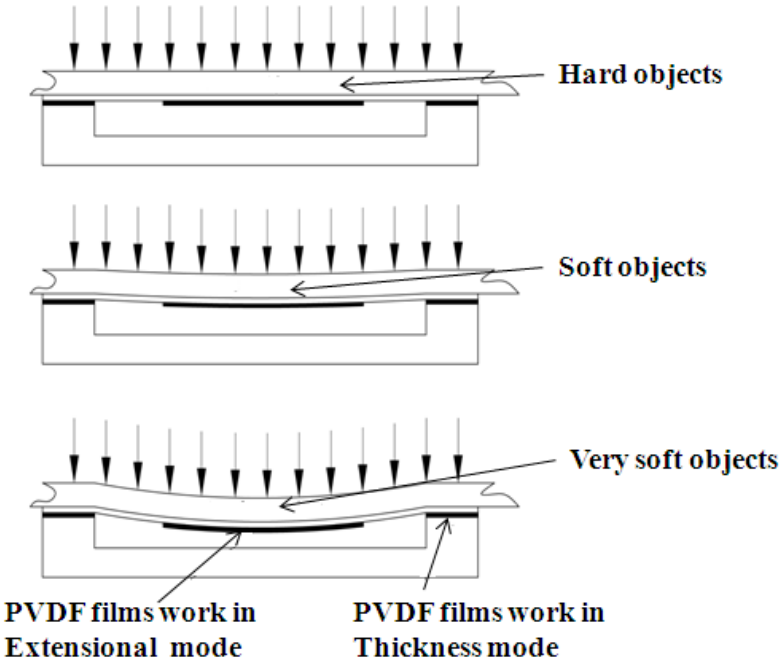

Figure 2.3: Schematic of a unit of a PVDF-based stiffness sensor (Sokhanvar, Packirisamy et al. 2007).

Figure 2.3 shows a proposed endoscopic grasper with stiffness sensor made of piezoelectric materials, polyvinyllidene fluoride (PVDF). The PVDF film jaw of the endoscopic grasper is equipped with a number of aluminium electrodes. When the force cause stress in the PVDF film, polarisation charges which produce voltage signals are generated. The magnitude, position and stiffness can then be determined by measuring

and comparing the amplitude of the output voltages at all electrodes (Sokhanvar, Packirisamy et al. 2007).

Although piezoelectric−based stiffness sensors have many advantages, piezoelectric materials are inherently subject to charge leakages which cause the deterioration of voltages in the presence of static forces. Hence they cannot provide true measurements of static forces. Another drawback is they are very sensitive to changes in temperature (P. Dario and D. De Rossi 1985).

Zheng and Mak developed a portable ultrasound indentation system using the ultrasound transducer itself as the indenter (Zheng Y P 1996). The system is capable of measuring both the initial thickness and stiffness. Due to its ease of operation and relatively small profile, this instrument has been successfully applied in a variety of clinical situations for the assessment of soft tissues (Zheng Y P 1996; Zheng YP 1999; Leung SF 2002; Huang YP 2005; Lau J 2005; Zheng YP 2006; Zheng YP 2000). However, the use of this system is still limited when it is applied to small specimens such as the skin and articular cartilage. Ultrasound elastography can generate images of tissue elasticity by propagating mechanical waves through the tissue (Laurent Sandrin 2002; Jean-Luc Gennisson 2004; Jinhua Shao 2009). While this method is effective for detecting tumours, it provides a 2D image of relative stiffness, rather than the quantitative measurements of tissue stiffness.

For active indentation-based stiffness probe, several actuating elements (e.g. a vibrator, motor) are included in the device. An air-driven oscillating stiffness probe was developed to detect bulk tissue compliance in stumps of amputated lower limbs (William M. Vannah 1999). The pressure was controlled by a flexible rubber hose and the displacement was recorded by an electromagnetic sensor. Kawahara T et al.

proposed an air-driven based phase differential technique for Video-Assisted Thoracic Surgery (T. Kawahara 2010). Another indentation tool (TeMPeST1-D) was developed by Ottensmeyer and Salisbury to monitor force-displacement response over a frequency range from DC to approximately 100 Hz (M.P. Ottensmeyer 2009). This probe makes use of a voice-coil linear actuator to drive a right cylindrical indenter.

Kaneko et al. proposed the camera-based stiffness probe that gives both visual and stiffness information of a human stomach, Figure 2.4 (M. Kaneko 2004). An air puff is applied to the stomach and the displacement is measured by a CCD camera. This idea has been further extended into the non-contact stiffness imager that can detect the

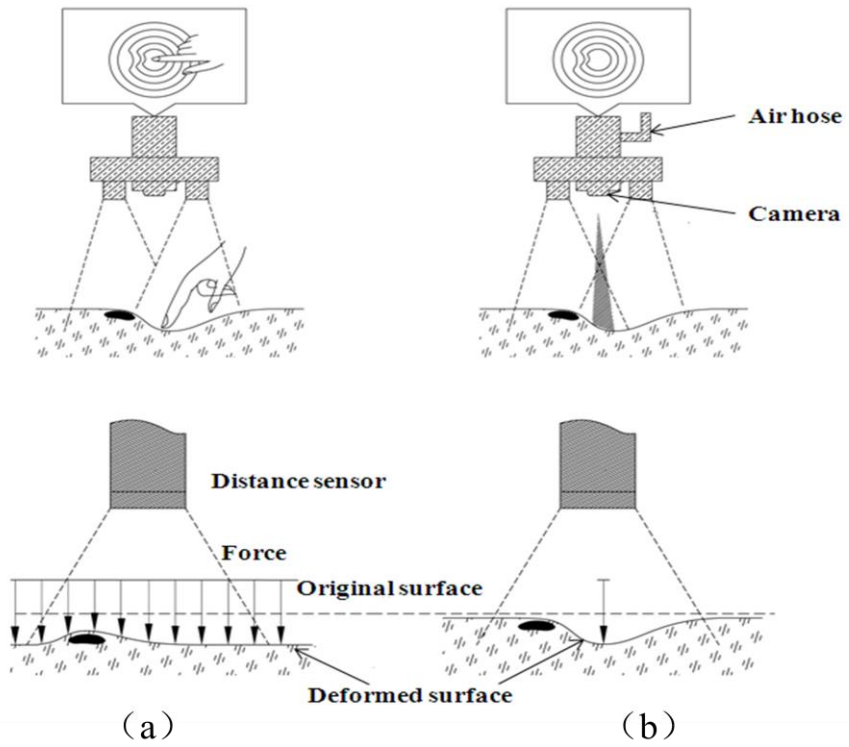

Figure 2.4: Conceptual image of Stiffness Imager. (a) shows an example of Stiffness Imager where a force is given directly to the environment by a contact probe and a CCD camera. Such a system is a contact probe, however, always meets occlusion at the point where the environment is hidden by the probe.(b) shows an example of non-contact Stiffness Imager, where the force is given to the environment by an air jet. The CCD camera observes the change of pattern during a force probing The change of pattern includes the stiffness information (M. Kaneko 2004).

stiffness distribution as a visual pattern (M. Kaneko 2004). However, since only a visual pattern does not provide surgeons with accurate stiffness values of target tissue.

A stiffness probe based on fibre optic techniques was proposed by H Liu, in collaboration with the author (Hongbin Liu 2010; H.Liu 2011). Figure 2.5 indicates the structure of the probe. The probe consists of an optical fibre force sensor (FS), and four optical fibre displacement sensors (DS), DS-1, DS-2, DS-3 and DS-4. A spherical roller with a diameter of 6 mm is connected to the force sensor and can rotate freely. Sensing for both force and displacement measurements are based on a light intensity modulation scheme (P. Puangmali 2008). When the probe indents into a soft tissue surface, the optic fibre FS measures the forces acting on the roller. When an axial force is applied, the four spheres (D_1, D_2, D_3 and D_4) which are free to slide axially are

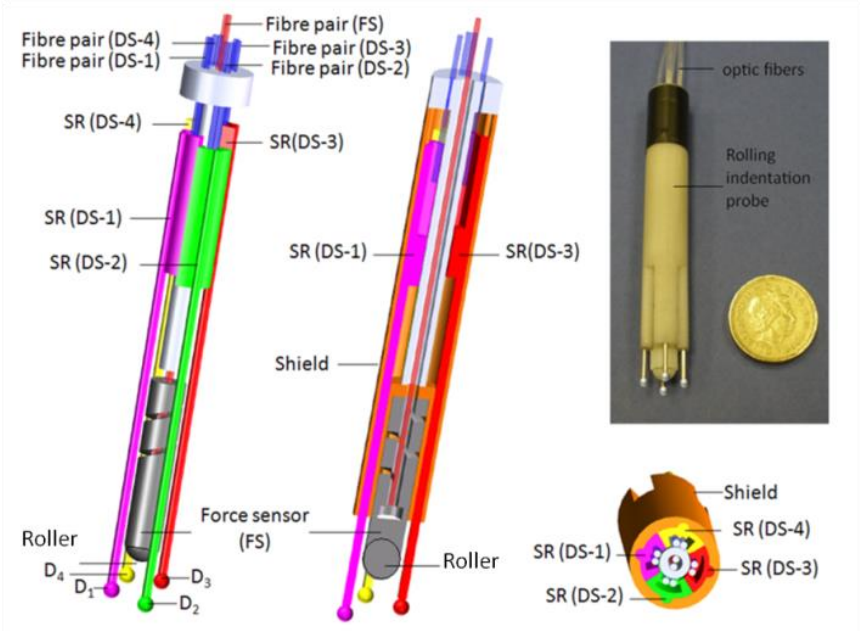

Figure 2.5: The stiffness probe consisting of one optical fibre force sensor (FS) as well as four optical fibre displacement sensors (DS), a one pound sterling coin is used to indicate the size of the stiffness probe (Hongbin Liu and Jichun Li et al. 2011)

pushed to slide upwards by the surrounding tissue, following an exponential curve (Johnson 1985). By modelling the relationship between the curve and the displacements of the four sliding rods, the indentation depth can be obtained. It should be noted that

the indentation depth is measured indirectly by detecting the deformation of the surrounding soft tissue, rather than measuring the relative displacement of the tip of indenter with regards to the tissue surface directly. Test results showed that the proposed probe is accurate and has good repeatability in measuring rolling indentation depth (Hongbin Liu 2010; H.Liu 2011).

For stiffness sensing of soft tissue, both the indentation deformation and reaction force need to be measured simultaneously. There are a variety of techniques which have been employed to intra-operatively measure the tissue deformation for biomedical applications.

The simplest method for measuring soft tissue deformation can be achieved by attempting to keep the indentation depth approximately constant. T.Lyyra et al. proposed a stiffness probe providing a constant deformation using a cylindrical indenter (Ø1 mm, 300mm length) positioned in the centre of an inclined reference plate of a rod (T. Lyyra 1999). Obviously, a constant deformation is not always achieved for different biomedical applications. To overcome this problem, a number of displacement sensors including LVDT sensor, laser sensor, optic encoder and electromagnetic sensor are employed to measure the relative displacement of the tip of stiffness probe with respect tothe tissue surface (William M. Vannah 1999; M.P. Ottensmeyer 2009; T. Kawahara 2010). While these displacement sensors have a high resolution, a registration at the inspection point is required, since the surface of the organ normally is uneven.

Intra-operative three-dimensional computed tomography (CT) technique can differentiate the bones from other tissues effectively and is widely used in oral surgery (Pohlenz, Blessmann et al. 2008), orthopedic surgery (Love, Pillai et al. 2008), and the prostate brachytherapy (Jain, Deguet et al. 2007). However, due to the cost and the

radiation exposure, it is not suitable for intra-operatively measurement of the tissue deformation.

The stereo vision is a more practical and inexpensive technique using two or more cameras to extract the 3D structure of the operating field and track the temporal motion of deformable tissue surfaces (Mourgues, Devernay et al. 2001; M. Kaneko 2005; Stoyanov 2005). While this approach is promising and progressing, one major downside with this technique is the difficulty of extracting features on curved and specular surfaces and it is not always working effectively (Keller and Ackerman 2000).

A laser line scanner can be employed to extract features on curved surfaces with high resolution 3D images. However, it is difficult to apply this technique to acquire feature information in real-time (N. Tanaka 2008).

The structured light technique can obtain the 3D deformation of a curved object in real time. This technique utilizes a projector to project a known light pattern onto the objects. The pattern reflected by the objects can be viewed by a camera mounted next to the projector. Knowing the position of the camera and the projector, the 3D information of each object can be obtained (Hu, et al., 1989)(Keller, et al., 2000)(Lavoie, et al.) .

2.4 Modelling and Finite Element Techniques for Soft Tissue

An accurate model of the mechanical behaviours of biological soft tissue is required for many medical applications. Soft tissue models can be utilized to intra-operatively detect stiffness of solid organs and thus determine tumours in MIS (Hannaford, Trujillo et al. 1998). Soft tissue models are beneficial to improve the performance of surgical training simulators (V.Vuskovic 2000). In addition, soft tissue models can aid the surgeon to control the tool-soft tissue interactions (Glozman and Shoham 2007). Based on soft tissue models, mechanical tissue properties can be

represented using model parameters identified by means of measurements from tool-soft tissue interactions.

Many soft tissues with organs, especially those porous internal structures, are anisotropic, heterogeneous and nearly incompressible. Most biological tissues show highly nonlinear characteristics, viscoelasicity and variable mechanics depending on the environmental parameters such as pH, temperature and health. The biomechanics of soft tissue is time and strain rate dependent (Fung 1993; Humphrey 2002; Rubin and Bodner 2002). Researchers have developed a variety of models to mathematically describe the mechanical behavior of soft tissues. These models can be summarized as hyperelastic (nolinear elasticity) models, linear viscoelastic models and nonlinear viscoelastic models (Fung 1993; Prange and Margulies 2002; Gasser 2006; El Sayed, Mota et al. 2008).

2.4.1 Nonlinear Elasticity Modelling of Soft Tissue

Soft tissue exhibits a highly nonlinear stress-strain relation when subjected to a finite deformation. Polynomials or exponential functions are widely used to describe the stress-strain relation (Morgan 1960; Ridge 1964; Brouwer and Ustin 2001; Carter, Frank et al. 2001; Okamura and Simone 2002; Han, Alison et al. 2003; Ahmadian and Nikooyan 2005). For example, Okamura et al. (Okamura and Simone 2002) reported a second order polynomial function to fit experimental data for bovine liver, Equation (2.1)

$$F(Z) = K_1 Z + K_2 Z^2, \tag{2.1}$$

where F is the indentation force, Z is the tool displacement, and K_1,K_2 are stiffness coefficients.

Ahmadian et al. (Ahmadian, et al., 2005) developed two empirical exponential equations to predict uniaxial nonlinear force-displacement characteristics of liver and kidney, Equations (2.2), (2.3) :

For liver,

$$F(Z) = \sum_{i=1}^{2} g_i \mathrm{e}^{-\left[\frac{m_i - z}{n_i}\right]^2}. \tag{2.2}$$

For kidney,

$$F(Z) = \sum_{i=1}^{2} \mathrm{v}_i \mathrm{e}^{-w_i z}, \tag{2.3}$$

where

F is the indentation force, Z is the tool displacement, and g_i, m_i, n_i, v_i, w_i are constants determined experimentally.

Han et al. (Han, Alison et al. 2003) extended earlier equation by Fung (Fung 1993) and presented an exponential equation to fit the experimental data, describing deformations of human heart, have been used to fit the tension data, Equation (2.4)**(2.4)**:

$$F(Z) = \alpha\left(e^{\beta z} - 1\right), \tag{2.4}$$

where

F is the indentation force, Z is the tool displacement,and α, β are constants determined by experimental data.

With an attempt to more faithfully describe nonlinear soft tissue behaviors, strain-energy functions are utilized to model the complex multi-dimensional nonlinear elasticity of soft tissue. The stress-strain function of such material can be derived from

the partial differentiation of the strain energy function with respect to strain. The first hyperelastic models, the Neo-Hookean and Mooney–Rivlin models, were initially developed by Ronald Rivlin and Melvin Mooney(Mooney 1940; Rivlin 1947). The Ogden model and the Arruda–Boyce model are another two widely used models (Prange and Margulies 2002; Kerdok, Ottensmeyer et al. 2005).

The Neo-Hookean strain energy function (U) is given by Equation (2.5) (ABAQUS 2008) :

$$U = C\left(I_1 - 3\right) + \frac{1}{D}\left(J^{el} - 1\right)^2 \tag{2.5}$$

where C is the Neo-Hookean constant,D is a temperature-dependent material parameter,J_{el} is the elastic volume ratio. Under uniaxial deformations the soft tissue is a fully incompressible material, $J_{el} = 1$, and

I_1 is the first deviatoric strain invariants, Equation (2.6):

$$I_1 = \lambda_1^{\,2} + \lambda_2^{\,2} + \lambda_3^{\,2} \tag{2.6}$$

where λ_1, λ_2 and λ_3 are the stretch ratios, which are the ratios between current length and the original length in the principal directions of a material fibre.

The principal stretches, λ_i, are related to the principal nominal strain, ε, by Equation (2.7) :

$$\lambda_1 = 1 + \varepsilon\ ,\ \ \lambda_2 = \lambda_3 = \frac{1}{\sqrt{\lambda_1}}\ . \tag{2.7}$$

Equation (2.8) shows the Mooney-Rivlin strain energy function(ABAQUS 2008):

$$U = C_{10}\left(I_1 - 3\right) + C_{01}\left(I_2 - 3\right) + \frac{1}{D}\left(J^{el} - 1\right)^2\ , \tag{2.8}$$

Where C_{10}, C_{01} are the Mooney-Rivlin constants.,I_1 is the first deviatoric strain invariants.

I_2 is the second deviatoric strain invariants and given by Equation (2.9)**(2.9)**:

$$I_2 = \lambda_1^{-2} + \lambda_2^{-2} + \lambda_3^{-2} \tag{2.9}$$

Equation (2.10) shows the Ogden strain energy function(ABAQUS 2008):

$$U = \sum_{i=1}^{N} \frac{2\beta_i}{\alpha_i^2}\left(\lambda_1^{\alpha_i} + \lambda_2^{\alpha_i} + \lambda_3^{\alpha_i} - 3\right) + \sum_{i=1}^{N} \frac{1}{D}\left(J^{el} - 1\right)^2 \quad , \tag{2.10}$$

where

β_i and α_i are the Ogden constants. λ_1, λ_2 and λ_3 are the stretch ratios.

Equation (2.11) shows the Arruda-Boyce strain energy function(ABAQUS 2008):

$$U = \mu \sum_{i+1}^{5} \frac{C_i}{\lambda_m^{2i-2}}\left(I_1^i - 3^i\right) + \frac{1}{D}\left(\frac{J_{el}^2 - 1}{2} - \ln J_{el}\right) \tag{2.11}$$

where

μ is the shear modulus, λ_m is locking stretch, and C_i is the Arruda-Boyce constant defined by (ABAQUS 2008), as follows:

$$C_1 = \frac{1}{2}, C_2 = \frac{1}{20}, C_3 = \frac{11}{1050}, C_4 = \frac{19}{7000}, C_5 = \frac{519}{673750}.$$

Strain energy models have been widely used in modeling soft tissue for biomedical applications. A Neo-Hooken model and a Veronda-Westman model was utilized to model the kidney tissue (Vuskovic, Kauer et al. 2000). Prange et al. employed a modified Ogden hyperelastic model for modeling of the brain tissue (Prange and Margulies 2002). The breast tissue was modeled by using an Arruda-Boyce constitutive (Kerdok, Jordan et al. 2005).

Figure 2.6 shows the uniaxial stress-strain curve for the Arruda-Boyce model compared with other hyperelastic material models.

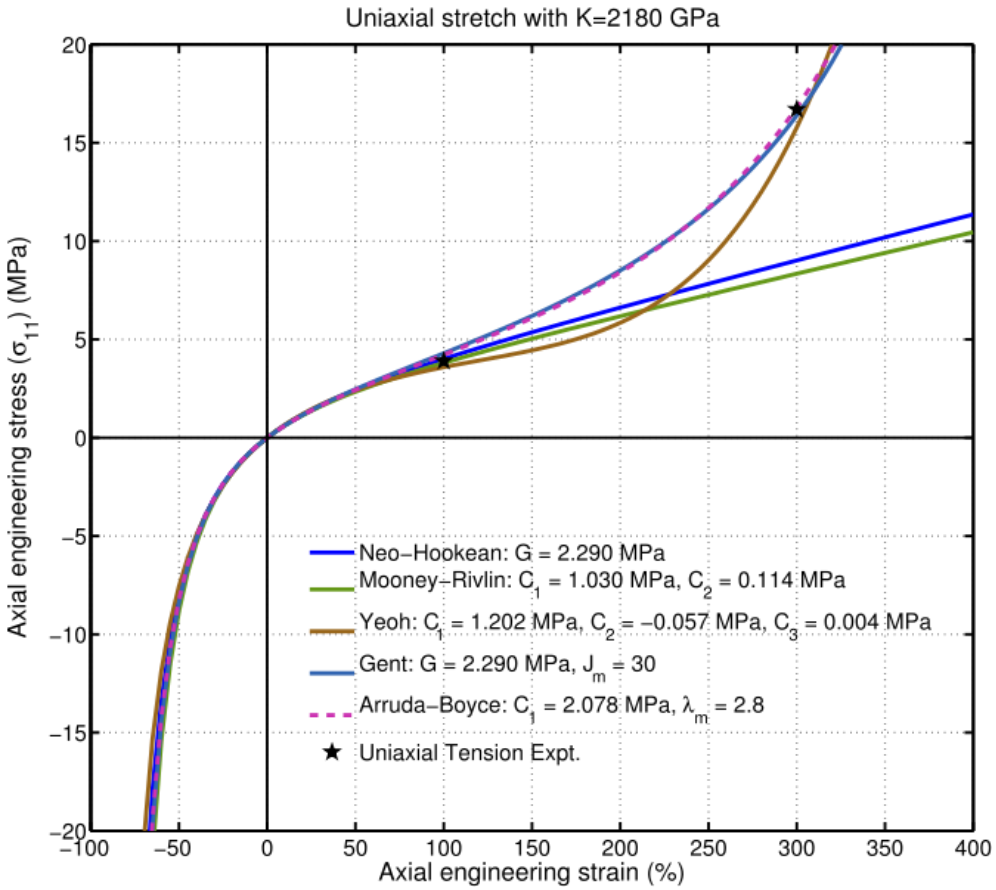

Figure 2.6: The Uniaxial stress-strain curve for the Arruda-Boyce model compared with other hyperelastic material models (http://en.wikipedia.org/wiki/File:ArrudaHyperElastic.svg)

2.4.2 Linear Viscoelastic Model

The theory of linear viscoelasticity can be employed to model an infinitesimally small deformation of soft tissue. The general differential equation using the principle of superposition for linear viscoelasticity is given by Equation (2.12) (Barnes, Hutton et al. 1989):

$$\left(1 + \alpha_1 \frac{\partial}{\partial t} + \alpha_2 \frac{\partial^2}{\partial^2 t} + \alpha_n \frac{\partial^n}{\partial^n t}\right)\sigma = \left(\beta_0 + \beta_1 \frac{\partial}{\partial t} + \beta_2 \frac{\partial^2}{\partial^2 t} + \beta_m \frac{\partial^m}{\partial^m t}\right)\varepsilon \qquad (2.12)$$

where n=m or m-1, ε is strain, σ is stress, α_i, β_i are constant parameters.

The linear viscoelasticity of soft tissue can also be viewed as a mechanical spring-dashpot models, where Hookean elasticity is represented by a spring and Newtonian viscosity by a dashpot. The basic models are the Voigt (spring and dashpot in parallel), Maxwell (spring and dashpot in series), and Kelvin (spring in parallel with a Maxwell) models (Barnes, Hutton et al. 1989; Fung 1993; Fung 1994; Humphrey 2002), Figure 2.7.

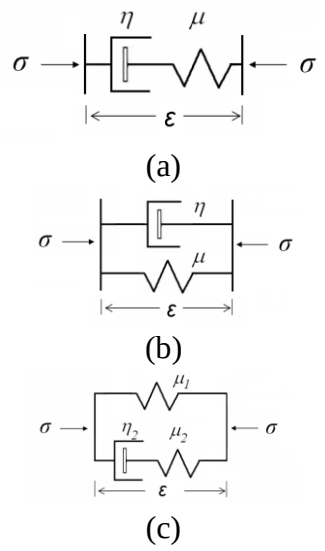

Figure 2.7: The three basic forms of a mechanical spring-dashpot model including Voigt model (a), Maxwell model (b), and Kelvin model (c). ε is strain, σ is stress, μ_i is the elastic coefficient of the spring and η_i is the viscosity coefficient of the dashpot, i=1, 2(Fung 1993).

Liu and Bilston (Liu and Bilston 2000) presented a 5-element Maxwell model forr *ex-vivo* bovine liver. Farshad et al. employed a linear viscoelastic lumped parameter model for pig kidney (Farshad, Barbezat et al. 1999). Kerdok et al. used two parallel Voigt models for *ex-vivo* porcine liver (Kerdok 2006). Kim et al. used the Kelvin model for *in-vivo* porcine liver (Kim, Tay et al. 2003). These studies showed that linear viscoelastic model is reasonable for soft tissue modeling when there is an infinitesimally small deformation.

2.4.3 Nonlinear Viscoelastic Model

While linear viscoelastic models are suitable for soft tissue with small deformation, nonlinear viscoelastic model soft tissue subjected to a large tissue deformation (Fung 1993; Gasser 2006; El Sayed, Mota et al. 2008).

The quasi-linear viscoelasticity (QLV) model proposed in (Fung 1993) was widely used to model many soft tissues including neck tissues, porcine abdominal organ and lower limb soft tissue (Zheng YP 1999; Tamura, Omori et al. 2002; Huang, Zheng et al. 2005). Miller et al. also developed new nonlinear viscoelastic constitutive equations for the description of brain deformation (Miller and Chinzei 1997; Miller 2000; Miller and Chinzei 2002). Rubin et al. developed a nonlinear viscoelastic model to predict the three dimensional strain energy dissipation of soft tissue. The proposed model was a combination of nonlinear elastic components and energy dissipative components, undergoing the same compressing and stretching (Rubin and Bodner 2002). Schwartz et al. proposed a nonlinear viscoelastic finite element model (Schwartz, Denninger et al. 2005). The proposed model can be utilized to simulate a wide range of mechanical tissue behaviours in real-time and has been employed for the planning of cryogenic surgery of the liver.

2.4.4 Finite Element Techniques

Finite element analysis (FEA) is a powerful computational technique providing approximate solutions to engineering problems with complex boundary conditions (M. J. Turner 1956).

Linear elasticity finite element models are one of the most widely used approach due to simplicity and high computation effectivity. M Bro-Nielsen et al. and S.Cotin et al. presented the first use of linear elastic finite element models for surgical simulation (M. Bro-Nielsen 1995; M. Bro-Nielsen 1996; S. Cotin 1996). M Bro-Nielsen et al.

developed a real-time volumetric finite element model with reduced complexity for human leg simulations (M. Bro-Nielsen 1996). The three-dimensional finite element model of human organs was produced using data from computed tomography (CT) scans (Cotin C 1999; E. Gladilin 2001).

While the linear elastic models are assumed to be valid for small displacements, nonlinear elastic or nonlinear hyperelastic finite element models are used to simulate large deformation of biological soft tissue. Tiller et al. presented three-dimensional hyperelastic finite element models to predict the behaviour of lamb kidney and the human uterus. The Neo-Hookean and Mooney-Rivlin hyperelestic models were utilized to validate the experiment results (Y. Tillier 2003). Tendick et al. employed the Mooney-Rivlin finite element model to simulate tissue deformation in a surgical training environment. The Mooney-Rivlin finite element model was evaluated using data from indentation experiments on porcine esophagus, liver and kidney (Jung Kim 2005) (Liu 2004). The Arruda-Boyce model was used to predict breast tissue behaviour (Kerdok 2005). K. Sangpradit et al. presented a finite element model (FEM) for simulating wheel-rolling tissue deformations using a rolling finite element model (RFEM). The proposed RFEM was validated on a silicone phantom and a porcine kidney sample (K. Sangpradit 2009; K. Sangpradit 2011).

Based on soft tissue model, living mechanical tissue properties can be represented using the model parameters identified by means of stiffness measurements during tool-soft tissue interactions. Recently, the inverse finite element method has been introduced to estimate unknown material parameters of biological soft tissue by minimizing the errors between finite element simulation and experimental results. An extended Kalman filter method is employed to minimize the disparity between magnetic resonance imaging (MRI) scan and finite element simulation results (M. Tada 2005).

The sequential quadratic programming (SQP) method was used for estimating breast tissue parameters by minimizing the error between experimental data and a finite element force-displacement model (A. Samani 2004; C. Choi 2006; J. E. Bischoff 2008). The Levenberg-Marquardt algorithm was used estimating parameters of porcine liver, kidney and lower esophagus (J. Kim 2005; C. Choi 2006). K. Sangpradit presented a method to identify the shear modulus of simulated soft tissue. The Arruda-Boyce constitutive equation and the Newton- Raphson method are used for parameter estimation of simulated soft tissue. The results showed that the method is accurate and robust.

2.5 Conclusions

Indentation is currently one of the most frequently used techniques to measure the variation in stiffness of soft tissues. A traditional indentation system utilizes an indenter to compress the soft tissue and resultant reaction forces and deformations are measured. There are two different approaches probes that are in direct contact with tissure and that are not. The direct contact approach means that a contact force is applied to a target directly by using a probe equipped with an appropriate force sensor.A non-contact approach imparts a force through a fluid jet, such as an a water or air jet. For the non-contact approach, it is hard to expect high accuracy and resolution because, in most cases, the sensor is implemented into the nozzle where the fluid jet is launched from, sensing intrinsically inaccurate. In addition, when using the water jet indentation for in-vivo tissues diagnosis, water will collect inside the body and need to be removed by another means. The contact approach, generally, can achieve higher accuracy and resolution for stiffness measurements compared with the non-contact approach. Current stiffness measurement instruments based on indentation presents difficulties for further miniaturization. Another drawback of indentation based method is that they are time

consuming due to the operation mode: To measure the stiffness distribution of a whole organ, the organ surface needs to be scanned point by point. Since the surface of the organ normally is uneven, a registration is required at each step. As a result, the indentation approach generally has a low scanning speed.

For vibration-based stiffness measurements, most stiffness probes include an actuating element to provide a controlled deformation or force, which limits the miniaturisation of such probes and also increases the fabrication complexity. This approach becomes even more challenging in applications within a confined space, such as in MIS.

The rolling indentation approach for the tissue diagnosis during MIS is effective and robust (Hongbin Liu 2010; H.Liu 2011) . However, the current implementation of wheeled indenters are fragile, easily damaged and suffer from increased fabrication complexity. Furthermore, due to the mechanism of sliding rods, the reliability of the probe is reduced and it is difficult to clean the probe because of the moving parts used.

In view of the limitations of the current measurement modalities for measuring soft tissue stiffness, a stiffness probe with important characters such as structural simplicity, high scanning speed, low cost and multi-functionality is proposed and investigated in this research.

While linear models are suitable for soft tissue modelling with small deformation, nonlinear models are subjected to large tissue deformations. Both linear models and nonlinear models for tool-soft tissue interaction are studied in this thesis.

Chapter 3

A Stiffness Probe Based on Force and Vision Sensing Modalities

Chapter 3

3.1 Introduction

Minimally invasive surgery (MIS) is becoming the more preferred approach for surgeons and patients because of distinct advantages including reduced blood loss, tissue trauma, discomfort, recovery time and hospitalisation costs (Fuchs 2002). Recently, advanced surgical robots such as the ZEUS® Surgical System (S. Uranüs 2002) and the da Vinci® Surgical System (Guthart and Salisbury 2000) have been introduced to perform more complex surgical operations in minimally invasive surgery. While minimally invasive surgery enables the surgeons to achieve much better outcomes than traditional surgery, the lack of 'sense of touch' is still one of the major downsides which could lead to a reduced surgical outcome (Deml, Ortmaier et al. 2005).

In order to achieve more effective surgical outcome, the surgeon should be able to feel tissue stiffness. The stiffness information of biological soft tissue is very important for a variety of biomedical applications. Stiffness helps the medical doctors to evaluate the health of tissue and identify tumours buried under the tissue surface at an early stage in organs such as breast, liver, kidney and prostate (Garra BS 1997; McKnight AL 2002; Brown, Rosen et al. 2003; Phipps, Yang et al. 2005; H.Liu 2011). The tissue stiffness can also be utilized to improve the performance of training simulators for clinical examinations. Finally, stiffness sensing has potential in numerous new application areas including rehabilitation robots, service robots and surgery robots. Stiffness of soft tissue can be obtained by clinicians using manual palpation. Palpation is one of the widely used approaches for clinicians to differentiate benign and malignant tissues in many biomedical applications. However, the lack of quantitive data of mechanical properties of soft tissue is a significant drawback of palpation. Moreover, during MIS it is impossible for the surgeon to directly palpate the tissue for tumour

location due to the small size of the incisions. Consequently, the development of a stiffness sensitive device is becoming more and more attractive for researchers all over the world.

There are two main ways to measure the deformation of soft tissues during indentation: (a) directly measuring the relative displacement of the tip of an indenter indenting the tissue surface and (b) measuring the change of some parameters of soft tissue, such as the volume, deformation curve or the contact area to get the relative displacement of soft tissue indirectly. While most research currently focuses on the measurement of relative displacement directly, the latter method of measuring the indentation depth indirectly will be explored in this thesis.

In view of limitations of the current measurement modalities for measuring soft tissue stiffness and soft tissue deformation in Chapter 2, a novel tissue diagnosis probe is presented based on several of the aforementioned technologies in this chapter. The proposed probe is based on stiffness measurements using force and vision modalities, comprising a commercially available force/torque sensor, a digital microscope to allow simultaneous measurement of the indentation depth and the tissue reaction force during sliding indentation. The proposed probe is composed of a force/torque sensor and a digital microscope to measure the contact area of probe-soft tissue interaction. The contact area measured by the digital microscope can be used to estimated the indentation depth. Knowing the indentation force and depth, the stiffness of the target tissue is obtained. Since current imaging techniques convey visual information, the indentation depth information related to the visual information during tool-tissue interaction is explored. Thus, we explore the capability of obtaining stiffness distribution with an endoscopic camera, using a single probe. Applying this technique,

the surgeons can obtain quantitative information on the properties of the investigated soft tissue and improve diagnostic decisions.

The advantages of utilizing such a probe are listed as follows: 1) Due to its simple sensing structure involving no moving parts, it is easy to manufacture, and the probe can be miniaturized for many biomedical applications; 2) The proposed probe can measure indentation force and indentation depth concurrently. Compared with other contact probes using cameras to capture the contact area, which always has occlusion at the measurement point which is covered by the probe, the probe proposed here can avoid such an occlusion by using a transparent round head and actually imaging the area of interest. 3) The proposed probe can conduct continuous measurement on an uneven surface of soft tissue using sliding indentation due to the round shape of the probe head: The probe can cover a large area of soft tissue rapidly similar to rolling indentation; 4) The probe can also be used by the surgeon to observe the tissue visually since it has an image acquisition unit and the head of the probe is clear, doubling the probe's purpose incorporating an endoscopic function.

This chapter is organized as follows. Section 3.2 presents the working principle of the probe. Section 3.3 gives the design and calibration of the prototype. Section 3.4 validates the effectivity and sensitivity of the prototype by tests on simulated soft tissue made from silicone gel and excised porcine kidney samples. Section 3.5 provides conclusions.

3.2 Working Principle

3.2.1 Principle of stiffness sensing

Figure 3.1 shows a conceptual image of the proposed probe indenting a target soft tissue. The proposed probe is composed of a force sensor, a transparent sphere

mounted at the tip of a shaft and an image acquisition unit (digital microscope) for displaying and recording the contact area. Generally, when the probe indents the soft tissue, the contact area between the probe and tissue will be circular. When increasing indentation depth, the diameter of the circular area will also increase. The digital microscope images the contact area between the sphere and soft tissue. Then the contact area acquired from the camera images can be converted into indentation depth estimates. By combining the indentation force and the indentation depth, the stiffness of the target tissue can be estimated. To the best of our knowledge,

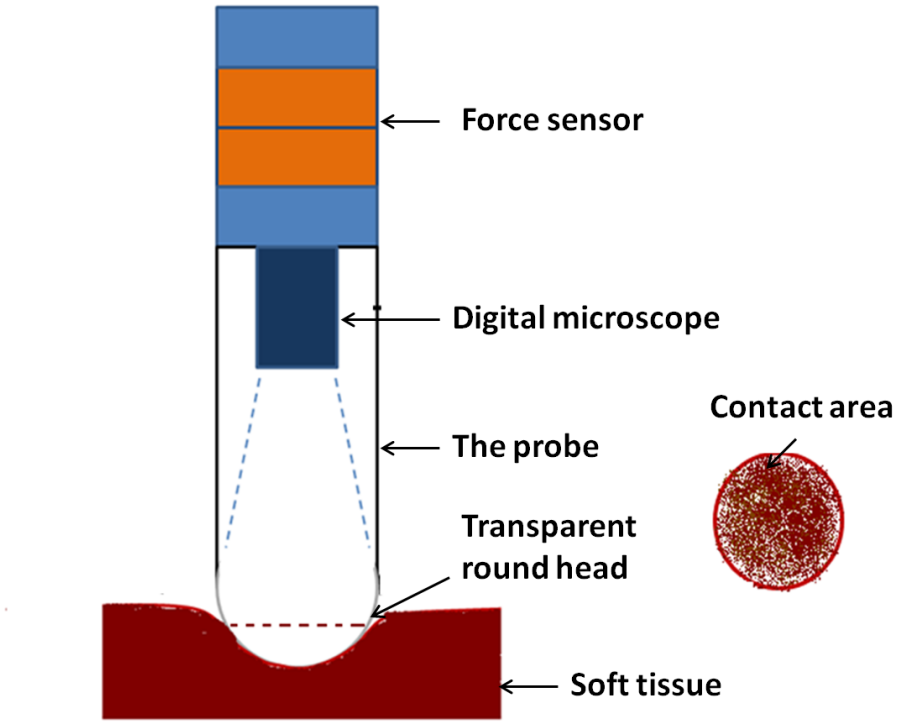

(a) (b)

Figure 3.1: (a) a conceptual image of the proposed stiffness probe indenting target soft tissue: the proposed prototype consists of a force sensor, a digital microscope and a shaft with a transparent round head made from glass. (b) A circular contact area seen from the digital microscope

there has not been any work under fallen previously that estimates the indentation depth by measuring the contact area.

3.2.2 Modelling the relation of indentation depth and contact area using finite element analysis

In recent years, finite element analysis (FEA) is widely used for predicting tissue behaviour and identifying tissue properties for many biological applications including surgery simulation, tool-soft tissue interactions, surgery planning and surgery training during robot-assisted surgery (K. Sangpradit, 2010;K. Sangpradit, 2009; K. Sangpradit,2011;V.Vuskovic, 2000 ;Prange, 2002 ;Kerdok, 2006;Kerdok, 2005).In order to investigate a preliminary relation between indentation depth h_{si} and contact area A_s (the diameter of a circular area is given as D_{sc}), FEA is employed to model tissue behaviour under indentation tests using a spherical indenter (diameter of 10mm).

In this study, the hyperelastic Arruda-Boyce equation is used to model tissue behaviour since it is widely used for modelling relatively large tissue deformations (Fung, 1993; ABAQUS,2008; Boyce, 1998).

In this study, two different materials: a silicone phantom (RTV6166, General Electric) which has mechanical properties similar to biological soft tissue (Okamura, 2004); porcine kidney samples were used here to simulate normal tissue. Parameters of the test materials are shown in Table 3.1.

The dimensions of the used silicone phantom were 15mm (height) × 45mm (length) × 45mm (width). The FE model of the silicone phantom was assumed to be continues, isotropic, homogeneous, incompressible and hyper-elastic. Since the indenter is much stiffer than the silicone phantom, it is assumed a rigid body.

Table 3.1: Properties of the Test Materials (K. Sangpradit, 2011)

Materials	μ ,shear Modulus (kPa)	$\lambda_{m,}$ Locking stretch	Mass Density (kg/m^3)	% RMS Error
Silicone (RTV6166 gel)	4.98	1.05	980	0.12
Porcine kidney	1.85	1.05	850	0.32

The bottom of the silicone phantom was constrained to the X-Y plane. The contact between the indenter and the phantom is assumed to frictionless. The silicone block is meshed using 9000 eight-node linear brick elements with, reduced integration and hourglass control (C3D8R). The 3D finite element model is developed using the ABAQUS finite element software package, Figure 3.2.

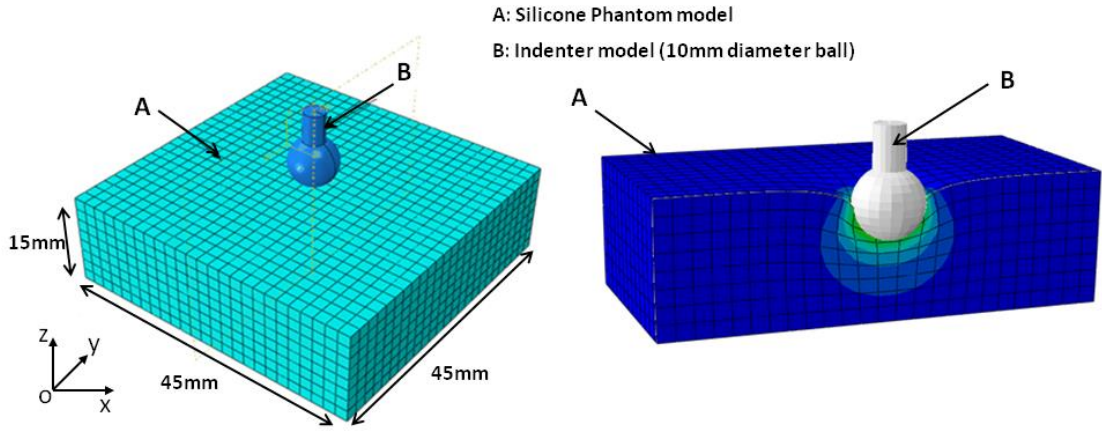

Figure 3.2: The 3D finite element model of silicone phantom and a cross section this model (by K. Sangpradit, 2011).

The FE model of the porcine kidney makes use of a similar assumption as done for the silicone phantom. The indenter was also assumed a rigid body and was positioned at a pre-defined area. The 3D porcine kidney mesh consists of 64570 ten-node modified quadratic tetrahedron (C3D10M) elements. Figure 3.3 shows the 3D finite element model of the kidney.

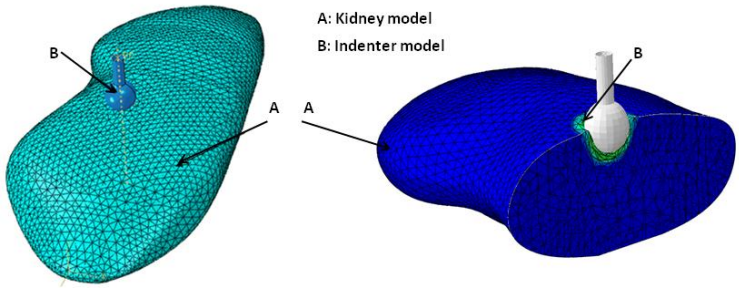

Figure 3.3: The 3D finite element model of silicone phantom and a cross section this model (by K. Sangpradit, 2011).

In order to evaluate the relation between indentation depth hs_i and the diameter of the contact area, $D_{sc,}$ virtual indentation tests on silicone phantoms and porcine kidney were conducted using the developed FE models. The protocol for these tests is listed below:

1. The indentation depth increases from 0 mm to 5mm with an increment of 0.2mm each step.
2. With the incrementation of indentation depth, the diameter of the contact area between the tissue and indenter were measured and recorded. For each indentation depth, the test was repeated 5 times.
3. According to the simulation results, the relation of hs_i and D_{sc} can be estimated using curve fitting for silicone phantom and porcine kidney respectively.

By curve-fitting the experimental measurements of hs_i as a function of D_{sc}, Figure 3.4, it was found that an exceptional function can accurately fit the data of both silicone phantom and porcine kidney, given by Equation (3.9):

$$h_{si} = 0.41 * (e^{0.43D_{sc}} - 1) \tag{3.9}$$

The R-square of the fitting is 0.99 and 0.97 respectively. The simulation results imply that it is feasible to use exponential function to describe the relation of indentation depth and the diameter of contact area. Thus the indentation depth can be obtained by measuring the diameter of contact area. However, more accurate model for such relation needs to be created based on experiments since simulation conditions were given ideally in above mentioned FE simulation.

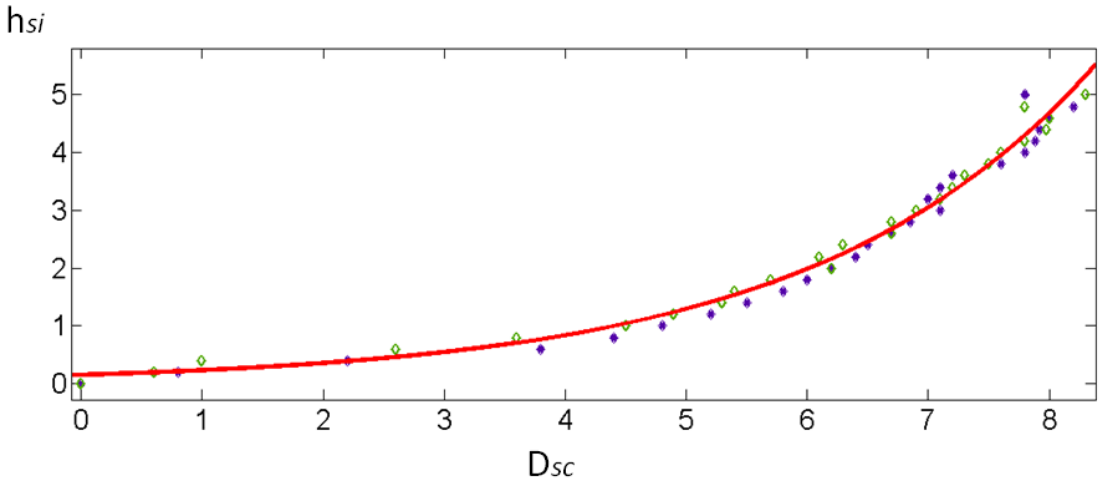

Figure 3.4: The relation of indentation depth hs_i and diameter of contact area D_{sc} based on FE simulation results. The purple dots are from the kidney model and the green dots are from silicone model. The red line is the fitting curve. All units are in "mm".

3.2.3 Working Principle for measuring indentation depth using CCD camera

In order to obtain the indentation depth during probe-soft tissue interactions, diameter of circular contact area between the probe and the soft tissue were used as size standards within the achieved images. By measuring their size in the recorded video images, the displacement of probe tip (indentation depth in axial direction to the probe) can be estimated.

Figure 3.5 shows the working principle for measuring indentation depth using CCD camera. In the non-deflected situation the contact area are in the zero-plane, since every pixel recorded by the CCD can be mapped with a specific coordinate in the zero-plane, it is possible to calculate the physical coordinates of the individual contact area. The mapping can be done by calibration of the contact area with known positions in the zero-plane and determining their position in the recorded image.

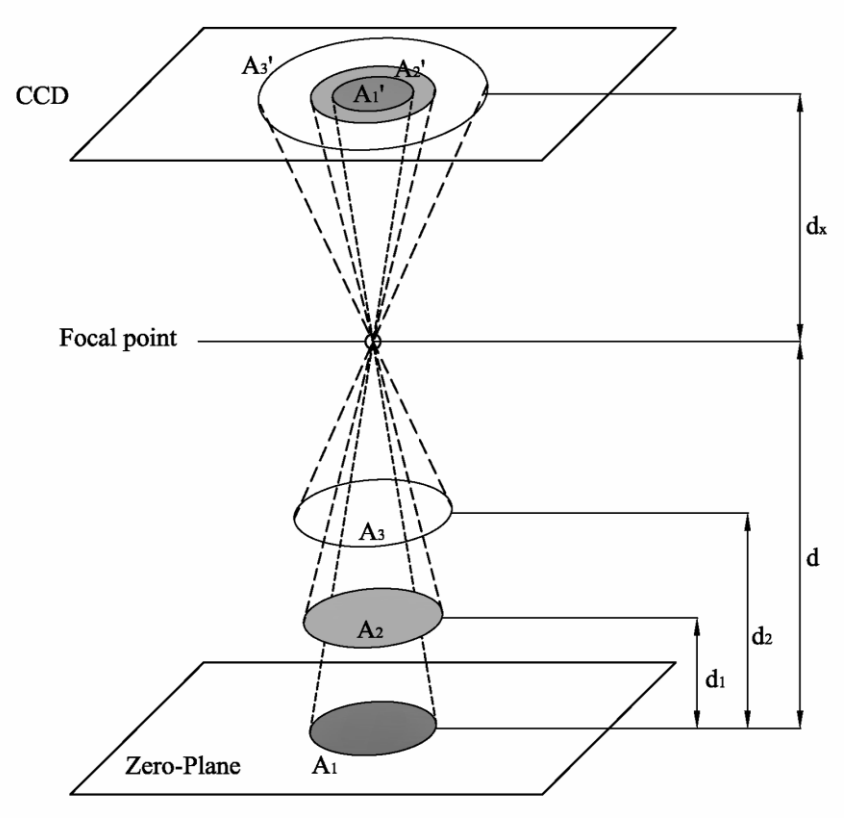

Figure 3.5: Representation of the optical paths in the endoscope. Three contact areas with increasing diameter are drawn (A1, A2 and A3). Different distances to the digital camera's focal point lead to differences in size on the recorded image (on the CCD-chip. dx is the distance between focal point and CCD-chip, d1 and d2 are the axial displacement of A2 and A3 from the zero plane. d is the distance between the zero-plane and the focal point. The indentation depth can be calculated trigonometrically with the measured diameter of image captured by the CCD.

3.3 Design and Implementation of the stiffness probe

Figure 3.6 shows the prototype probe that was designed and developed. The prototype probe consists of three main parts: a force sensor, a digital microscope and a transparent sphere with a diameter of 10mm made from borosilicate glass, at the tip of the probe shaft. This first probe is equipped with a commercial force/torque (F/T) sensor (Nano17, SI-25-0.25, ATI Industrial Automation). The image sensor of the digital microscope (a diameter of 8mm) is a 1.3MP CMOS with a maximum capture resolution of 1600×1200 pixels and 400× magnification.

Figure 3.6: A prototypes of a probe equipped with a commercially available force/torque sensor, (ATI Nano 17).

Figure 3.7 shows an overview of the data acquisition system for stiffness measurements. The system consists of a PC, a PCI Data Acquisition Card (NI PCI 6034E, which is a 16-bit DAQ card) and the probe. Data from the force/torque sensor is acquired using the National Instruments LabView 8.0 software package. Image data is

captured and processed by a commercially available image processing software program, HIG (developed by Holdtecs, Shuyou Ltd, Chengdu China).

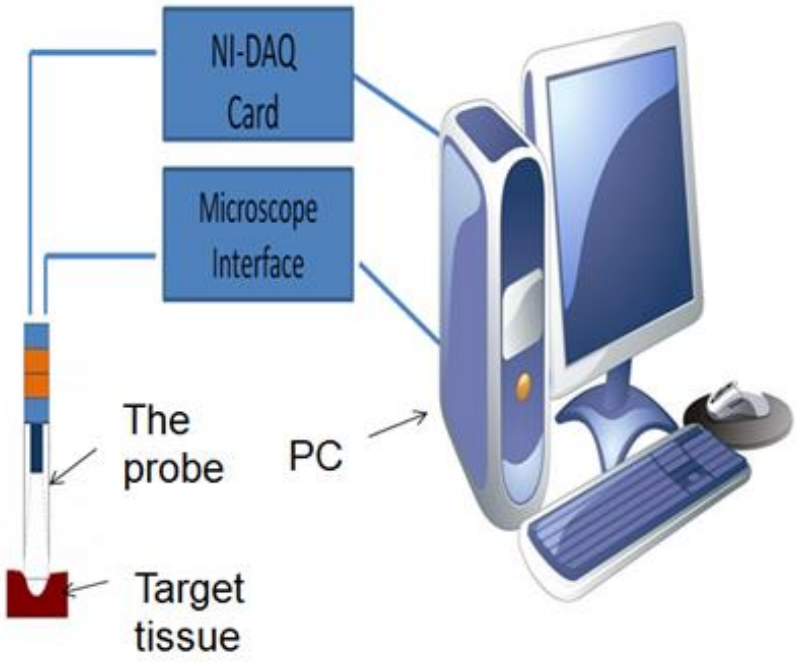

Figure3.7: Overview of the data acquisition system for stiffness measurement. The system consists of a PC, a NI PCI 6034E card and the probe.

3.4 Primary Validation Test

In order to validate the approach, experiments on silicone phantoms, pork liver, pork kidney and pork heart were conducted using the developed probe. The protocol utilized for these experiments is listed below:

1. One point of the sample was selected randomly and a single manual indention is carried out.
2. The digital microscope captures the probe-soft tissue contact area image using the HIG software.

3. The captured image is analyzed using the HIG software and the contact area is drawn using the “Extract Circle” menu.

As shown in Figure 3.8, the red circles are the measured contact areas during indentation experiments for randomly selected indentation depths during indentation of a silicone phantom, Figure 3.8 (a), pork liver, Figure 3.8 (b), pork kidney, Figure 3.8 (c) and pork heart, Figure 3.8 (d). The ex-vivo porcine samples used in these experiments were fresh organs obtained from a local store. These samples were obtained on the day of the experiments and transported to the lab within approximately 20 minutes after purchasing them. The lab conditions were as follows: lab temperature = 18.1^{o}C, lab humidity = 30%.

To obtain the indentation depth, the relationship between the indentation depth and the contact area need to be calibrated. The relation of the indentation depth, d_i, and the diameter of the contact area, d_{ca}, is investigated and validated in the following section. Calibration is carried for different tissue samples and can be used to estimate the indentation depth.

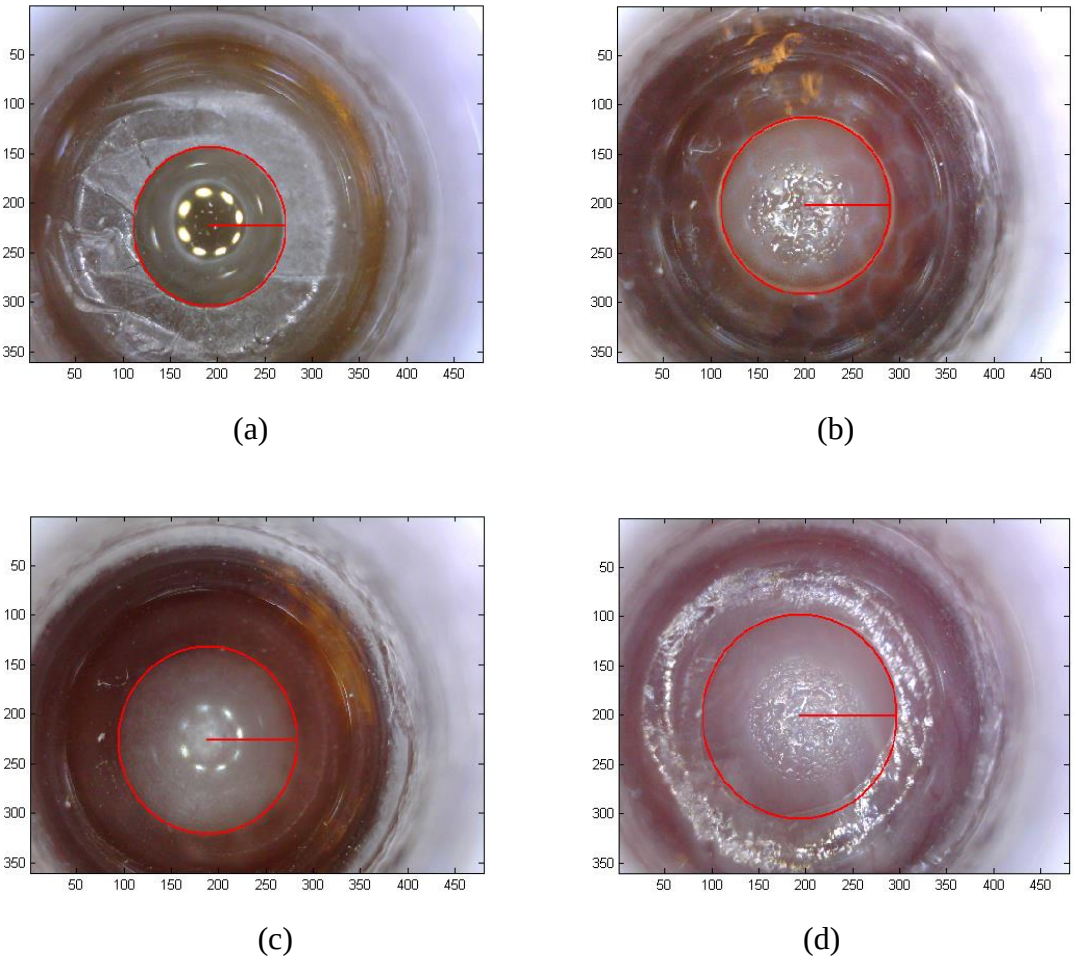

Figure3.8: The red circles show the measured contact area during indentation experiments using the developed probe. (a) Contact area on silicone phantom, (b) contact area on pork liver,(c) contact area on pork kidney, and (d) contact area on pork heart. All units are in "pixel".

3.5 Calibration of relation between indentation depth and diameter of contact area

The indentation depth (d_i) and the diameter of contact area (d_{ca}) are varied for different materials, to conduct calibration experiments. Four silicone phantoms (S-A, S-B, S-C and S-D) made from the RTV6166 gels with different stiffness values were used for calibration tests. The dimensions of these silicone samples are 100 mm * 100 mm * 30 mm.

Figure 3.9 shows the experimental setup for calibrating the relation between d_i and d_{ca}. The test rig consists of a robotic manipulator (RV-6SL, Mitsubishi), the developed probe and a silicone phantom. During the calibration test, the robotic manipulator holds the probe in a vertical orientation with respect to the silicone surface and indents into the silicone phantom at a speed of 5mm/s. After the indentation depth reaches 5mm, the robotic manipulator will stop indenting and move back to the original point. The image of the contact area and the indentation depth are recorded at a speed of 20 frames per second and the procedure is repeated four times for each sample.

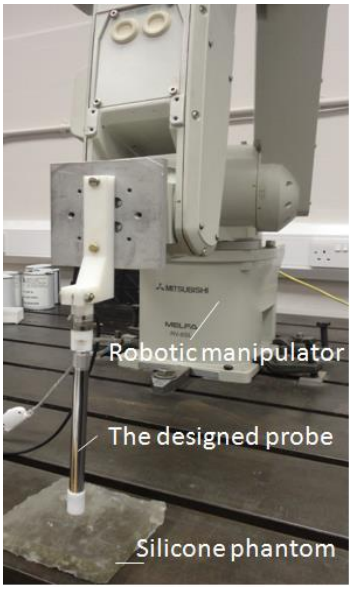

Figure 3.9: The experimental rig for calibration of indentation depth and diameter of contact area, using a robotic manipulator, Mitsubish RV-6SL.

According to experimental observations, the relation of d_i and d_{ca} follows an exponential function (Fung, 1993):

$$d_i = \alpha\left(e^{\beta d_{ca}} - 1\right), \qquad (3.9)$$

where α and β are constant coefficients obtained experimentally. For the calibration, β was found to be 0.46 for all the samples. Fig. 3.10 shows the calibration results for d_i and d_{ca} for the developed stiffness probe.

Table 3.2 shows the elastic modulus, coefficient α and R^2 using curve-fitting tool in Matlab, the fitted curve and the measured data for the four silicone samples S-A, S-B, S-C and S-D respectively. The results show that Equation 3.9 provides a good approximation for all the samples (R^2 >0.95).

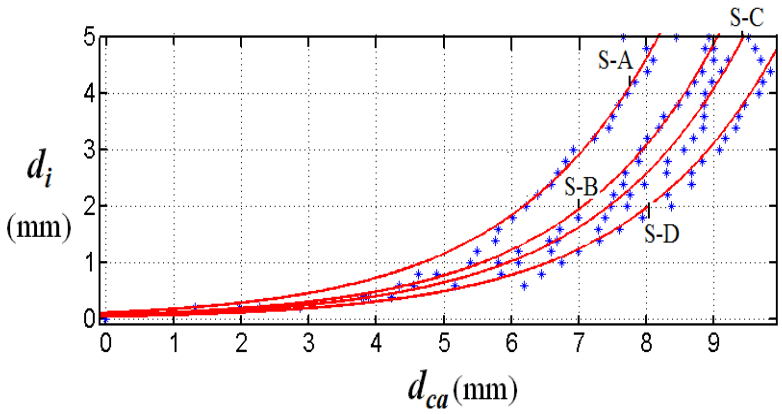

Figure 3.10： the relation of d_i and d_{ca} for four silicone phantoms with different stiffness; the blue pentagrams are the averaged measurements and the solid red lines are the fitted curves.

Table 3.1: Calibration results for four silicone phantoms

Items	Parameters and calibration results		
	Elastic modulus (Kpa)	*Coefficient α*	R^2
S-A	8.4	0.32	>0.95
S-B	18.2	0.21	>0.95
S-C	30.6	0.18	>0.95
S-D	51.2	0.14	>0.95

As shown in Figure 3.10, at a given indentation depth d_i, the measured d_{ca} increases with the increase of tissue stiffness. This indicates that if the probe is calibrated on a lower stiffness area, it will over-estimate the d_i for high stiffness regions. As shown in Table 3.2, using the calibration result of S-A (Phantom) (E = 8.4 KPa), the over-estimation of d_i increases with increasing of tissue stiffness. While the estimation error of tissue elasticity increases along with increased tissue stiffness, this implies that the probe is capable of differentiating soft tissue stiffness.

Table 3.2: The estimation errors in elastic modulus and indentation depth

Items	*Elastic modulus (Kpa)*	*Measured E (Kpa)*	*Error*
S-B	18.2	16.4	9.9%
S-C	30.6	24.2	20.9%
S-D	51.2	38.6	24.6%

3.6 Identifying Stiffness using Indentation Force and Depth

The probe is designed to non-invasively identify tumours from solid organs such as liver and kidney with small indentation depths. Thus the investigated tissue organ is assumed to have the following properties: 1) the tissue is linear elastic since biological tissues exhibit linear elasticity with small deformations; 2) the curvature of tissue surface is much larger than the diameter of the roller; 3) the normal tissue of the organ is isotropic, homogenous and incompressible.

According to the above assumptions, tissue stiffness can be modelled using the tissue elastic modulus, through the measurements of tissue reaction force and indentation depth. The elastic modulus of tissue is as follows (Margulies, 2004):

$$E = \frac{3f(1+v)}{8d_i\sqrt{rd_i}}, \qquad (3.10)$$

where E is the elastic modulus, f is the tissue reaction force normal to tissue surface, v is the Poissons ratio; for incompressible materials, v =0.5), d_i is the indentation depth and r is the radius of the indenter sphere head.

To validate the linear elastic assumption, indentation tests were conducted on silicone phantom and pork organs. During experiments, the probe indented into samples by 5 mm at a speed of 5mm/s driven by a robotic manipulator Mitsubishi RV-6SL. The image acquisition speed is 20 frames/second. Figure 3.11 shows the results of the experiments. It was found that Equation （3.10） fits the measurements well when the indentation depth is small (R^2 >0.96, h_i< 3.2 mm). The estimated results of kidney and liver show good agreement with existing literatures (B Hannaford, 1998;H Liu, 2008;H Liu, 2010).

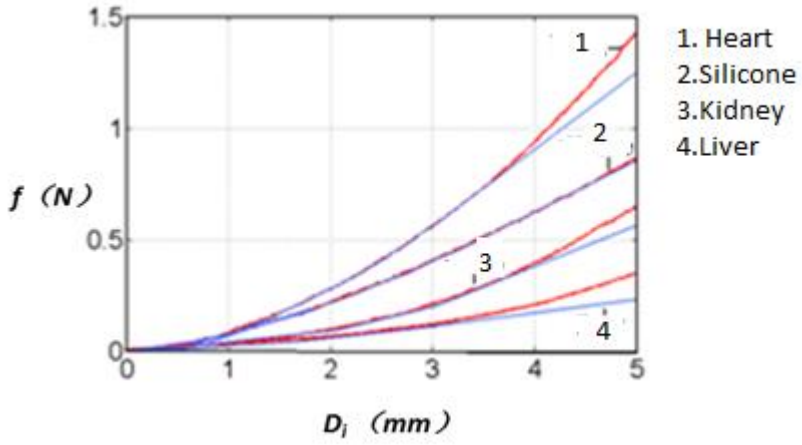

Figure 3.11: The relation of tissue reaction force f with the indentation depth d_i of the stiffness probe; the blue solid lines are the estimations using Equation（3.10）, the red solid lines are the experimental measurements.

3.7 Stiffness Image based on Sliding Indentation (SISI)

A new rolling indentation approach for tissue abnormality localization during MIS was proposed in (H.Liu,2008; H.Liu,2011).This approach employs a force-sensitive wheel to roll over a soft tissue organ, allowing the continuous and rapid measurement of the tissue stiffness as rolling takes place, thus obtaining the stiffness distribution of a large tissue area in a short time. By fusing the tissue reaction forces measured along each trajectory, the variations in tissue mechanical properties can be then mapped into a pseudo-colour rolling mechanical image (RMI). The RMI contains information on a tissue's geometrical stiffness distribution and the tissue reaction forces from the interactions between the wheel and the tissue. However, the effects of shear forces on the materials apparent stiffness, makes the stiffness measurements less accurate. Secondly, friction effects on the sensors during translation will become significant with increasing indentation depth. Hence, this research investigates a simpler approach, Stiffness Image based on Sliding Indentation (SISI), to acquire the stiffness distribution within soft tissue. While SISI is similar to RMI, for SISI, only the normal force, $F_{n,}$ is used to model the dynamic interactions between tool and soft tissue. Thus, the design of the roller integrated with a rolling indentation probe is simplified to a sphere head, which is capable of sliding over a soft tissue surface.

3.8 Tissue Abnormality Identification Using Stiffness Image based on Sliding Indentation

In order to analyse the capability of tissue abnormality identification using the proposed SISI, sliding indentation tests were conducted on a silicone phantom embedded with nine spherical simulated tumours made from rubbers. The dimensions

of the phantom and the position of simulated tumours are shown in Figure 3.12. The elastic modulus of the tumour was 219 KPa and that of the silicone phantom was measured as 14.7± 2.4 KPa.

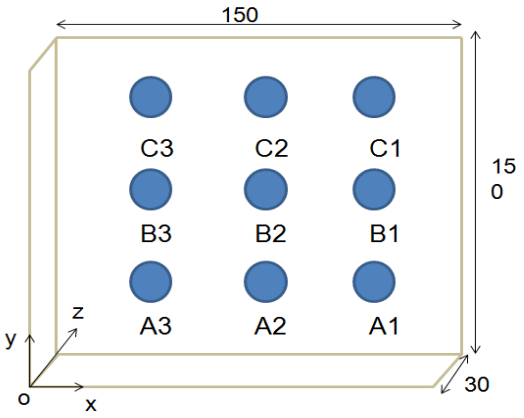

Nodules	Depth	Location (x, y)
A1	5	125, 25
A2	10	75, 25
A3	15	25, 25
B1	5	125, 75
B2	10	75, 75
B3	15	25, 75
C1	5	125, 125
C2	10	75, 125
C3	15	25,125

Figure 3.12: Schematic of the silicone phantom buried with nine simulated tumours and their locations and buried depths. All units are in "mm".

The silicone phantom has an uneven surface and the average surface height is 30mm $\pm$ 1.16 mm. In order to follow the linear elastic assumption of tissue, the maximum indentation depth was selected as 4 mm. The probe was driven by a robotic manipulator at a speed of 5 mm/s.

Prior to tests, the probe was programmed to follow multiple paths parallel to the *x-y* plane. The height of the plane was defined as 27mm causing an average indentation depth of 3 mm. To evaluate the robustness and repeatability of the probe, sliding indentation experiments were repeated five times.

After each test, the estimated tissue elastic modulus along the rolling path were fused together to generate a stiffness map. Figure 3.13 (a) shows the generated stiffness map and Figure 3.13 (b) indicates the location of the detected tumours.

Compared with the ground truths, the errors of the identified tumour locations range from 0.28 mm to 1.54 mm in *x* axis and from 0.32 mm to 1.98 mm in *y* axis. The standard deviations range from 1.64 mm to 2.52 mm along the *x* axis and from 1.12 mm to 1.96 mm along the *y* axis. This indicates good accuracy and repeatability of the localization of tumours based on the proposed SISI approach using the developed stiffness probe.

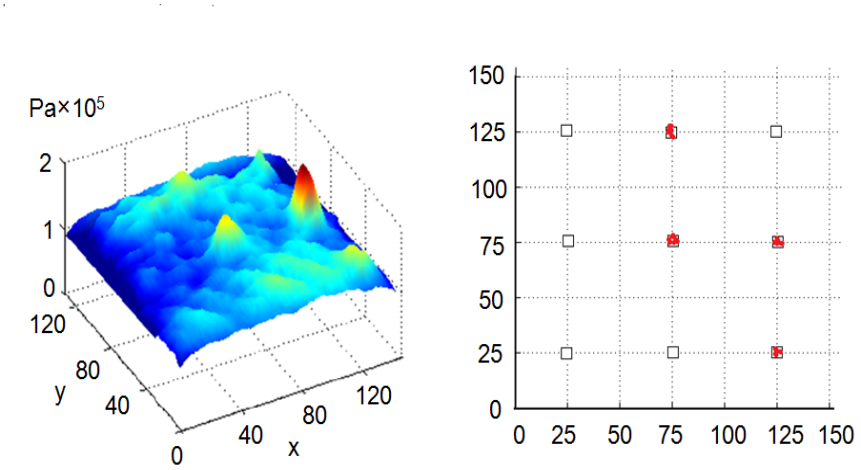

(a) (b)

Figure 3.13: (a) the stiffness map produced by sliding over the tissue using the proposed probe with an average indentation depth of 3 mm; (b) the identified locations of tumours for each experiment.

3.9 Discussion and Conclusion

This chapter presents a novel approach of stiffness measurement for tissue diagnosis based on force and vision sensing. The developed probe is composed of a force sensor and an image acquisition unit to obtain the contact area of probe-soft tissue interaction. By measuring the change of diameter of the contact area during indentation tests, the indentation depth can be estimated. By measuring indentation force and depth simultaneously, the stiffness distribution of target soft tissue can be mapped for

localization of abnormalities using the Stiffness Image based on Sliding Indentation (SISI).

The performance of the developed probe was validated through experiments on multiple materials including silicone phantoms and pork organs. The results show that the probe can perform stiffness measurements effectively when the probe indents and slides over tissue surfaces.

The probe has the potential to aid surgeons to detect the positions of tumours. Furthermore, it can also acts as an endoscope, helping the surgeons to observe organs directly without involving additional tools. Due to its simple sensing structure without any moving parts, it is easy to manufacture and the probe can be miniaturized for many biomedical applications.

However, there are several limitations of the probe. One of the limitations of the method is that the contact area will be constant after a certain indentation depth. The probe can be used to measure small deformations of soft tissue, which may result in difficulties detecting deeply embedded tumours. Secondly, it is time consuming to process a large amount of images.

Chapter 4

Parameter Estimation of Ex-vivo Human Prostate using Inverse Finite Element Analysis and Newton-Raphson Method

Chapter 4

4.1 Introduction

Prostate cancer is the most frequently diagnosed male cancer. The annual cancer statistics report from the American Cancer Society (Cancer Facts & Figures 2011) shows that there are 240,890 new cases of prostate cancer diagnosed in 2011 in the United States. Moreover, this cancer is one of the leading causes of cancer-related death in men, with 33,720 prostate cancer-specific deaths in 2011.

Many researchers have been investigating the biomedical model of the human prostate, since it is essential for diagnosing disease with different mechanical properties of normal and abnormal tissues, controlling complex tool-tissue interactions during surgery, and training in virtual surgical environment. While direct standard identification approaches such as uniaxial indentation test, tensile test (A. Samani 2004; J. Kim 2005; M. Tada 2005; C. Choi 2006; J. E. Bischoff 2008) and inflation test are widely used for determining material properties, it is often not feasible to cut human prostate tissue to produce a sample of well defined dimensions. In addition, there are more difficulties for soft tissue mechanical properties identification in in-vivo condition. For such cases, the inverse finite element method can be employed to provide a solution.

In this chapter, the inverse Finite Element and Newton-Raphson method are used to estimate human prostate tissue parameters from test data based on force-displacement measurements. In order to obtain ground truth data, the developed stiffness probe described in Chapter 3 is integrated with a robotic arm, Phantom Omni (SensAble technologies), to conduct sphere-soft tissue indentation experiments on ex-vivo human prostate tissue. Then the sphere-tissue interaction is modelled using ABAQUS^{TM} finite element software. The Arruda-Boyce hyperelastic model is used to

represent the large deformation behaviour of human prostate tissue. Inverse finite element analysis and the Newton-Raphson method are employed to identify the shear modulus (μ) of the hyperelastic model, using the static sphere-tissue indentation data as input.

This chapter is organized as follows. Section 4.2 reviews related work on hyperelastic finite element modelling with ABAQUS and inverse finite element modelling for soft tissue parameter estimation. Section 4.3 describes methods and materials for tissue parameter estimation. Section 4.4 shows results and Section 4.5 gives conclusions.

4.2 Hyperelastic Finite Element Model and Inverse Finite Element for Soft Tissue Parameter Estimation.

The FEA was proposed by M.J. Turner in 1956, and has been widely used for modelling soft tissue behaviours in many biomedical applications. The large tissue deformations during tool-soft tissue interactions can be studied by using nonlinear elastic or nonlinear hyperelastic models, for which material parameters are assumed to be non-linear, isotropic and incompressible.

A hyperelastic material is typically defined by a strain energy function, U (ε), which can be derived from the constitutive stress/strain relationships. To model Hyperelastic materials, there are several forms of strain energy function including Neo-Hookean, Ogden, Mooney-Rivlin, and Arruda-Boyce.

Since previous research implies that a relative large deformation during indentation test of soft tissue benefit the detection accuracy of tumour (K. Sangpradit 2009; K. Sangpradit 2010; K. Sangpradit 2011), the modelling of large deformation of tool-tissue interaction is necessary. Furthermore, Arruda-Boyce models was selected

since they were widely used in biomechanical soft tissue simulations (V. Vuskovic 2000; Tönuk E 2003; Tillier 2004; Kerdok, Jordan et al. 2005; K. Sangpradit 2009; K. Sangpradit 2010; K. Sangpradit 2011).

The Arruda-Boyce strain energy function is given by Equation (4.1) (ABAQUS 2008):

$$U = \mu \sum_{i+1}^{5} \frac{C_i}{\lambda_m^{2i-2}} \left(I_1^i - 3^i \right) + \frac{1}{D} \left(\frac{J_{el}^2 - 1}{2} - \ln J_{el} \right), \tag{4.1}$$

where μ is the shear modulus, λ_m is locking stretch, and C_i is the Arruda-Boyce constant defined by (ABAQUS 2008)

$$C_1 = \frac{1}{2}, C_2 = \frac{1}{20}, C_3 = \frac{11}{1050}, C_4 = \frac{19}{7000}, C_5 = \frac{519}{673750}.$$

The Arruda-Boyce equation requires two parameters, μ and λ_m. The locking stretch, λ_m, is given by Equation (4.2) (J. S. Bergstrom 1998):

$$\lambda_m = \sqrt{\frac{1}{3} \left[\lambda_{\lim}^2 + \frac{2}{\lambda_{\lim}} \right]} \tag{4.2}$$

Under a uniaxial deformation, it has been shown that the nominal strains are approximately 30% for normal tissue and thus $\lambda_{lim} = 0.7$(Bergstrom ; J. S. Bergstrom 1998; T A Krouskop 1998; Miller 2005). Hence, the locking stretch, λ_m, is calculated to be 1.05 from Equation (4.2). Then, only shear modulus μ, needs to be identified in the Arruda-Boyce model.

The shear modulus μ is one of several quantities for measuring the stiffness of materials. Based on a soft tissue model, the inverse finite element method means that unknown shear modulus μ can be estimated by minimizing the errors between finite element simulation and experimental results. There are varieties of mehods for minimizing the errors between the experimental results and the simulation results using finite element model including the sequential quadratic programming (SQP) method,

the Levenberg-Marquardt algorithm, the extended Kalman filter method and the Newton-Raphson Method (A. Samani 2004; J. Kim 2005; M. Tada 2005; C. Choi 2006; J. E. Bischoff 2008; K. Sangpradit 2010; K. Sangpradit 2011). Since the Newton-Raphson Method has been validated to be robust against measurement noise and have fast convergence properties by previous researches (Y. H. Zweiri 2004; K. Sangpradit 2009; K. Sangpradit 2010), this chapter descries the method of identifying parameters of ex-vivo human prostate tissue using inverse finite element analysis and the Newton Rahpson method.

4.3 Methods and Materials

4.3.1 Experimental setup

The Phantom Omni device (SensAble technologies) is a passive robotic arm providing 6 degrees of freedom position sensing. It was used for many applications due to its properties and availability to public, for example in (Hayn 2010) (Sankaranarayanan 2010). However, to our knowledge, it has not been used broadly combined with a haptic probe for soft tissue examination (Jichun Li 2012; Jichun Li 2012; Min Li 2012). In order to do unixial indentation test with a large deformation on ex-vivo human prostate tissue at hospital, the developed stiffness probe is attached to the stylus of the Phantom Omni device, Figure 4.1.

The Phantom Omni device provides 6 degrees of freedom position sensing. By applying forward kinematics equations using Denavit-Hratenberg algorithm, the position of the stiffness probe tip can be calculated. The coordinate frame was assigned to each joint, Figure 4.2. Since Phantom Omni can be described as a mechanical system, the kinematics relationships can be described according to frame's relative movement.

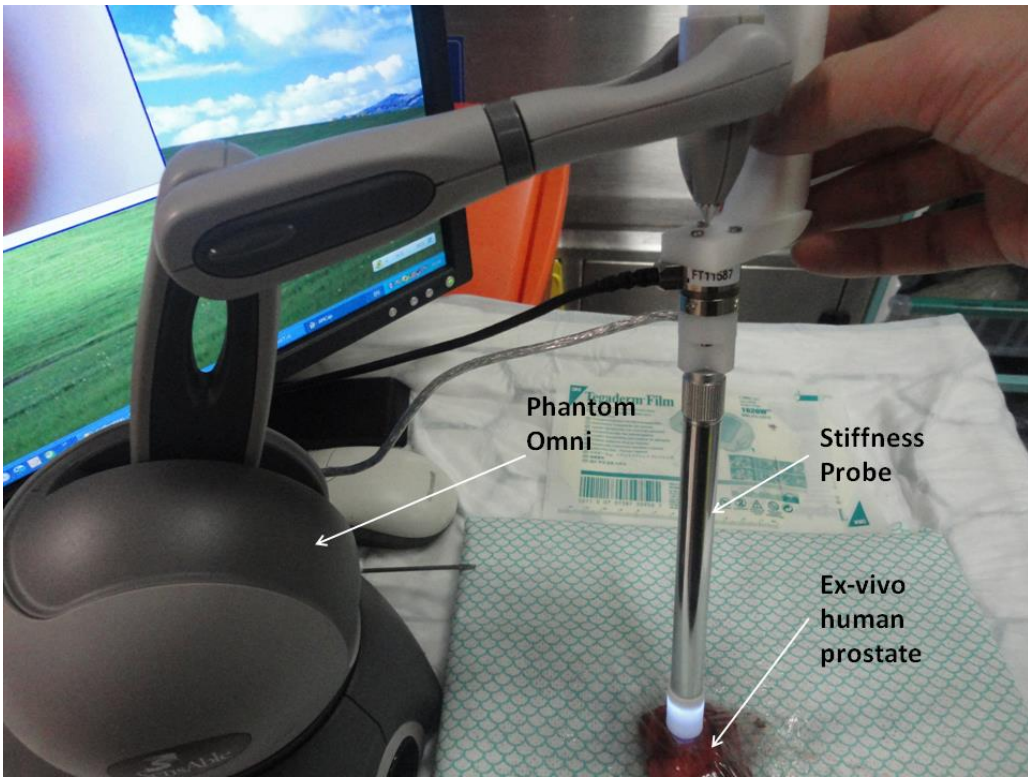

Figure 4.1: The Phantom Omni device attached with the developed stiffness probe for uniaxial indentation test on ex-vivo human prostate tissue.

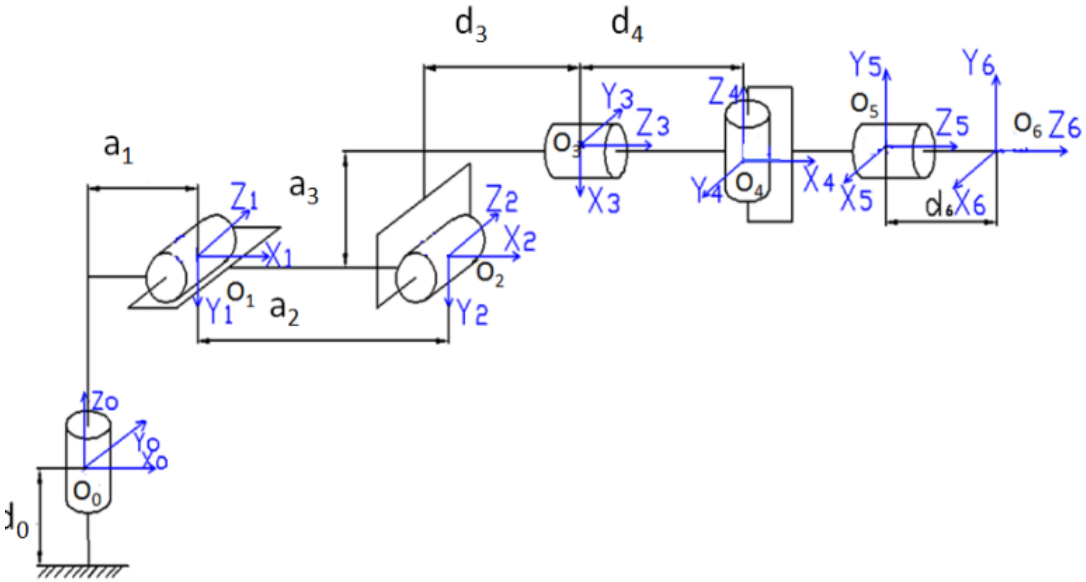

Figure 4.2: Kinematics model of the robotic platform (Phantom Omni device) (J Li et al 2012).

Then, the homogenous transformation matrixes A_i^{i-1}were used, where *i* define the number of the frame. Four parameters describe interrelation between frame *i* and *(i-1)*, three of them are construction constants and the fourth is controlling variable (θ_i). The Denavit-Hartenberg parameters are shown in Table 4.1.

Table 4.1： Denavit-Hartenberg Parameters

Frame（O*i*）	α_i	a_i	d_i	θ_i
O*0*	0	0	d_0	0
O*1*	-90º	a_1	0	θ_1
O*2*	0	a_2	0	θ_2
O*3*	90º	a_3	d_4	90º +θ_3
O*4*	-90º	0	0	θ_4
O*5*	90º	0	0	90º +θ_5
O*6*	0	0	d_6	θ_6

There are six frames for the Phantom Omini, thus i=6 and six transformation matrixes can be given by Equation (4.4) to Equation (4.9). For simplicity the following trigonometric identities were given by: $\cos(\theta_i)= c_i$ and $\sin(\theta_i)=s_i$.(J. Zirjakova 2011).

$$A_i^{i-1} = \begin{bmatrix} \cos\theta_i & -\sin\theta_i\cos\alpha_i & \sin\theta_i\sin\alpha_i & \alpha_i\cos\theta_i \\ \sin\theta_i & \cos\theta_i\cos\alpha_i & -\cos\theta_i\sin\alpha_i & \alpha_i\sin\theta_i \\ 0 & \sin\alpha_i & \cos\alpha_i & d_i \\ 0 & 0 & 0 & 1 \end{bmatrix} \tag{4.3}$$

$$A_1^0 = \begin{bmatrix} c1 & 0 & -s1 & a_1c1 \\ s1 & 0 & c1 & a_1s1 \\ 0 & -1 & 0 & 0 \\ 0 & 0 & 0 & 1 \end{bmatrix} \tag{4.4}$$

$$A_2^1 = \begin{bmatrix} c1 & -s2 & 0 & a_2c2 \\ s1 & c2 & 0 & a_2s2 \\ 0 & 0 & 1 & 0 \\ 0 & 0 & 0 & 1 \end{bmatrix} \tag{4.5}$$

$$A_3^2 = \begin{bmatrix} c3 & 0 & s3 & a_1c3 \\ s3 & 0 & -c3 & a_1s3 \\ 0 & 1 & 0 & 0 \\ 0 & 0 & 0 & 1 \end{bmatrix} \tag{4.6}$$

$$A_4^3 = \begin{bmatrix} c4 & 0 & -s4 & 0 \\ s4 & 0 & c4 & 0 \\ 0 & -1 & 0 & d_4 \\ 0 & 0 & 0 & 1 \end{bmatrix} \tag{4.7}$$

$$A_5^4 = \begin{bmatrix} c5 & 0 & s5 & 0 \\ s5 & 0 & -c5 & 0 \\ 0 & 1 & 0 & 0 \\ 0 & 0 & 0 & 1 \end{bmatrix} \tag{4.8}$$

$$A_6^5 = \begin{bmatrix} c6 & -s6 & 0 & 0 \\ s6 & c6 & 0 & 0 \\ 0 & 0 & 1 & d_6 \\ 0 & 0 & 0 & 1 \end{bmatrix} \tag{4.9}$$

The resultant homogenous matrix, which defines position and orientation of the probe tip in absolute coordinate's calculation, is given by Equation ((4.10). Knowing coordinates of tip trajectory it is possible to obtain whole path of indentation probe.

$$A_6^0 = A_1^0 * A_2^1 * A_3^2 * A_4^3 * A_5^4 * A_6^5 \tag{4.10}$$

Figure 4.3 shows the schematic of the designed test rig. Experimental data of positions and force from the probe are acquired using custom designed software using C++ programming language. The image processing software as described in Chapter 3 is used for capturing contact area between the probe and human prostate tissue. The PCI Data Acquisition Card (NI PCI 6034E, which is a 16-bit DAQ card) is used for force data acquisition.

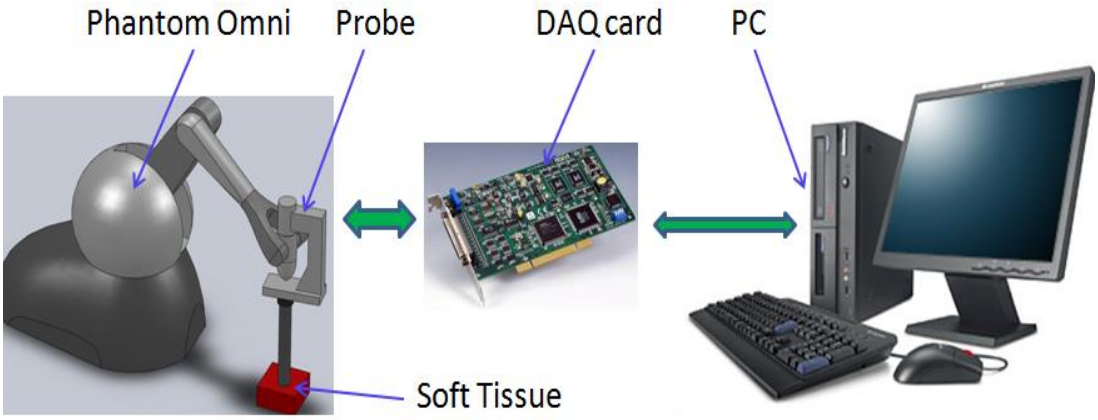

Figure 4.1 : Schematic of the test rig. The test rig consists of a PC, a DAQ system for force and displacement measurement , a Phantom Omin robotic arm and the developed probe.

4.3.2 Newton- Raphson method

The Newton Raphson method works by modifying an initial estimate iteratively and gives at a converged solution after several iterations. Generally, the iterative process stops when the error between predicted and measured data falls below a pre-defined threshold. In this study, uniaxial indentation experiments were conducted on prostate tissue and the Newton-Raphson method to identify the shear modulus, μ, corresponding to a finite element model.

The residual error, e, is defined as the difference between FE predicted and the measured force-displacement curves (F_M and F_{FE} respectively)(K. Sangpradit 2009; K. Sangpradit 2011),given by Equation (4.11):

$$e = \frac{1}{n}\sum_{j}^{n}\left(F_M - F_{FE}\right)^2 \tag{4.11}$$

The Newton-Raphson method is used to minimize the error function, given by Equation (4.12):

$$P_{i+1} = P_i - J^{-1}\left[e_1\left(p_1, i_1\right)\right] \tag{4.12}$$

where $J = \left[\frac{\partial e_1}{\partial P_1}\right]$, e is the error between the FE predicted and the measured results. P is parameter to be estimated (here is the shear modulus, μ):.

The inverse analysis starts with two initial guesses of the shear modulus, μ_0 and μ_1. Then the value of μ at the kth iteration is calculated using Equation (4.13):

$$\mu_{k+1} = \mu_{k-1} - \left(\frac{\mu_{k-1} - \mu_k}{e_{k-1} - e_k}\right) e_{k-1} \tag{4.13}$$

The iterations are terminated when e_k falls below a pre-defined threshold valve, δ.

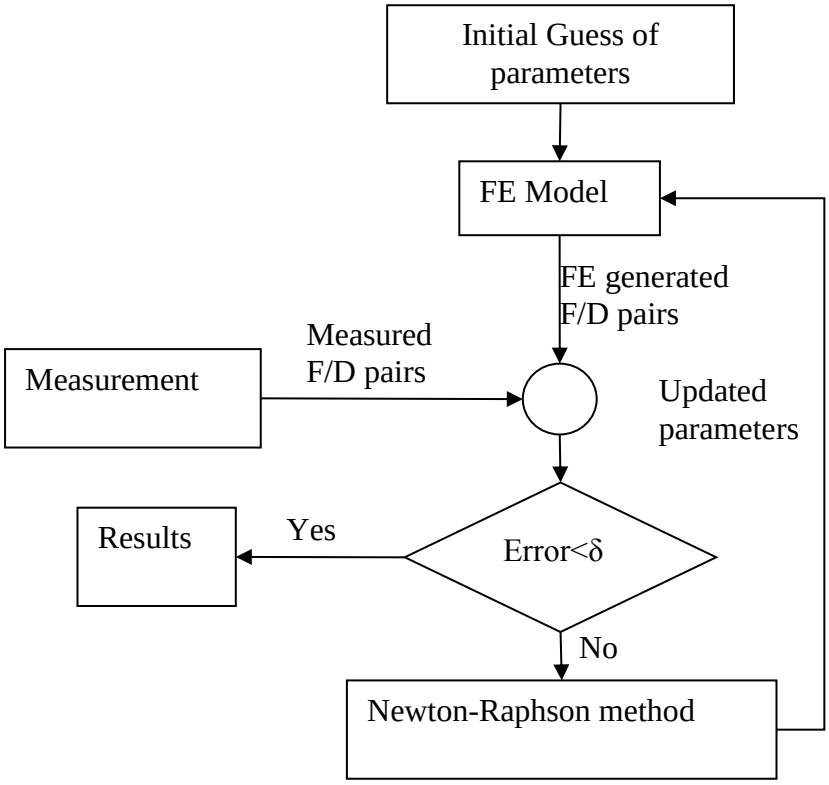

Figure 4.4: Flow chart of the inverse finite element model based on the Newton-Raphson method for parameter identification.

Figure 4.4 shows a flow chart of the inverse finite element model based on the Newton-Raphson method for parameter identification.

4.3.3 Experimental protocol

In order to estimate unknown shear modulus μ of human prostate using the inverse finite element method and the Newton-Raphson algorism, an experimental protocol is listed as follows:

1) The stiffness probe with a 10 mm spherical head indents into the ex-vivo human prostate at a predefined position by 4mm. The reaction force and the displacement signals are recorded.

2) The geometry curve passing the pre-defined position of the tested human prostate is measured using the developed passive robotic

platform. Then the geometry data is imported into SolidWorks to produce the 2D geometry of prostate for the finite element simulation.

3) Modelling the ex-vivo human prostate using the Arruda-Boyce model. An FE analysis of the uniaxial indentation process was performed with the aim of obtaining the force-displacement curves, $F_{FE.}$

4) An inverse FE analysis is used to identify the shear modulus of ex-vivo human prostate by minimizing the error between the finite element and experimental data

4.3.4 Modelling of ex-vivo human prostate

Figure 4.5 (a) shows the indentation test on an ex-vivo human prostate and the yellow area is a pre-defined test position. Figure 4.5 (c) shows the 2D finite element simulation of the prostate using ABAQUS software package.

The prostate model is constrained on the ground while the indenter is modelled as a rigid cylindrical wheel with 10 mm diameter, Figure 4.5 (b). The contact between the indenter and the prostate is modelled using a frictionless “contact pair”. The finite element mesh consists of 287 four-node bilinear plane stress quadrilateral elements, with reduced integration and hourglass control (CPS4R in ABAQUS). The indenter is modelled as a 10 mm diameter 2D-circle with 25 elements of the two- node 2D linear rigid link (ABAQUS element R2D2).

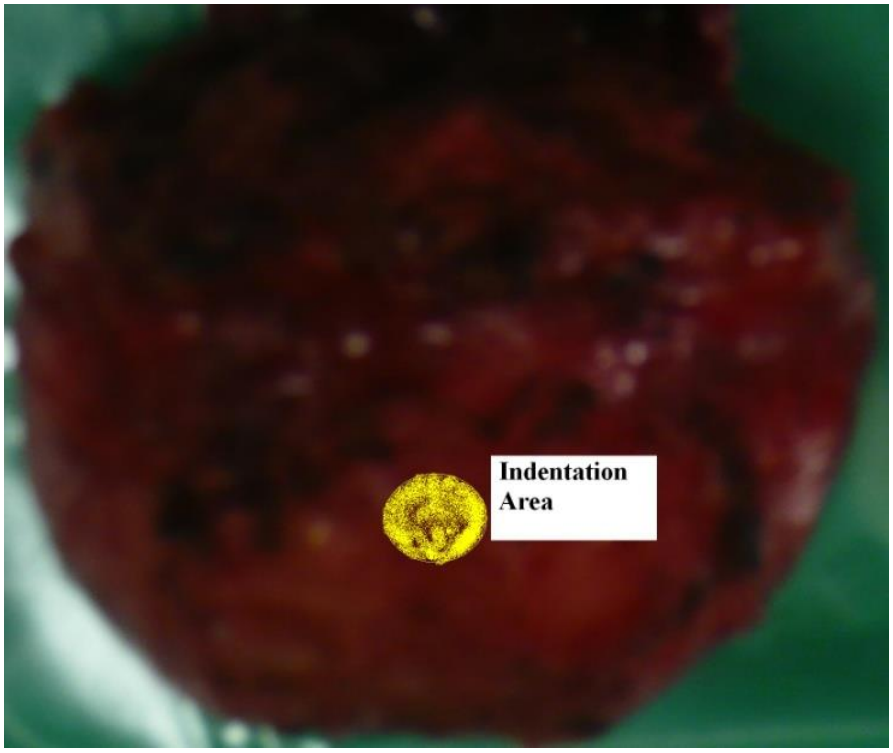

(a)

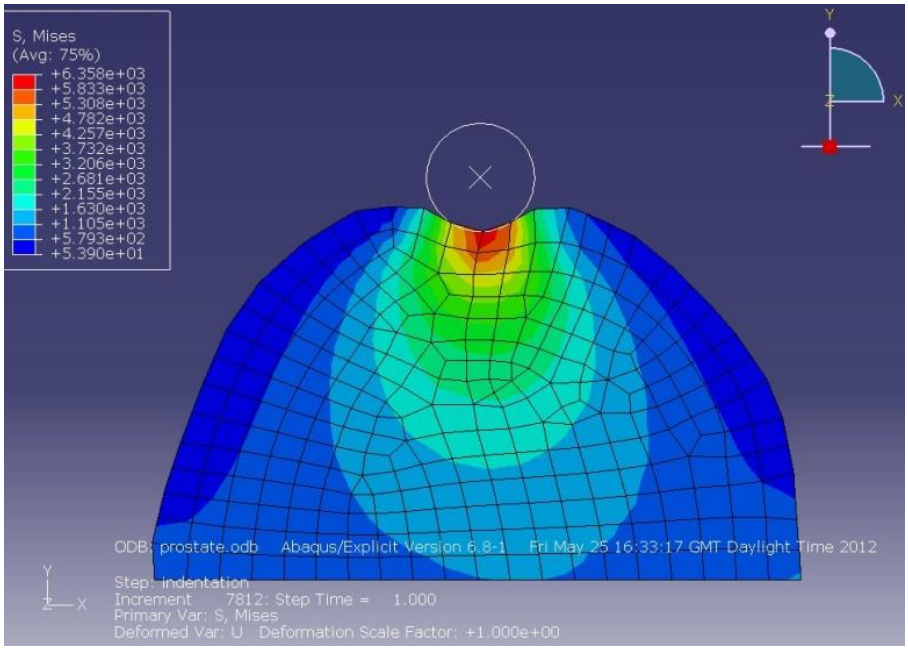

(b)

Figure 4.5: (a) The indentation experiments on a prostate. The yellow area shows the pre-defined tested area. (b) The 2D finite element model of the human prostate.

4.3.5 Inverse Finite Element Analysis

An inverse FE analysis is carried out to identify the shear modulus of the human prostate tissue by minimizing the error between the finite element and experimental data. The threshold of the RMS error was set as 0.05%.

The inverse analysis starts with two initial guesses, μ_0 and μ_1, for the unknown parameter. The error between the finite element simulation curve and the measured curve is calculated using Equation (4.12) .and the unknown parameter is updated using Equation (4.13). The process is iteratively repeated until the solution converges.

Five sets of initial values (μ_0 and μ_1), A (μ_0= 1800, μ_1=900), B (μ_0= 500, μ_1=1000), C (μ_0=5000, μ_1=3000), D (μ_0=4000, μ_1=2500), E (μ_0=10000, μ_1=8000), were used for the simulations to evaluate the sensitivity to initial conditions. One iterative solution requires approximately 1 minutes of computational time on a 2.99 GHz Pentium(R) D machine with 3.23 GB of RAM, for convergence of the parameter estimation algorithm.

4.4 Results

Table 4.2 lists the converged values for each initial guess, computational time, number of iteration, and the parameter prediction error. It is noted that sets A–E converge to the actual value. It is also noted that the method takes fewer than 8 iterations to converge for a range of initial gausses, with time consumed not greater than 16 minutes, and the RMS errors range is less than 0.05%. Results showed that the final estimated prostate shear modulus is in agreement with experimental results, Figure 4.7.

Table 4.2: Prostate shear modulus estimation using Newton-Raphson and inverse finite element method.

Initial Guess (kPa)	Estimated μ (kPa)	Estimation Error %	No. of Iterations	Computation time (minute)
A.μ_0=1.8,μ_1=0.9	2475	0.04	4	8
B. μ_0= 0.5,μ_1=1.0	2459	0.04	5	10
C.μ_0=5.0, μ_1=3.0	2531	0.04	3	6
D. μ_0=4.0, μ_1=2.5	2500	0.05	1	2
E. μ_0=10.0, μ_1=8.0	2401	0.04	8	16

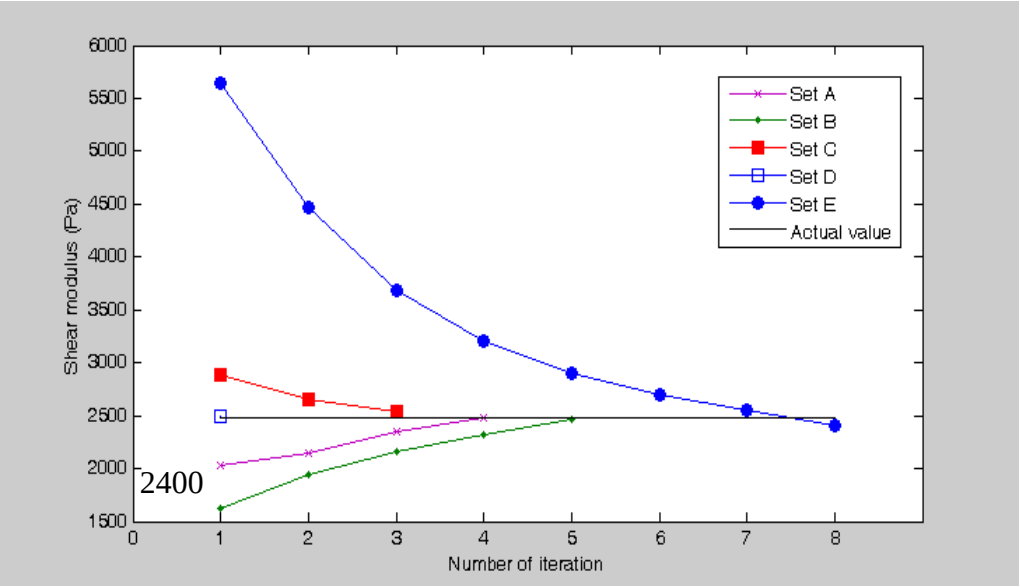

Figure 4.6 : Convergence rates for the 5 initial value sets for prostate.

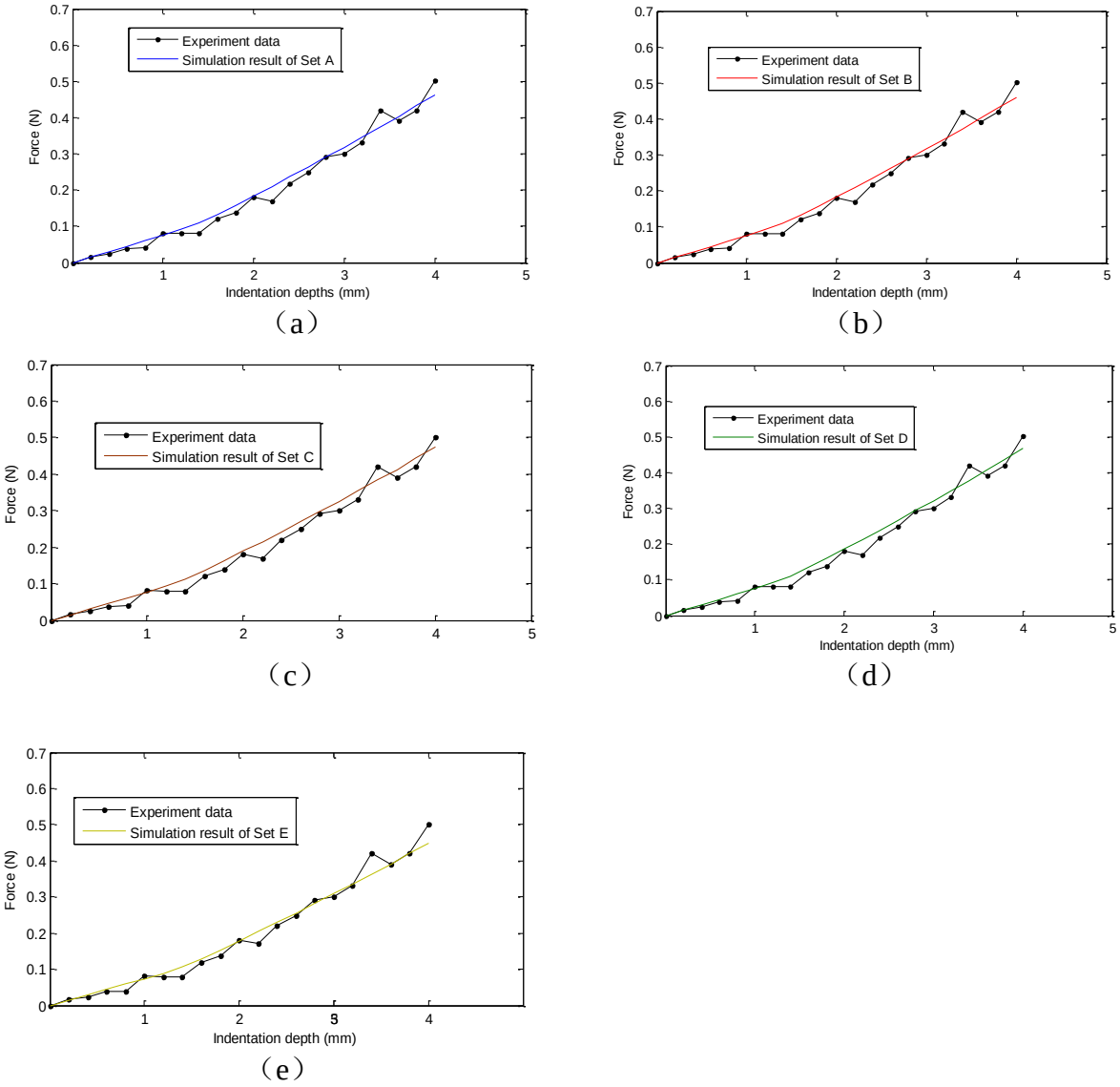

Figure 4.7: Finite element and experimental results using final estimated parameter for five sets of initial condition for human prostate tissue (a-e).

4.5 Conclusions

This chapter applies inverse finite element analyses and the Newton Rahpson method to estimate the shear modulus of ex-vivo human prostate tissue. Experiments were conducted using a developed passive robotic platform integrating the developed stiffness probe (which is so-called sliding indenter robot). The Arruda-Boyce model was adapted for modelling the ex-vivo prostate tissue and the Newton-Raphson method

is used for estimating the shear modulus. The results in Figure 4.6 and Figure 4.7 show that the shear modulus of prostate is about 2400Pa and the force-deflection curve generated from the identified of parameters is in good agreement with the experimental measurements.

Chapter 5

Clinical Study of Ex-vivo Prostate Tissue Mechanical Characteristics for Prostate Tumour Identification

Chapter 5

5.1 Introduction

Digital Rectal Examination (DRE) is one of the most common screening tests used to diagnose prostate cancer(Ahn BM 2010). According to the National Cancer Information Service, most prostate tumours are accessible from the posterior, and cancer tissue is grittier and firmer than normal tissue. The clinician inserts a finger wearing a glove into the patient's rectum, whereby he or she can detect a malignancy using haptic feedback. Prostate cancer is therefore detectable using a DRE. This test therefore has low risk, prompt availability, and is cost effective(Ahn BM 2010). Despite these advantages, the results of a DRE are not quantitative and depend on the expertise of the clinician. In order to overcome this problem, robotic palpitation has been investigated by researchers to measure the properties of human prostate. For robotic palpation, one common method used to measure the mechanical property of tissue is indentation.

A variety of master-slave robotic systems attached with medical probes, capable of providing haptic feedback through kinaesthetic sensing have been developed (Rosen and Hannaford 1999; Trejos, Jayander et al. 2008; H.Liu 2011). For such systems driven by industrial robot, the accurate control of the motion could be achieved. It is relatively easy solution for laboratory experiments, as the path of the probe can be pre-programmed and the performance is evaluated under the same conditions. However, it is an expensive and difficult alternative for surgeons. Moreover, it does not give the possibility to detect organ curvatures and easily change the measurement path, in order to compose an accurate 3D representation. In addition, moving parts of the probes could reduce the reliability and could be difficult to fabricate in mass production. From the other side, many hand-held devices are developed to measure the mechanical feedback of soft tissue. Such systems showed good accuracy and feasibility. However, they were

designed to carry out local stiffness measurement and not capable of generating 3D stiffness representation.

In order to overcome the weaknesses of the devices mentioned above, we have proposed a novel portable passive robotic platform, called a sliding Indenter robot(Jichun Li 2012; Jichun Li 2012). Using this device to measure both the mechanical properties and geometry of samples, we created a three dimension stiffness image of ex-vivo soft tissue. This system is low cost, mobile, and minimal training is required for use. Experiments using our system were performed on human prostates in which we estimated the elasticity of the sample tissues. This was in order to determine whether there was a measurable difference in the mechanical properties of ex-vivo cancerous and non-cancerous prostate tissue.

This chapter is organized as follows. In section 2, the materials and methods are described. In section 3, we discuss experimental results. Finally, discussions and conclusions are drawn in section 4.

5.2 Materials and Methods

5.2.1 Slidling Indenter Robot

As described in Chapter 4, The Phantom Omni haptic device (SensAble technologies) was used for combining with the developed stiffness probe for soft tissue stiffness examination.

Phantom Omni is a robotic device with range of motion set by hand wrist movements and with nominal positional resolution of 0.055 mm. Three potentiometers and three encoders read the outputs of the device - six variable angles – three joint angles for translation and three gimbal angles for rotation. The user is able to set any

necessary trajectory of the probe, thus, making soft tissue examination more effective. It is possible to capture the curvature of a soft tissue and to detect hard formations more accurately. Combining the geometry information from the Phantom Omni device and the information about the mechanical properties of soft tissue from the probe, a three-dimensional scanning of soft tissue can be obtained.

The indentation probe for force and stiffness measurements is attached to the stylus of the device. Force data from the probe are acquired using custom designed software and associated PCI Data Acquisition Card (NI PCI 6034E, which is a 16-bit DAQ card). Indentation depth data was obtained using the image processing software as described in Chapter 3.

5.2.2 3D Stiffness map

To validate the performance of tissue abnormality identification, sliding indentation tests were performed on ex-vivo human prostates. The developed stiffness probe slid over the surface of the prostates. During this process, the stiffness and trajectory are recorded. Then, stiffness feedbacks at each sampled location are combined together to generate a colour-coded mechanical image, Figure 5.1 Since the image indicates the stiffness distribution within the soft tissue, the location of the tumours can be identified. It can be seen from Figure 5.2 that the sliding indenter robot is possible to produce a 3D stiffness map of human prostate tissue.

Nowadays, biopsy results provide information about tumour location for surgeons during operation. The test is performed on six prostate segments, therefore, for the comparison studies it was necessary to divide stiffness map into six parts. Each segment contained information about tissue condition – either it was healthy tissue segment or it contained tumour, Figure 5.3.

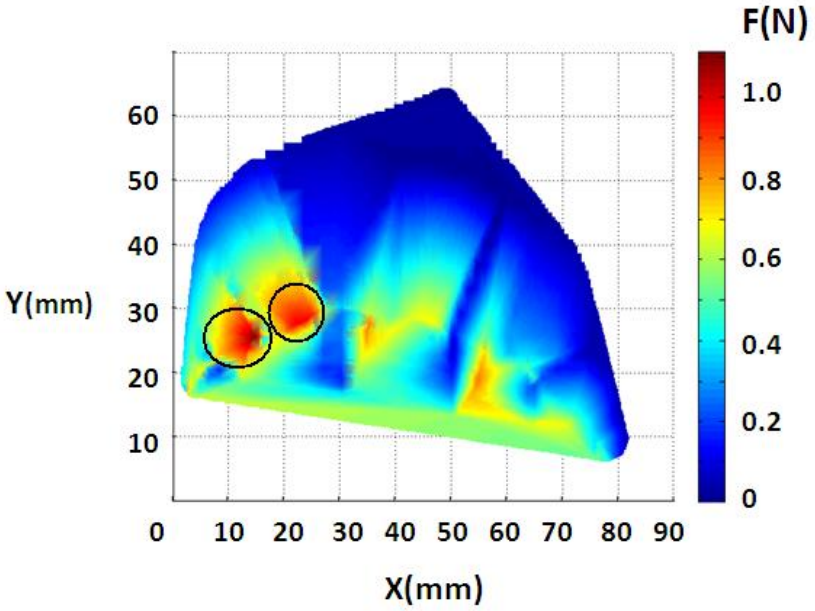

Figure 5.1: 2D stiffness map of prostate. The circles imply the cancerous area with higher stiffness with the prostate.

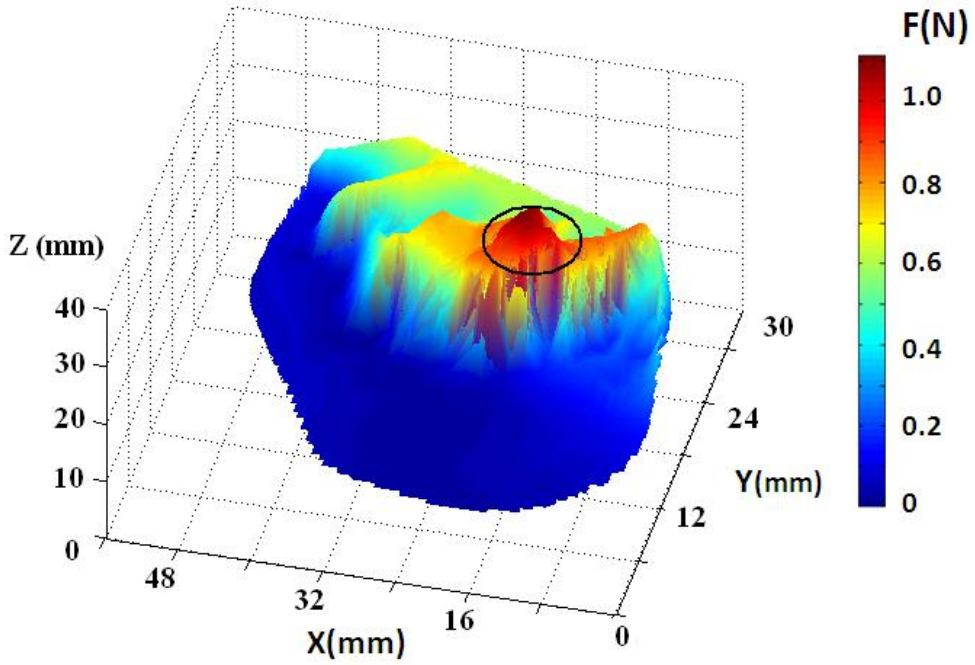

Figure 5.2: 3D stiffness map of an ex-vivo human prostate. The circle implies the cancerous area with higher stiffness with the prostate.

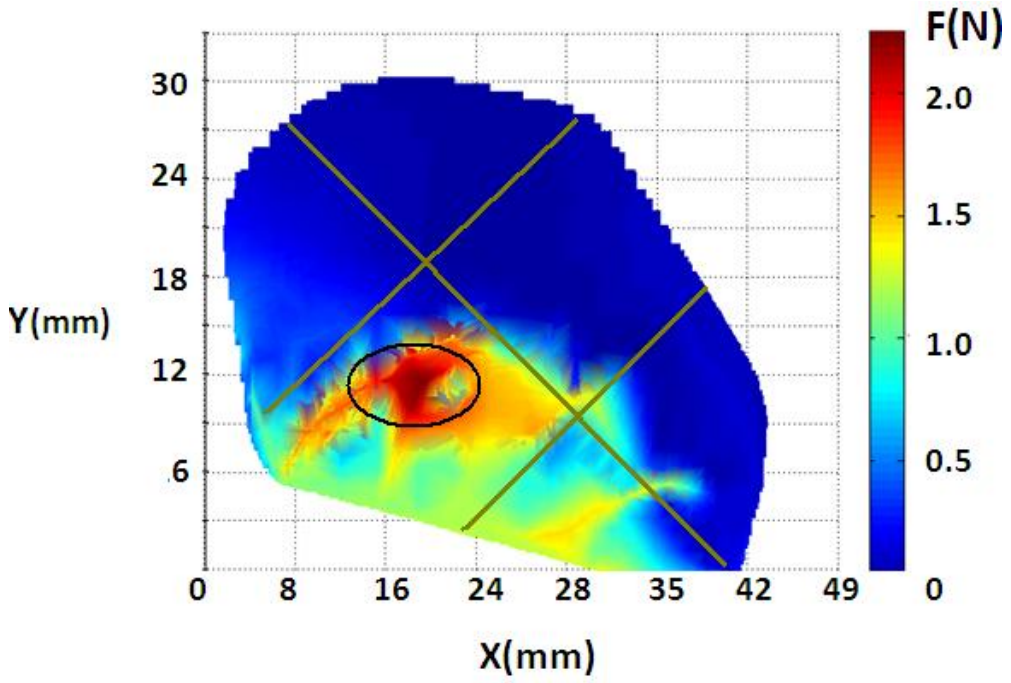

Figure 5.3: Stiffness map subdivision into six segments

5.2.3 Patients and samples

35 patients from Guys and St Thomas Hospital, London, donated prostate tissue for the purposes of this experiment. The study was given full ethical approval to be conducted at the Department of Urology and Histopathology, Guys and St Thomas Hospital and the donators provided written informed consent allowing the post-operative examination of the extracted prostate samples. All patients had undergone radical prostatectomy between January 2011 and January 2012. Patients with clinically insignificant small cancer (<0.5 mL) were not included in the sample. Patients whose prostates had been altered by prostate-related surgery, preoperative hormonal therapy or radiation therapy were also excluded from the study. After these criteria were

accounted for, 21 prostate specimens of those collected were eligible for analysis. The mean preoperative volume of prostates was 45.8±18.4mL. The mean PSA level was 8.5±3.4 ng/mL. The prostate cancer specimens were divided into the pathologic findings. The clinical stage of the prostate cancer obtained with this system was T2b in 5 patients; T2c in 6 patients; T3a in 10 patients. The mean age of patients was 64.2±5.2 years old.

5.2.4 Experiments

In the mechanical experiments carried out on the sample tissue, the sliding Indenter robot was used to measure the tissue behaviour against mechanical loadings. The investigator who performed the experiments was blind to the clinical data. The clinical expert determined the divided sites of specimens. The sliding indentation experiments were carried out on the extracted human prostates, within 60 minutes after extraction of the specimen in the operating room. It takes about 5 minutes to finish scanning of a proste.

A total of 126 areas were recorded for comparison with clinical results on the 21 specimens, after which the average volume and weight were measured and recorded.

After indentation tests, the specimens were sent to the pathology department for histological examination at Guys and St Thomas Hospital, London, upon completion of the experiments. The specimens were prepared by fixing in formalin and were then examined using an optical microscope, by a single pathologist. The pathologist was blind to the results of stiffness image and determined and documented the location and size of the cancer tissues for all specimens. A total of 126 areas were recorded for comparison with clinical results on the 21 specimens. Fig .7 shows a comparative result of stiffness image with clinical reporting proformas on a selected prostate.

5.2.5 Mechanical property estimation

The elastic modulus (E) is used to present the mechanical properties of the biologic tissues. Uniform deformation and friction-free contact were assumed to permit sliding of the tissue across the indenter surface. The elastic modulus equation, Equation (5.1), was applied to estimate the elastic modulus of the tissue from the experimental results when the indenter contacted completely with the tissue (A. Gefen 2005).

$$E = \frac{3f(1+\nu)}{8d_i\sqrt{rd_i}}, \quad (5.1)$$

Where E is the elastic modulus, f is the tissue reaction force normal to tissue surface, r is the radius of the sphere, d_i is the indentation depth and v is the Poisson ratio. For incompressible material, v =0.5.

5.2.6 Statistical Analysis

SPSS Statistics version 17.0 was used to perform statistical analyses. The elastic modulus was presented as mean±standard deviation in kPa. The two samples independent t-test was used to determine the significance of the elasticity differences between the cancerous and normal tissues.

5.3 Results

A total of 126 sites of 21 prostates obtained from male patients who underwent robot-assisted radical prostatectomy were examined. The stiffness map generated using SIRI was correlated with the finding of DRE, MRI and TRUS biopsy results using a proforma. Two separate persons collected data on the proforma using stiffness image and the other modalities (DRE, MRI and TRUS) respectively. Figure 5.4 shows a three dimensional color-coded stiffness image which indicates the stiffness distribution and

tumor locations of a human prostate, where the tumor shows up as distinctly red colored areas (higher stiffness).

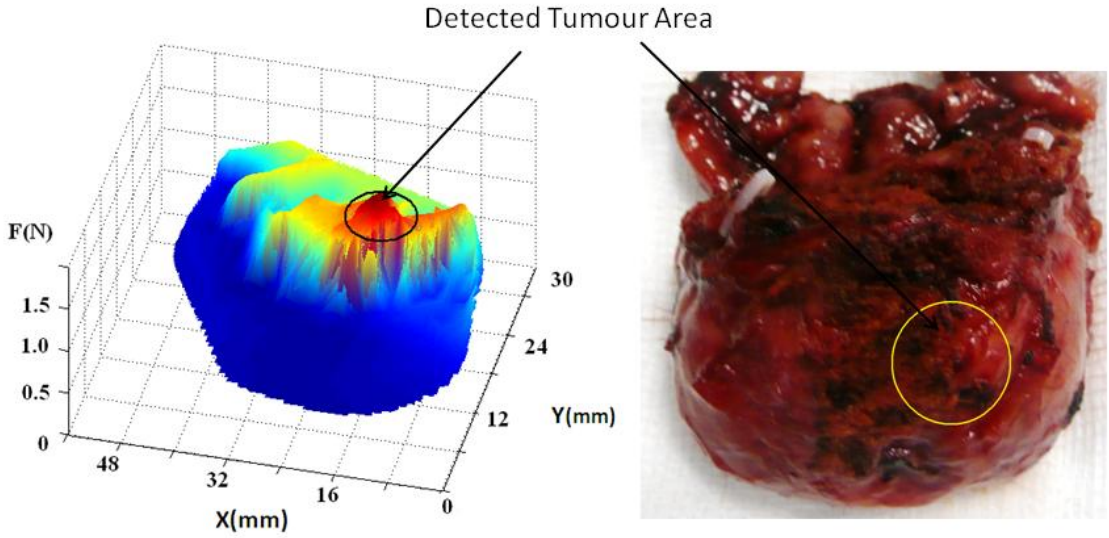

Figure 5.4: Three dimensional stiffness image of the examined prostate obtained from rolling indentation experiment on a selected prostate (left) and tumor area highlighted on photographic image of the same prostate (right).

The performance of each test to detect prostatic cancer was assessed by comparing the test results with the final histology. The accuracy, sensitivity, specificity and the negative predictive value for tumour detection were calculated, Table 5.1.

Table 5.1: Accuracy of prostate tumour detection using different tests

Test	Sensitivity (%)	Specificity (%)	NPV (%)
DPE	34.8	66.7	48.2
MRI	34.9	82.5	55.9
TRUS	76.2	51.6	68.1
Stiffness image	45.9	78.2	64.3

In our study, stiffness image has a high specificity (78.2%) with a 64.3% positive predictive value. This implies that a positive result detected by stiffness image means a high probability of the presence of prostate cancer. The results are helpful for a surgeon to localize the position of prostate tumour during surgery. When utilizing tests for tumour detection, a high negative predictive value is desirable as it is essential that the tests used for detection do not miss diagnosis of cancer. Both stiffness image and TRUS were able to demonstrate similar negative predictive values and performed better than the other tests.

DRE is the commonest examination undertaken to detect prostatic cancer. In the current literature, the sensitivity and specificity of prostate tumour detection with DRE range from 27.1% to 53.2% and 49 % to 91% respectively (Schröder FH 1999; Crawford ED 1996). In our study, DRE has a specificity of 66.7%, and a sensitivity of 34.8%. The results are within the range of the current literatures. In our study, SIRI has a greater accuracy than DRE with regards to all used performance indicators for prostate tumor localization. These results can be explained by the fact that the force sensitive probe makes use of a force sensor with a high resolution (0.003N). In robot-assisted MIS, it is not possible for the surgeon to directly palpate the tissue and get haptic feedback to locate a tumor, due to the small diameter of the access incisions. Hence, stiffness image is a suitable substitute for DRE and due to the small size of the sensor head it can be employed during MIS to reach prostate surfaces that cannot be accessed by the human hand directly. In addition, stiffness image can precisely measure the biological behaviour of prostate tissues, estimating mechanical properties of prostate tissue quantitatively.

In the current literature, the sensitivity and specificity of MRI in the detection of prostate cancer range from 13% to 96% and 44.3 % to 97% respectively (Purohit RS

2003; Kirkham APS 2006; Peter R Carroll 2005). In our study, MRI has higher specificity (82.5%) than SIRI (78.2%). However, stiffness image (45.9%) is better than MRI (34.9%) achieving a 10% higher sensitivity. The results also demonstrate that stiffness image performs better for a negative result when detecting prostate tumour. Moreover, stiffness image performs similarly to MRI for indicators such as negative predictive value, positive predictive value and accuracy. Figure 5.5 shows the test results on a human prostate with a tumour detected by stiffness image and pathology, while it is invisible for MRI.

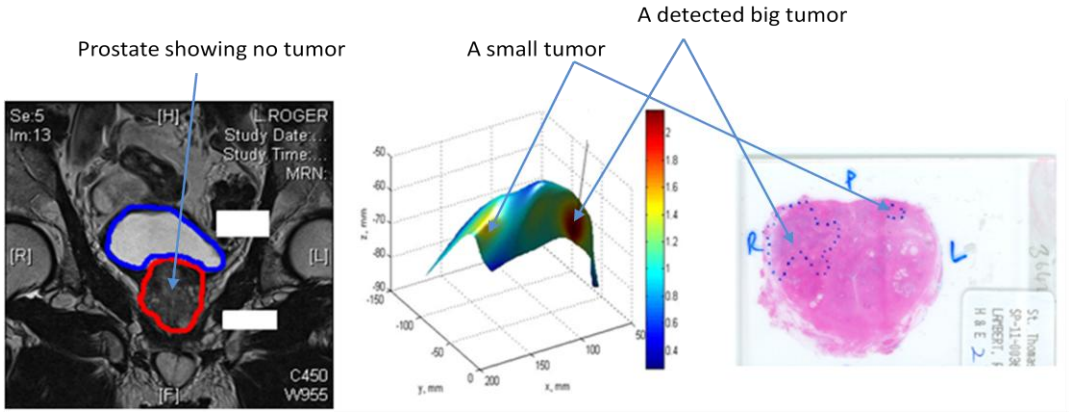

(a) (b) (c)

Figure 5.5: (a) MRI results - no tumour visible. (b) RISI shows that there is one large tumour and one suspicious small tumour. (c) The pathology examination shows that there is one big tumour and one small tumour.

In the current literature, the sensitivity and specificity of prostate tumour detection with TRUS range from 49% to 87 and 38 % to 93% respectively (Peter R Carroll 2006; Amiel GE 2006; Pallwein L 2007). The results in our study show that the measures are with the range. The results showed that TRUS biopsy had higher sensitivity (76.2%) than stiffness image (45.9%), which demonstrated that TRUS biopsy performed better for a negative result when detecting prostate tumour. However, stiffness image (78.2%) was better than TRUS (51.6%) with a 26.6% increase in

specificity. The results implied that stiffness image performed better than TRUS biopsy when detecting the presence of prostate cancer.

Stiffness image can be used to localize prostate tumour by measuring the stiffness distribution along the surface of organs. However, with this technique, it is difficult to detect small tumours buried deep within the prostate because force feedback method has its limitations due to constraint on the amount of pressure one can exert to reach deep. Further technical advances in the type of sensor and modelling of tool-tissue interaction may overcome this issue and allow better tumour detection. This pilot study demonstrates the potential of SIRI to detect prostatic cancer. Further evaluation of this technique on more samples is recommended to demonstrate its use in vivo.

Figure 5.6 shows the outcome of a study comparing the results of our sliding indentation experiments with the clinical reporting proforma on a selected prostate conducted by clinicians at Guy's Hospital.

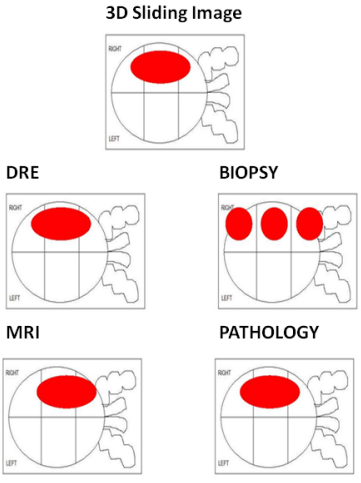

Figure 5.6: A comparative result of sliding indentation with clinical reporting proforma on a selected prostate.

Chapter 5

The conducted experimental study shows that there was good correlation of the outcome of our sliding indentation based method with the clinical reporting proforma, in particular for index lesions greater than 1 cm in size.

The sliding indentation experiment was used to obtain the elastic modulus of 126 regions and the mechanical analysis results were compared with the pathologist's reports.

126 regions of 21 prostates specimens included the cancer tissues as determined by the histological examination. The majority of the cancer tissues were located at the base of prostate (39.7%), while mid-gland occurrence was second most common (35.3%) followed by cancers in the apex of the prostate (25.0%).

The results indicated that the region containing cancerous tissue increased the elastic modulus. The mean elastic modulus of the normal and cancer tissues were 18.67 ± 5.21 and 34.67 ± 9.29 kPa at a 3mm indentation (P=0.000). For non-cancerous areas of the prostate, region 1 demonstrated the greatest elastic modulus (20.33 kPa) followed by the region 2 (20.11 kPa), region 3 (18.91kPa), region 5 (18.53 kPa), region 4 (17.66 kPa), and region 6 (15.55 kPa). In the regions with cancerous tissue, the region 6 demonstrated the greatest elastic modulus (44.01 kPa), followed by the region 3 (35.01 kPa), region 4 (34.76 kPa), region 1 (32.33 kPa), region 5 (32.13 kPa) and region 2 (29.55 kPa).

The elastic modulus of normal and cancer tissues showed significantly different from the t-test results (p=0.000). All these results demonstrates that the cancer tissue was harder than normal tissue for all regions and the results confirm the ability to differentiate cancer tissues from normal tissues based on elastic modulus. The elastic modulus and t-test results are listed in Table 5.1.

Table 5.1: Elastic Modulus and t-Test Results of Normal and Cancer Prostate Tissues

	Elastic modulus (kPa)						Independent t-test		
	Healthy tissue			Cancerous tissue				95% confidence interval of the difference	
Region of prostate	n	Mean	SD	n	Mean	SD	p-value	lower	upper
1	21	20.33	4.56	9	32.33	7.56	0.000	-16.32	-10.32
2	15	20.11	5.12	11	29.55	8.72	0.000	-19.32	-13.32
3	14	18.91	4.01	8	35.01	8.11	0.000	-15.32	-9.32
4	8	17.66	5.7	10	34.76	9.4	0.000	-26.32	-20.32
5	9	18.53	6.02	6	32.13	10.92	0.000	-22.55	-16.55
6	6	15.55	5.83	8	44.01	11.03	0.000	-21.33	-15.33
Average		18.67	5.21		34.67	9.29			

5.4 Conclusion

In this chapter, we utilize stiffness image to identify cancerous tissues by employing a sliding indenter robot. We described the working principle and results of the sliding indenter robot for ex-vivo tissue diagnosis used for three-dimensional scanning. The platform consists of Phantom device and a stiffness probe. It was shown, that the setup is suitable for quantitative assessment of the mechanical properties of soft tissue ex-vivo specimen.

The sliding indenter robot is specially created for soft tissue ex-vivo examination and allows user to validate the feasibility of the probe before in-vivo tests.

The experimental results show good feasibility of the setup to generate 3D stiffness maps for ex-vivo tissue examination and to detect embedded tumours.

Knowledge of the precise tumour location may help decrease tissue trauma and damage of sensitive structures during surgery and radiotherapy. Generally, the use of TRUS for tumour localization is limited, since up to 30% of prostatic cancer tumours are not being detected. Hence, TRUS is widely used for guiding needle biopsies. Although there have been great advances in MRI for localization of prostate cancer in recent years, the use of MRI is still controversial (Hashim U. Ahmed 2009). DRE is one of the most frequently used approaches to localize prostate cancer. Advantages of DRE include low risk, prompt availability and cost effective. However, DRE has a low sensitivity for the detection and it depends much on the expertise of the clinician (Mistry K 2003). Many researchers are developing new instruments replacing the DRE by acquiring stiffness information for MIS. Stiffness image is a novel method with rapid high efficiency and enhanced sensitivity for tissue tumour localization. The aim of this study is to compare the accuracy of SIRI for localization of prostate tumour to that of DRE, MRI and TRUS biopsy.

When comparing the tumour detection with stiffness image to DPE, the sensitivity and specificity were higher. The negative predictive value was also better with stiffness image. Hence, the prostate tumour detection was more accurate and reliable using stiffness image.

Comparing the efficacy of stiffness image with MRI, it was more sensitive but less specific than MRI. . However, both the negative predictive value and positive predictive value were similar. The TRUS biopsy had higher sensitivity but lower

specificity than stiffness image. However, the negative predictive values of both tests were similar.

The experiments estimated the elasticity of human prostates as a quantitative variable by sliding over various regions of the posterior surface. The resulting data show that there is a difference in the mechanical properties that normal and cancerous tissue across various regions of the prostate.

Chapter 6

Development and Validation Test of a Second Generation Probe Using Optic-Fibre Techniques

6.1 Introduction

Manual palpation is an essential tool for many surgical procedures since it provides rich information on the mechanical properties of soft tissue. Since there is usually a notable difference in compliance between benign and malignant tissue (a malignant tumour is typically stiffer than the surrounding parenchyma). in minimally invasive surgery (MIS), the restricted access to the surgical field precludes manual palpation.

As described in Chapter 3, the first generation prototype of stiffness probe is equipped with a commercial force/torque (F/T) sensor (Nano17, SI-25-0.25, ATI Industrial Automation). However, this sensor is of relative large size (≥17 mm in diameter), and cannot be inserted through a standard−sized laparoscopic port (5-15mm in diameter). Subsequent research in this chapter focused on developing a small−sized force sensing device that could replace the use of the commercial F/T sensors.

The work in chapters 3 has demonstrated the approach of Stiffness Image based on Sliding Indentation (SISI) is able to detect and locate the areas of high stiffness within soft tissue. This chapter describes a validation experiment with the second stiffness prototype for further evaluating the effectiveness of the SISI approach in detecting stiff nodules buried in soft tissue sample in comparison to manual palpation conducted by experienced surgeons. This comparative study has been approved by Biomedical Sciences, Dentistry, Medicine and Natural & Mathematical Sciences Research Ethics Subcommittee at King's College London (BDM/1011-107).

During the comparative study, the developed probe is driven across the surface of simulated soft tissue samples using a Mitsubishi RV-6SL 6-DOF robotic manipulator. Silicone phantom samples embedded with simulated tumours were used in

order to compare human palpation and SISI based on sliding indentation. In total, sixteen experienced urological surgeons from Guy's Hospital were involved in this study.The results show that the SISI technique outperforms manual palpation with regards to the maximum forces applied to the tissue 48.3% decrease on average and the detection accuracy when locating tumours average increase an average increase from 41.7% to 66.7%. The research shows that the proposed SISI technique is a suitable substitute for manual palpation and due to the small size of the sensor it can be employed during MIS to reach tissue surfaces that cannot be accessed by the human hand.

6.2 Design of a Second Generation Prototype

6.2.1 Requirements for the probe

The location of the force sensing element is also an important issue that influences the quality of the measurements. There are two locations where the sensing elements can be placed, Figure 6.1. As shown in Figure 6.1 (a), the force sensor can be placed on the upper end of the probe shaft. It may be outside the patient's body or inside the patient's body when applied in MIS. If it is placed outside the patient's body, there is not much constraint with respect to the size of the sensing element since there is no need to go through the insertion port. However, the force sensing device placed at this position is subjected to friction and reaction forces created at the instrument insertion port. Measuring forces at this location without any means of compensation is therefore not practical. On the other hand, if the force sensing device is placed on the shaft inside the patient's body, friction and reaction forces generated at the instrument insertion port do not affect the accuracy and sensitivity of the measurement. However, then the dimension of the sensing device should be limited to less than 15 mm in

diameter (regular size of the trocar used to introduce a laparoscopic port). As shown in Figure 6.1 (b), the force sensing device can be placed at the lower tip of the instrument shaft. Friction and other disturbance forces generated from any moving mechanisms do not affect the accuracy of measured indentation force.

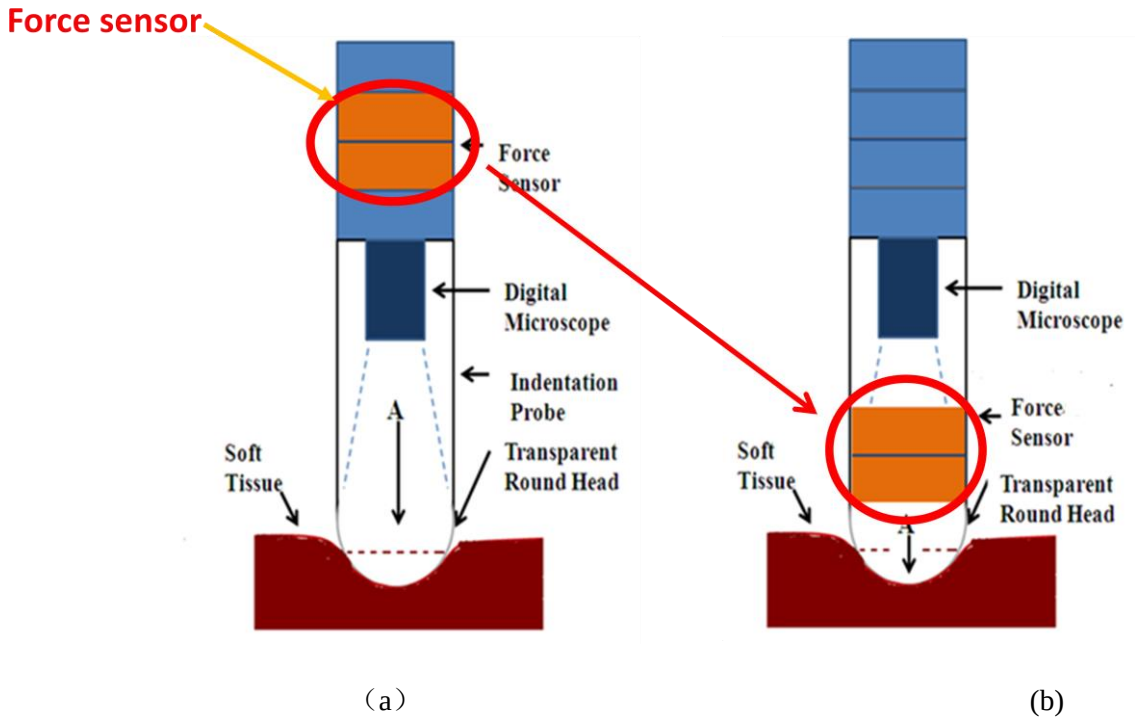

Figure 6.1: A conceptual image of the proposed stiffness probe indenting target soft tissue: (a) the force sensor is placed at the upper end of the instrument shaft. (b) The force sensing unit is placed at the lower tip of the instrument shaft.

However, with this arrangement, the force sensing device needs to be hollow or transparent, so that the digital microscope can capture the image of the contact area. In addition, the dimension of the sensing device should be limited to less than 15 mm in diameter as well. To the best of our knowledge, there has not been any commercially available force sensor which meets the above mentioned requirements.

6.2.2 Optic fibre based sensing

In recent years, photonic technologies have brought been widely used for sensor development in many applications. There are several types of optical fibre

sensors including intensity-modulated based, phase−modulated sensors, wavelength−modulated sensors. In this research, the intensity−modulated sensing scheme is selected for force sensor design since it usually require only a few sensing components and can made small and compact to meet miniaturisation requirement in MIS. Compared to other optical fibre sensors, it also has less temperature dependence. In addition, the sensing element of the sensor can be made of inexpensive plastic material.

A general form of the intensity modulation sensor employs a pair of straight parallel optical fibres, one transmitting fibre and one receiving fibre, and a reflector, Figure 6.2 Any changes of the distance between the reflective surface and the fibre tips cause the intensity of the light to the optical detector to be varied, allowing the relevant displacement related force to be measured.. Although such a sensing structure proved to be practical in many applications, a weak point of this structure is that most of the light is lost at the region between the fibre tips and the reflector. In order to overcome this problem, Puangmali et al. proposed a bent−tip optical fibres mechanism, where the pair of optical fibres has tips bent to a certain degree of fibre−tip angle, Figure 6.3(P. Puangmali 2008).

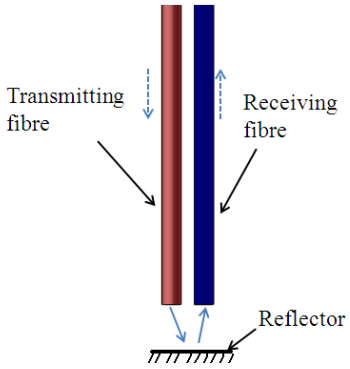

Figure 6.2: Intensity modulation mechanisms that utilise a straight parallel optical fibre

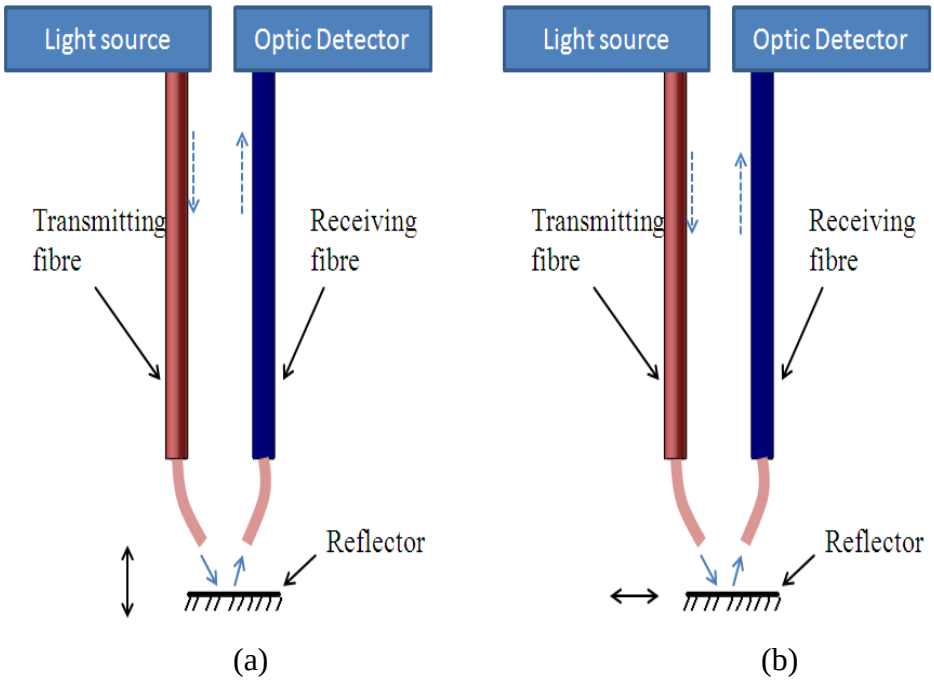

Figure 6.3: Intensity modulation mechanisms using a pair of bent−tip optical fibres. (a) The reflector can move laterally. (b) The reflector can move longitudinally(P. Puangmali 2008).

Based on this principle, there are two possible methods to modulate the light intensity: Sliding the reflector laterally while maintaining a constant distance between the fibre tips and the reflector surface, Figure 6.3 (a), and moving the reflector in the longitudinal direction with reference to the fibres, Figure 6.3 (b). The use of bent−tip optical fibres with either a laterally sliding or a longitudinally moving reflector offers much better sensitivity than straight fibres(P. Puangmali 2008).

In order to obtain good measurement sensitivity whilst maintaining high stiffness characteristics of the sensor, Puangmali et al. proposed a flexure made of a hollow cylindrical shaft which has a partial cut at a proximal end was employed with an internal straight long bar (P. Puangmali 2008), Figure 6.4. Such a long bar offers an

"amplifying effect" allowing a small deflection of the flexure to induce a large displacement at the position where the reflector is located.

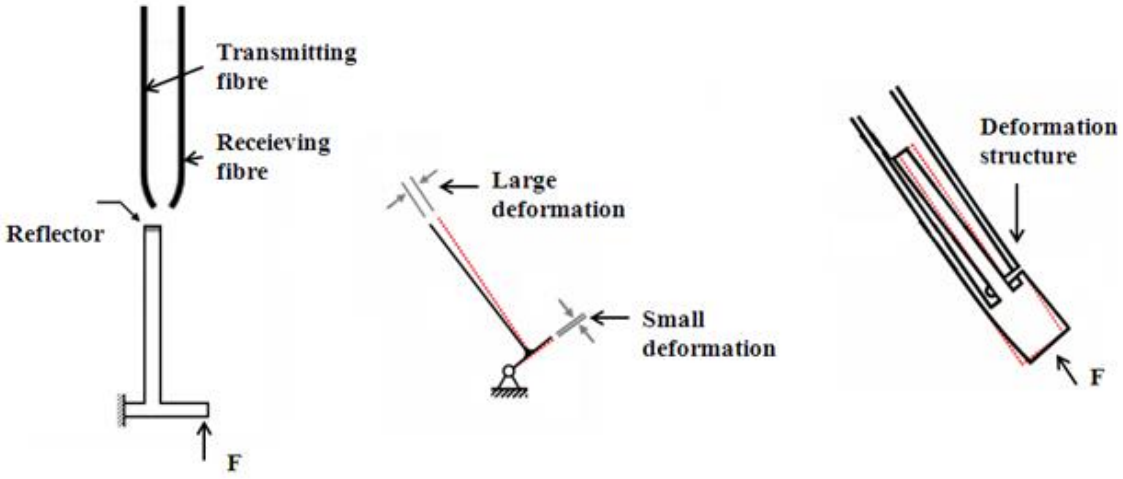

Fig 6.4: Working theory of the developed force sensor structure(P. Puangmali 2008).

Due to characteristics of the sensing structure in Figure 6.4, such a structure was adapted by the author to develop an unaxial force sensor as replacement of the Nano 17 force sensor on the first generation prototype of the stiffness probe, Figure 6.5.

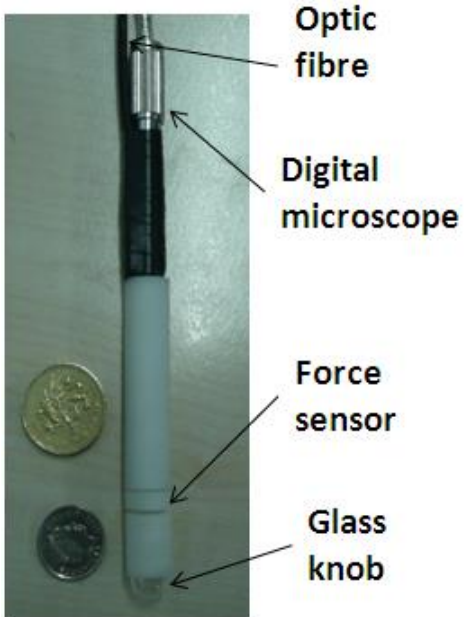

Figure 6.5: A second generation prototype of stiffness probe using optic fibre based force sensor.

6.2.3 The electrical circuit design for optic fibre sensor

The electrical circuit box for the optic fibre sensor includes optical source board, optical detection board, optical fibres, cables and a shielding box, Figure 6.6. In order to reduce the signal distortion from the electromagnetic field, the Optical Source Board and Optical Detection Board are both placed inside a box made of aluminium alloy. A 16-bit data acquisition card (NI PCI 6013) is used to acquire the measured signals. Optical source board is designed for generating the light for the optical fibre system. Five superlight LEDS are utilized to generate light, activated by a power supply circuit e using a 7805 terminal regulator. Five variable resisters (VR) are adapted for regulating the suitable light intensity.

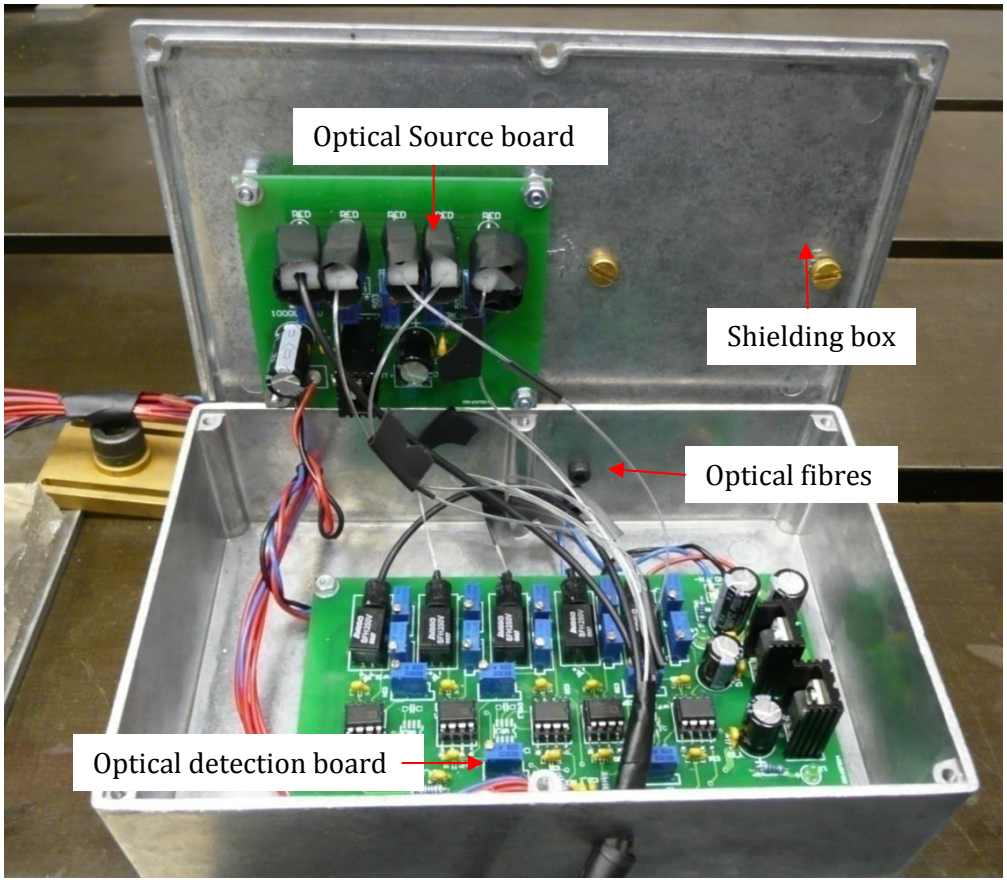

Figure 6.6: An electrical circuit box for optic fibre based force sensor.

Optical Detection Board is used to detect currents generated by the five photo detectors (SF250V). The power supply of +15v and -15v is generated from the 7815 and 7915 terminal regulators.

The currents generated by the photo detectors are transformed into voltage signal using voltage potential divider. Then the voltage signals are amplified with AD620 Op-amp. A low-pass RC filter is designed to eliminate the high frequency noise of AD620 output.

6.2.4 Calibration of the developed optic fibre sensor

To calibrate the force sensor of the stiffness probe, the probe is attached to the distal tip of a Mitsubishi RV-6SL, a 6-DoF (degree of freedom) robotic manipulator with a positioning accuracy up to 0.01 mm, to allow for accurate motion control. A 6-DOF ATI Nano17 Force/Torque sensor (calibration SI-25-0.25, resolution 0.003 N with 16-bit DAQ) was used as a standard force sensor. During the procedure of calibration, the probe press towards and retrieved from the Nano 17 sensor, varying the interaction force between the two sensors. The signals measured from the optic fibre sensor and the corresponding force values measured from the Nano 17 were recorded. The calibration results are shown in Figure 6.7.

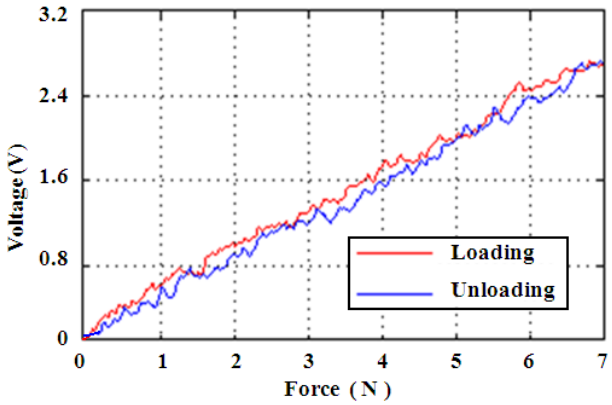

Figure 6.7: Calibration results of the force sensor prototype to loading/unloading.

6.3 Material and Method

6.3.1 Material

The materials used in these experiments were silicone phantom embedded with rubber nodules, Figure 6.8. These silicon phantoms were made from silicone gels (RTV6166 A and RTV6166 B, General Electric Spherical rubber nodules with a diameter of 5 mm and hemispherical ones with a diameter of 10 mm were used to simulate tumours.

The elastic modulus of the nodule is 252±20.6 KPa and that of the silicone phantom was measured as 19.8± 1.6 KPa. Nine phantoms with small nodules and nine phantoms large nodules were prepared for each trial. For both small nodules and large nodules, the buried depth is 2.5 mm. The number of nodules in each sample was allocated to be either zero or one or two, determined by a block randomization process. The human subjects were blinded to the process of randomization. The average length and width of these phantoms are 110±4.2mm×55±2.8mm. Furthermore, these silicone phantoms have an uneven surface and the average surface height is 29 ± 1.25mm.

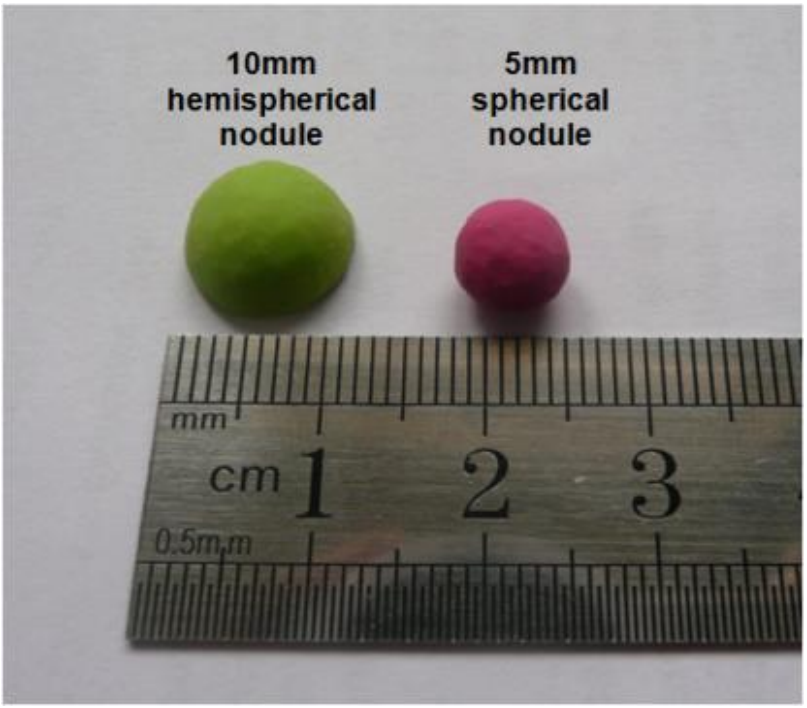

(a)

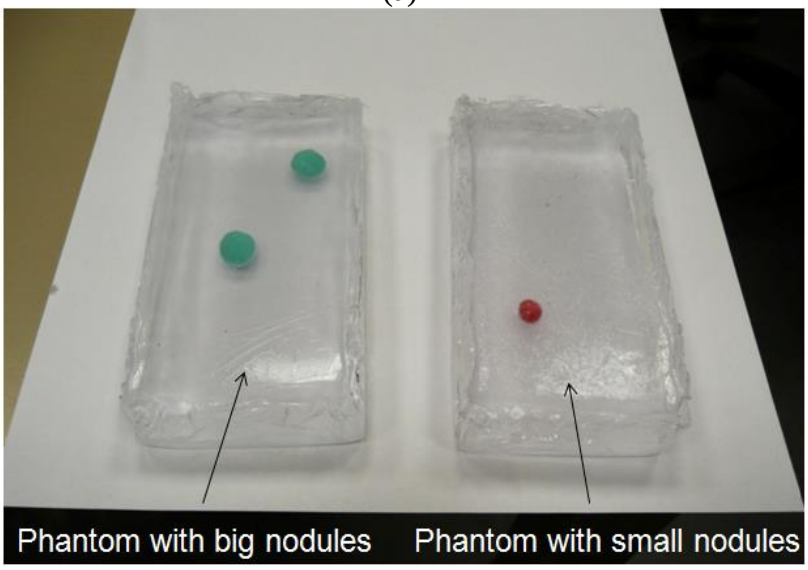

(b)

Figure 6.8: (a) Simulated tumours. (b) A phantom with two big nodules and a phantom with one small nodule.

The performance of SISI and manual palpation was evaluated with regards to: the success rate for tumour localization, the palpation force and the task completion time.

The *success rate* for tumour localization can be used to assess the ability of experimental method to correctly identify the tumours in each sample. *Four categories*(Davidson 2002*),* are used to calculate the success rate. 1) *a true positive* occurs describe the situation where a tumor is correctly identified; 2) *a false positive* is used to describe the situation when a tumour is believed to be detected but, in fact, none is present; 3) *a false negative* shows that a tumour is not predicted although one does exist; and 4) *a true negative* occurs when it is correctly identified that there are no tumours. These four categories can be used to determine performance measures such as: accuracy ((a+d)/(a+b+c+d)), sensitivity (a/(a+c)), specificity(d/(b+d)), negative predictive value(d/(c+d)) and positive predictive value (a/(a+b)).

Sensitivity and specificity are statistical measures of the performance of a binary classification test. Sensitivity measures the proportion of actual positives which are correctly identified as such (e.g. the percentage of sick people who are correctly identified as having the condition). Specificity measures the proportion of negatives which are correctly identified (e.g. the percentage of healthy people who are correctly identified as not having the condition). If a test has high sensitivity then a negative result would suggest the absence of disease. If a test has high specificity, a positive result from the test means a high probability of the presence of disease. A high negative predictive value for a given test means that when the test yields a negative result, it is most likely correct in its assessment. A small positive predictive value indicates that many of the positive results from this testing procedure are false positives. Thus it will be necessary to follow up any positive result with a more reliable test to obtain a more accurate assessment as to whether cancer is present (Altman DG 1994).

Table 6.1: Four categories used to calculate accuracy, sensitivity, specificity, negative predictive value and positive predictive value (M. Davidson 2002)

Tumour				
		Present	Absent	Totals
Diagnostic Test Result	Positive	True Positives a	False Positives b	a+b
	Negative	False Negatives c	True Negatives d	c+d
	Totals	a+c	b+d	a+b+c+d

The *palpation force* exerted while searching for a tumour is adopted as a measure of the potential damage to the tissue. For the manual palpation tests conducted by the human subjects, the maximum forces were determined using the ATI Mini 40 force/tactile sensor placed below the testing plate. For sliding indentation tests, the maximum forces were determined using the developed force sensor attached to the probe.

6.3.2 Experiments for Manual Palpation

Figure 6.9 (a) shows the experimental setup for manual palpation. The samples can be placed on the top plate made from Plexiglas. An ATI 6-DOF force/torque sensor (Mini40, ATI Industrial Automation) was mounted between two plates. The lower plate was fixed to a table by two grippers. NI DAQ systems were configured to acquire the measured signals.

Sixteen subjects were invited to participate in the palpation experiments: all of them had clinical experience. Before the trials, the participants were permitted to touch and feel and feel the simulated tumours and were informed that the number of tumours inside the organ sample could be zero, one or two. During the trials, the locations of the tumours found by the participants were marked with self-stick labels, Figure 6.9 (b).

6.3.3 Experiments for Sliding Indentation

The protocol utilized for sliding indentation experiments is listed below: First, a series of 9 trajectories parallel to the x-axis were defined, with a shift of 5 mm along the y-axis between each path. Each trajectory was 100 mm in length and an area of $100\times45mm^2$ is to be covered during the experiment. Second, In order to follow the linear elastic assumption of tissue, the manipulator was programmed to traverse the developed probe along the predefined trajectories with original indentation depth of 3mm. The traversing speed was kept constant at 5mm/second. During all experiments, the sample frequency of image acquisition is 20 frame /second. The force imparted by the sample was recorded during each traverse at a sampling rate of 100Hz. After completion of the experiments, the SISIs were generated from the acquired data. The MISI gives the stiffness distribution over the test area, red representing the highest stiffness value and blue the lowest. The assessment of the images was performed by sixteen volunteers who had no knowledge of the number of tumours present in each trial. A similar assessment of success rate was conducted using *four categories*.

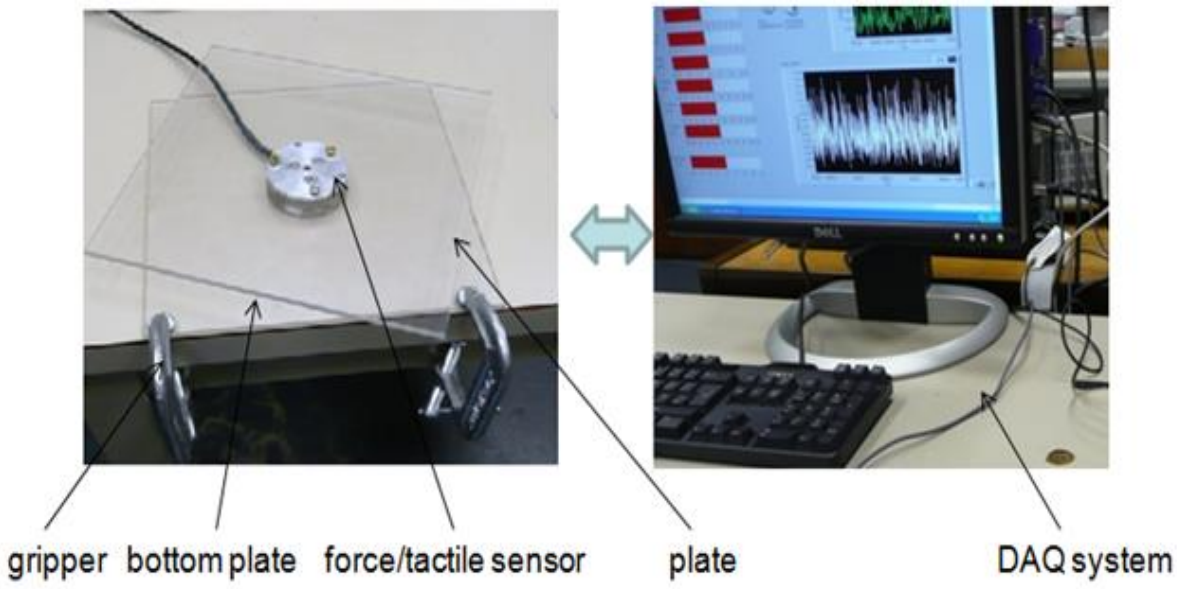

(a)

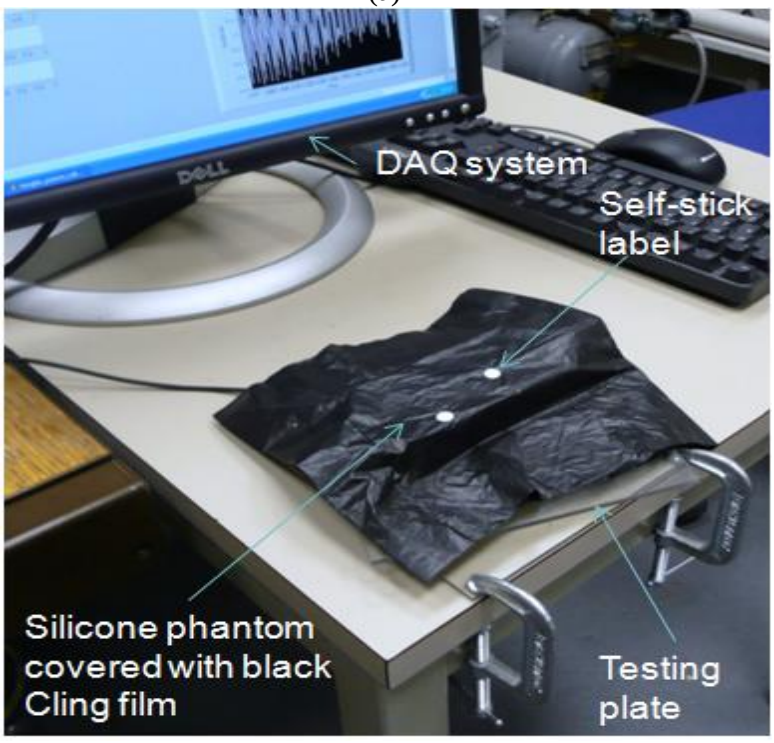

(b)

Figure 6.9: Layout of the experimental setup for manual palpation testing (a) and manual palpation experiments with phantom covered with black cling film. The suspected tumor sites were marked with self-stick labels (b).

The *t-test* assesses whether the means of two groups are *statistically* different from each other. The unpaired *t*-test is used when two independent and identically distributed samples are obtained, one from each of the two populations being compared. The paired *t-test* typically consists of a sample of matched pairs of similar units, or one group of units tested twice. In order to establish differences among the different methods, the paired *t-test* was used to determine differences between MISI and manual palpation. Then unpaired *t-test* was used to determine differences between the large and the small tumours within each group. The statistical analysis was conducted using the SPSS software, version 17.0 for windows.

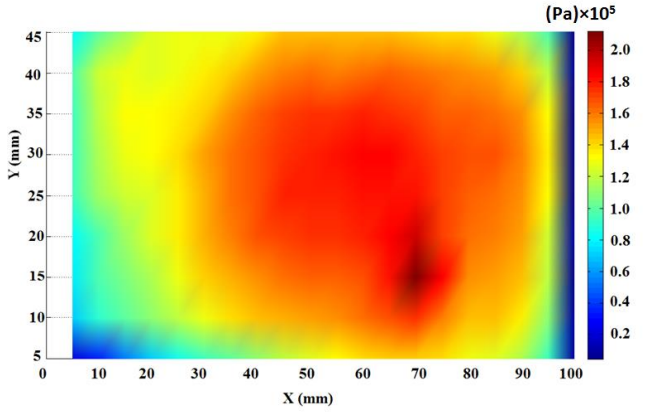

(a)

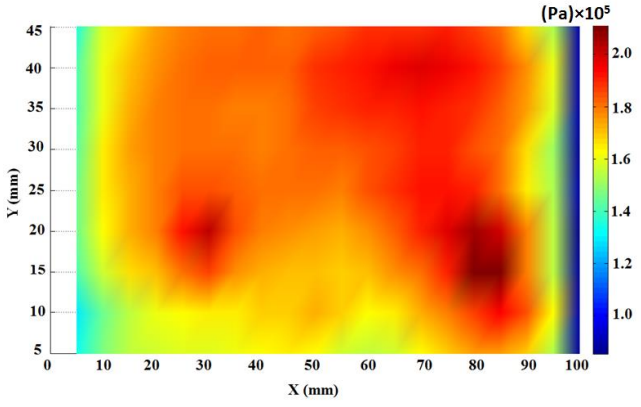

(b)

Figure 6.10: Selected stiffness image for the experiments: (a) one large nodule, (b) one small nodule and one large nodule.

6.4 Results

Figure 6.10 shows some of the selected stiffness images based on sliding indentation obtained from the experiments.

The experimental results are shown in Table 6.2 and Table 6.3. Table 6.2 shows the mean of the maximum forces applied on the silicones and the associated *p*-values. It is seen that there is a significant difference in the forces applied by the human in comparison to SISI. Table 6.3 shows the measures of accuracy. The results showed an improvement in all of the average of measures when using the SISI method. It is also found that both the manual palpation and the SISI approach performed better when trying to localize the 10 mm tumours than the 5 mm tumours. It should also be noted that the "large" tumours used in this study are not clinically large. Actually, the studies in (LeBlanc 2007; P. Singh 2007)show that conventional methods such as CT and MRI are not always capable of detecting tumours which are smaller than 10mm.

Table 6.2: Results for maximum force

Trial	**Maximum Force(N)**	**p-value**
A-Human		
Small tumors	5.26±1.6	0.770 small to large
Large tumors	5.04±1.2	
Average	5.15±1.4	P<0.001 A to B
B-Robot		
Small tumours	2.96±0.6	0.517 small to large
Large tumours	2.36±0.8	
Average	2.66±0.7	P<0.001 B to A

Table 6.3: Accuracy measures

Trial	Accuracy	Sensitivity	Specificity
A-Human			
Small tumours	41.7%	37.5%	50.0%
Large tumours	58.3%	55.6%	66.7%
Average	41.7%	46.6%	58.4%
B-Robot			
Small tumours	58.3%	57.1%	60.0%
Large tumours	75.0%	77.8%	66.7%
Average	66.7%	67.5%	63.4%

6.5 Discussion and Conclusions

This chapter presents a second generation prototype of the stiffness probe based on optic fibre force sensing techniques including sensing principle, design and manufacture, calibration and design of electrical circuits. The prototype was utilized to conduct a comparative study of SISI with manual palpation.

The experimental results show that SISI can result in an average 41.7% decrease in the maximum forces applied to the tissue and an average increase from 41.7% to 66.7% in the detection accuracy for tumours. It shows that the proposed SISI technique is a suitable substitute for manual palpation and due to the small size of the probe it has the potential to be employed during MIS to reach tissue surfaces that cannot be accessed by the human hand.

It should also be noted that the SISI setup employed in this paper is not suitable for use in a clinical environment since the robotic manipulator is an industrial robot and further evaluation study on animal organs and human organs need to be investigated in the future.

Chapter 7

Conclusions and Future Work

Chapter 7

7.1 Conclusions of the Thesis

This thesis proposes a smart, novel stiffness sensing probe using force and vision sensing to determine the stiffness of soft tissue organs to be used for many medical applications, especially for laparoscopic surgery or robot-assisted minimally invasive surgery (MIS) to compensate for the lack of "sense of touch" for surgeons. The performance of the developed probe was validated by tests of uniaxial tissue indentation and sliding tissue indentation on silicone phantoms and pork organs. A comparative study of the proposed probe with manual palpation was conducted. The results show that the probe can perform stiffness measurement effectively when the probe indents and slides on the tissue surface. Moreover, investigation of mechanical properties of archived human prostate tissues has been conducted using the developed stiffness sensing probe. As part of this research, inverse Finite Element Analysis (FEA) and generalised Newton-Raphson method are used for estimating the unknown mechanical properties of archived human prostate.

First, the work has contributed to the development of soft tissue diagnosis probe. The developed prototype integrates a force sensor with a transparent sphere mounted at one end of a shaft, which is connected to a miniature camera mounted at the other end. The digital microscope displays and records the contact area between the sphere and tissue. This information can be used to calculate the indentation depth. By combining depth and force measurements, the tissue stiffness can be mapped. Moreover, since the sphere is transparent, Surgeons can also use it to visually observe the tissue, doubling the probe's purpose as an endoscope. Optic-fiber sensing technique is used for force sensing in the updated design of the probe to replace the commercial force sensor. The main advantages of the developed probes are low-cost, simple structure and multi-functional. The stiffness image based on sliding indentation (SISI) approach for the

localisation of tissue abnormalities using the probe was presented and validated. The acquired force and stiffness information during sliding indentation can be converted into a pseudo-colour SISI, which can reveal the spatial variation of stiffness within the soft tissue. Then clinicians can localise abnormalities according to SISI, since abnormalities within the soft tissue are generally stiffer than the surrounding organ. The comparative study of SISI with manual palpation by experienced clinicians is also conducted. The experimental results demonstrate that the SISI approach is more effective than manual palpation in this phantom study, with moderately smaller forces applied to the phantom comparing to manual palpation.

Then, the research contributes a novel portable stiffness sensing platform for the three-dimensional scanning of soft tissue, capable of evaluating mechanical properties and geometry in ex-vivo condition. The platform comprises a passive robotic arm (Phantom Omni) with six degrees of freedom (DOF) position sensing, a data acquisition system, and a set of stiffness probes for force and stiffness measurement. Estimations of a total of 126 sites from 21 radical human prostate samples were analysed using the developed test rig. Each prostate was divided into 6 regions. The estimated stiffness from 6 regions was separated into normal and cancerous tissues according to the pathological information. A three-dimensional sliding indentation mechanical image was also generated using the test rig. Results from the ex-vivo tests demonstrate the capability to separate cancerous tissue from normal tissue based on stiffness and force measurement.

Finally, the work contributes to the estimation of the mechanical properties of archived human prostate using inverse Finite Element Analysis (IFEA) and Newton-Raphson method. The results imply that the proposed IFEA approach can estimate the mechanical properties of the archived human prostate effectively.

7.2 Future Work

7.2.1 Improvements of the stiffness probe

Firstly, the proposed probe has been tested on a range of biological and artificial tissue samples. In order to further optimize the design of the probe, different size of the transparent sphere head should be investigated. Moreover, in order to the accurately model the relation between the indentation depth and the tissue deformation during indentation, there are two other potential methods can be explored: modelling the pixels of contact area with the indentation depth and modelling the change of deformation volume with the indentation depth. Furthermore, the captured images for measurement of indentation depth are processed through commercial available software in an offline mode. In the future, an imaging processing system capable of providing with real-time measurement should be investigated. Finally, further validation tests for the designed probe could be conducted to distinguish the abnormal prostatic tissue from normal ones, aiding surgeons carrying out prostatectomy. In addition, the validation test could be extended to the *in vivo* experimental study in the future work.

7.2.2 Stiffness model of soft tissue

In this study, elastic modulus is used as the measurement of the tissue stiffness. However, this model may not work effectively for in vivo living biological soft tissues, since they are often inhomogeneous and nonlinear viscoelastic. Hence, estimation of unknown viscoelastic parameters including stiffness inversely based on the tissue force and deformation measurement has to be further investigated to allow the stiffness measurement more accurate.

Moreover, since the irregular boundary conditions of soft tissue will also distort the measured stiffness distribution. A mechanical image produced by the finite element modelling can be regarded as a reference image. The reference image would take into account of the shape and size of the investigated sample, the indentation depth and shape of the indenter. The comparison between the physically obtained stiffness image and the reference image is expected to be capable of providing more explicitly indication of the location of an abnormal stiff nodule within soft tissue.

7.2.3 Integration of the probe into MIS

In this study, the developed probe is driven by an industrial robot and a commercial available haptic device. In real surgical environments, there are two potential directions for the implementation of the developed stiffness probe into MIS: firstly, the probe can be integrated with a current surgical robot manipulator in which the indentation depth and trajectories of the probe are controllable. Alternatively, the probe can be developed into a hand-held laparoscopic device with a three dimensional tracking unit to track the trajectories.

7.2.4 Parameter Estimation of Prostate tissue using Inverse Finite Element Analysis

In this study, only one unknown tissue parameter, the shear modulus of the nonlinear hyperelastic Arruda-Boyce model, was estimated. However, the multi tissue parameters estimation could be further investigated by modifying the proposed method. Furthermore, the proposed tissue parameter estimation algorithm should be tested in real time *in vivo* experiments to study the effects of real tissue environments to the algorithm outputs.

Appendix

A.1: C++ Code for Data Acquisition of Force and Position Using the Phantom Omni Integrated Stiffness Probe

```
//*****************************************************************************/
//Comments: Defines the entry point for the console application.
#ifdef  _WIN64
#pragma warning (disable:4996)
#endif
#include <stdio.h>
#include <assert.h>
#include <vector>
#include <iostream>
#include <fstream>
#include <iomanip>
using namespace std;
#if defined(WIN32)
# include <windows.h>
# include <conio.h>
#else
# include "conio.h"
# include <unistd.h>
# define Sleep(x) usleep((x) * 1000)
#endif

#include <HD/hd.h>
#include <HDU/hduError.h>
#include <HDU/hduVector.h>//Comments: headfile for hapticdevice
#include "stdafx.h"
//#include <stdio.h>
#include <stdlib.h>
#include "ftconfig.h"//Comments: headfile for sensor
#include "nidaqex.h"//Comments: head file for ni card
HDCallbackCode HDCALLBACK UpdateCalibrationCallback(void *pUserData);
HDCallbackCode HDCALLBACK CalibrationStatusCallback(void *pUserData);
HDCallbackCode HDCALLBACK DevicePositionCallback(void *pUserData);
HDCallbackCode HDCALLBACK Device_joint_angles_Callback(void *pUserData);
HDCallbackCode HDCALLBACK Device_gimbal_angles_Callback(void *pUserData);
HDenum GetCalibrationStatus();
HDboolean CheckCalibration(HDenum calibrationStyle);
void PrintDevicePosition();
/*******************************************************************************
 Main function.
*******************************************************************************/
//Comments:Define Varibles for force and positions
struct PhantomOmniPosition
{
        double x;
        double y;
        double z;
} tempPos;
struct PhantomOmnijointAngle
{       double a;
        double b;
```

```
        double c;
} tempjoint_angle;
struct PhantomOmnigimbalAngle
{
        double d;
        double e;
        double f;
} tempgimbal_angle;///set for haptic
struct SensorForceRead
{
        double  fx;
        double  fy;
        double   fz;
} tempsensorForceRead;
struct SensorTorqueRead
{
        double  mx;
        double  my;
        double  mz;
} tempsensorTorqueRead;
std::vector<PhantomOmniPosition> vec_AllPos;
std::vector< PhantomOmnijointAngle> vec_All_Joint_angle;
std::vector< PhantomOmnigimbalAngle> vec_All_Gimbal_angle;
std::vector< SensorForceRead > vec_SensorForceRead;
std::vector< SensorTorqueRead > vec_SensorTorqueRead;

int main(int argc, char* argv[])
{
    HHD hHD;
    HDErrorInfo error;
    int supportedCalibrationStyles;
    int calibrationStyle; //Comments: for hap
//Comments: Variable for sensor
        char *calfilepath="C:/FT7486.cal";      // name of calibration file   // name of
calibration file
        unsigned short index=1;   // index of calibration in file (second parameter; default =
1)
        Calibration *cal;               // struct containing calibration information
        unsigned short i=0;       // loop variable used to print results
        short sts;              // return value from functions

        // Local Variable for card:
    i16 iStatus = 0;
    i16 iRetVal = 0;
    i16 iDevice = 1;
    i16 iChan = 0;
    i16 iGain = 1;
    f64  dVoltage = 0.0;
    i16 iIgnoreWarning = 0;
    int chan = 0;               /* change this to your channel */

float mvoltages[6]={0.2651,-0.0177,-0.0384,-0.0427,-0.1891,0.1373};

float FT[6];            // This array will hold the resultant force/torque vector

// create Calibration struct+

printf("Sensor calibration \n");
 //getch();
```

```
for(i=0;i< 6;++i)
{
    iStatus = AI_VRead(iDevice, i, iGain, &dVoltage);


        iRetVal = NIDAQErrorHandler(iStatus, "AI_VRead", iIgnoreWarning);


    if (iStatus == 0)
                {
                mvoltages[i]=(float)dVoltage;

                printf(" The voltage at Calibration AI channel %d is %f volts.\n",
i,mvoltages[i]);
                };
   }
        cal=createCalibration(calfilepath,index);
        SetForceUnits(cal,(char*) "N");
        SetTorqueUnits(cal,(char*) "N-m");
        Bias(cal,mvoltages);

printf("Bias reading:\n");
        for (i=0;i<6;i++)
                printf("%9.6f ",mvoltages[i]);
printf(" \n");
 //getchar();
        for (i = 0; i < 6; ++i)
        {
    iStatus = AI_VRead(iDevice, i, iGain, &dVoltage);


        iRetVal = NIDAQErrorHandler(iStatus, "AI_VRead", iIgnoreWarning);


    if (iStatus == 0)
                {
                mvoltages[i]=(float)dVoltage;

                //printf(" \n The voltage at AI channel %d is %f volts.\n", i,mvoltages[i]);
                };
        }
 //getchar();
ConvertToFT(cal,mvoltages,FT);
printf("\nSensor Calibration Result:\n");
        for (i=0;i<6;i++)
                printf("%9.6f ",FT[i]);
   printf(". \n");
   printf("Ready to start... \n");
        vec_AllPos.empty();
        vec_All_Joint_angle.empty();
        vec_All_Gimbal_angle.empty();
     vec_SensorForceRead.empty();
        vec_SensorTorqueRead.empty();
    hHD = hdInitDevice(HD_DEFAULT_DEVICE);
    if (HD_DEVICE_ERROR(error = hdGetError()))
    {
        hduPrintError(stderr, &error, "Failed to initialize haptic device");
        fprintf(stderr, "\nPress any key to quit.\n");
        getch();
```

```
        return -1;
    }
    printf("Haptic  Calibration\n");
    printf("Found %s.\n\n", hdGetString(HD_DEVICE_MODEL_TYPE));

    /* Choose a calibration style.  Some devices may support multiple types of
       calibration.  In that case, prefer auto calibration over inkwell
       calibration, and prefer inkwell calibration over reset encoders. */
    hdGetIntegerv(HD_CALIBRATION_STYLE, &supportedCalibrationStyles);
    if (supportedCalibrationStyles & HD_CALIBRATION_ENCODER_RESET)
    {
        calibrationStyle = HD_CALIBRATION_ENCODER_RESET;
    }
    if (supportedCalibrationStyles & HD_CALIBRATION_INKWELL)
    {
        calibrationStyle = HD_CALIBRATION_INKWELL;
    }
    if (supportedCalibrationStyles & HD_CALIBRATION_AUTO)
    {
        calibrationStyle = HD_CALIBRATION_AUTO;
    }
    /* Some haptic devices only support manual encoder calibration via a
       hardware reset. This requires that the endpoint be placed at a known
       physical location when the reset is commanded. For the PHANTOM haptic
       devices, this means positioning the device so that all links are
       orthogonal. Also, this reset is typically performed before the servoloop
       is running, and only technically needs to be performed once after each
       time the device is plugged in. */
    if (calibrationStyle == HD_CALIBRATION_ENCODER_RESET)
    {
        printf("Please prepare for manual calibration by\n");
        printf("placing the device at its reset position.\n\n");
        printf("Press any key to continue...\n");

        getch();

        hdUpdateCalibration(calibrationStyle);
        if (hdCheckCalibration() == HD_CALIBRATION_OK)
        {
            printf("Calibration complete.\n\n");
        }
        if (HD_DEVICE_ERROR(error = hdGetError()))
        {
            hduPrintError(stderr, &error, "Reset encoders reset failed.");
            return -1;
        }
    }
    hdStartScheduler();
    if (HD_DEVICE_ERROR(error = hdGetError()))
    {
        hduPrintError(stderr, &error, "Failed to start the scheduler");
        return -1;
    }
    /* Some haptic devices are calibrated when the gimbal is placed into
       the device inkwell and updateCalibration is called.  This form of
       calibration is always performed after the servoloop has started
       running. */
    if (calibrationStyle  == HD_CALIBRATION_INKWELL)
    {
```

```
        if (GetCalibrationStatus() == HD_CALIBRATION_NEEDS_MANUAL_INPUT)
        {
            printf("Please place the device into the inkwell ");
            printf("for calibration.\n\n");
        }
    }
            printf("Press any key to quit.\n\n");

        int intFreq;
        cout << "Please enter the frequency of sampling:";
        cin >>  intFreq;

        if (intFreq < 1 && intFreq > 2000)
        {
                cout << "Please check the frequency" << endl;
                return 0;
        }

        cout << endl;

   /* Loop until key press. */
    while (!_kbhit())
    {
        /* Regular calibration should be checked periodically while the
           servoloop is running. In some cases, like the PHANTOM Desktop,
           calibration can be continually refined as the device is moved
           throughout its workspace.  For other devices that require inkwell
           reset, such as the PHANToM Omni, calibration is successfully
           performed whenever the device is put into the inkwell. */
        if (CheckCalibration(calibrationStyle))
        {
                                for (i = 0; i < 6; ++i)
                                        {
                                                iStatus = AI_VRead(iDevice, i, iGain,
&dVoltage);


                                                iRetVal = NIDAQErrorHandler(iStatus,
"AI_VRead", iIgnoreWarning);


                                        if (iStatus == 0)
                                                {
                                                        mvoltages[i]=(float)dVoltage;

printf(" The voltage at AI channel %d is %f volts.\n", i,mvoltages[i]);
                                        };

                                        }
                                                printf(".\n");

                                        ConvertToFT(cal,mvoltages,FT);

                                        printf("\n sensor  Result:\n");
                                        for (unsigned short jj=0; jj<6; jj++)
                                        {printf("%9.6f",FT[jj]);}
                                       tempsensorForceRead.fx=FT[0];
                                        tempsensorForceRead.fy=FT[1];
                                        tempsensorForceRead.fz=FT[2];
```

```
                                        tempsensorTorqueRead.mx=FT[3];
                                        tempsensorTorqueRead.my=FT[4];
                                        tempsensorTorqueRead.mz=FT[5];

                                        vec_SensorForceRead.push_back(tempsensorForceRead);
                        vec_SensorTorqueRead.push_back(tempsensorTorqueRead);
                                        printf("\n read position\n");
                                        //getchar();
                                    PrintDevicePosition();
        }
        Sleep(intFreq);
    }
        std::fstream file_op("d:/1marA/test_mar_01-3m005MM_001.txt",std::ios::out);
        if(!file_op)
        {
                std::cout << "Fail to open the file. Please create a data.txt file!";
                vec_AllPos.empty();
                vec_All_Joint_angle.empty();
                vec_All_Gimbal_angle.empty();

                vec_SensorForceRead.empty();
        vec_SensorTorqueRead.empty();

            destroyCalibration(cal);
                return 0;
        }

        for (int i = 0; i < vec_AllPos.size(); ++i)
        {
                file_op <<setiosflags(ios::fixed)<<setprecision(6)<< vec_AllPos[i].x <<" "<<
vec_AllPos[i].y <<" "<<  vec_AllPos[i].z
                        <<" "<< vec_All_Joint_angle[i].a<<" "<< vec_All_Joint_angle[i].b<<"
"<<vec_All_Joint_angle[i].c
                        <<" "<< vec_All_Gimbal_angle[i].d<<" "<< vec_All_Gimbal_angle[i].e<<"
"<< vec_All_Gimbal_angle[i].f
                        <<" "<< vec_SensorForceRead[i].fx<<" "<< vec_SensorForceRead[i].fy<<"
"<< vec_SensorForceRead[i].fz
                        <<" "<< vec_SensorTorqueRead[i].mx<<" "<<
vec_SensorTorqueRead[i].my<<" "<< vec_SensorTorqueRead[i].mz
                        << std::endl;

        }
    file_op.close();
        hdStopScheduler();
    hdDisableDevice(hHD);
        vec_AllPos.empty();
        vec_All_Joint_angle.empty();
        vec_All_Gimbal_angle.empty();
        vec_SensorForceRead.empty();
        vec_SensorTorqueRead.empty();
        destroyCalibration(cal);
        return 0;
}/*******************************************************************************
 Begin Scheduler callbacks
//HDCallbackCode HDCALLBACK UpdateCalibrationCallback(void *pUserData)
HDCallbackCode HDCALLBACK UpdateCalibrationCallback(void *pUserData)
{
    //HDenum *calibrationStyle = (int *) pUserData;
        HDenum *calibrationStyle = static_cast<HDenum *> (pUserData);
```

```
            if (hdCheckCalibration() == HD_CALIBRATION_NEEDS_UPDATE)
    {        hdUpdateCalibration(*calibrationStyle);
    }
    return HD_CALLBACK_DONE;
}
HDCallbackCode HDCALLBACK CalibrationStatusCallback(void *pUserData)
{
    HDenum *pStatus = (HDenum *) pUserData;

    hdBeginFrame(hdGetCurrentDevice());
    *pStatus = hdCheckCalibration();
    hdEndFrame(hdGetCurrentDevice());
    return HD_CALLBACK_DONE;
```

A.2: Specification of Phantom Omni

Specifications for the
PHANTOM Omni® haptic device

The SensAble Technologies PHANTOM® product line of haptic devices makes it possible for users to touch and manipulate virtual objects. Different PHANTOM devices meet varying needs. The Premium models are high-precision instruments and, within the PHANTOM product line, provide the largest workspaces and highest forces, and some offer 6DOF (6 degrees of freedom) output capabilities. The PHANTOM Omni model is the most cost-effective haptic device available today. Portable design, compact footprint, and IEEE-1394a FireWire® port interface ensure quick installation and ease-of-use.

Model	The PHANTOM Omni Device
Force feedback workspace	~6.4 W x 4.8 H x 2.8 D in > 160 W x 120 H x 70 D mm
Footprint Physical area the base of device occupies on the desk	6 5/8 W x 8 D in ~168 W x 203 D mm
Weight (device only)	3 lb 15 oz
Range of motion	Hand movement pivoting at wrist
Nominal position resolution	> 450 dpi ~ 0.055 mm
Backdrive friction	<1 oz (0.26 N)
Maximum exertable force at nominal (orthogonal arms) position	0.75 lbf. (3.3 N)
Continuous exertable force (24 hrs.)	> 0.2 lbf. (0.88 N)
Stiffness	X axis > 7.3 lb/in (1.26 N/mm) Y axis > 13.4 lb/in (2.31 N/mm) Z axis > 5.9 lb/in (1.02 N/mm)
Inertia (apparent mass at tip)	~0.101 lbm. (45 g)
Force feedback	x, y, z
Position sensing **[Stylus gimbal]**	x, y, z (digital encoders) [Pitch, roll, yaw (± 5% linearity potentiometers)]
Interface	IEEE-1394 FireWire® port: 6-pin to 6-pin*
Supported platforms	Intel or AMD-based PCs
OpenHaptics® SDK compatibility	Yes

*Please visit the Support and Resources section of our website for more information www.sensable.com/support-overview.htm.

Corporate Headquarters
SensAble Technologies, Inc.
15 Constitution Way
Woburn, MA 01801 USA
[t] +1-781-937-8315
[f] +1-781-937-8325
email: info@sensable.com
Web: www.sensable.com

A.3: Mechanical Specification of Nano 17 and Mini 40 Sensor

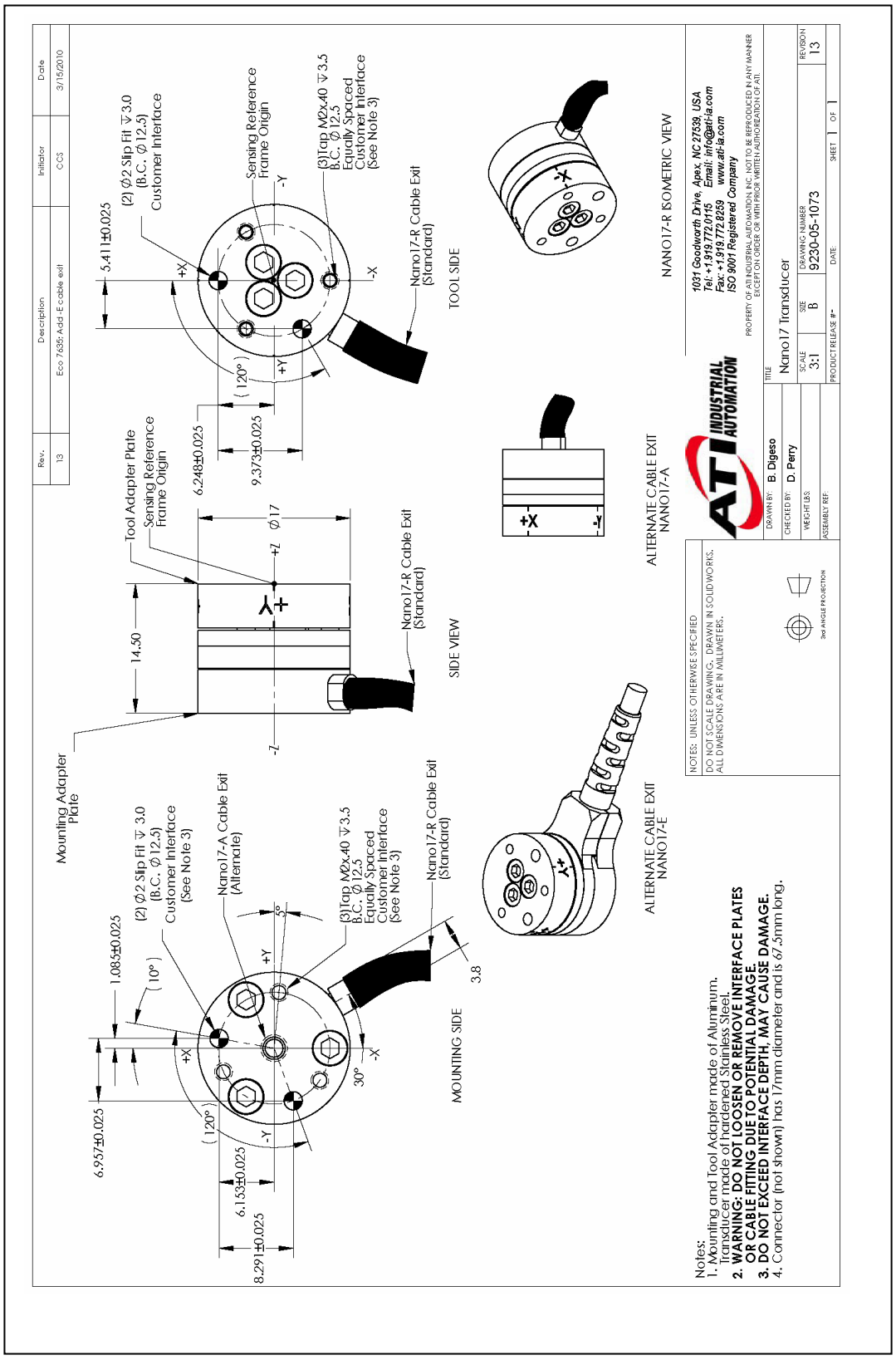

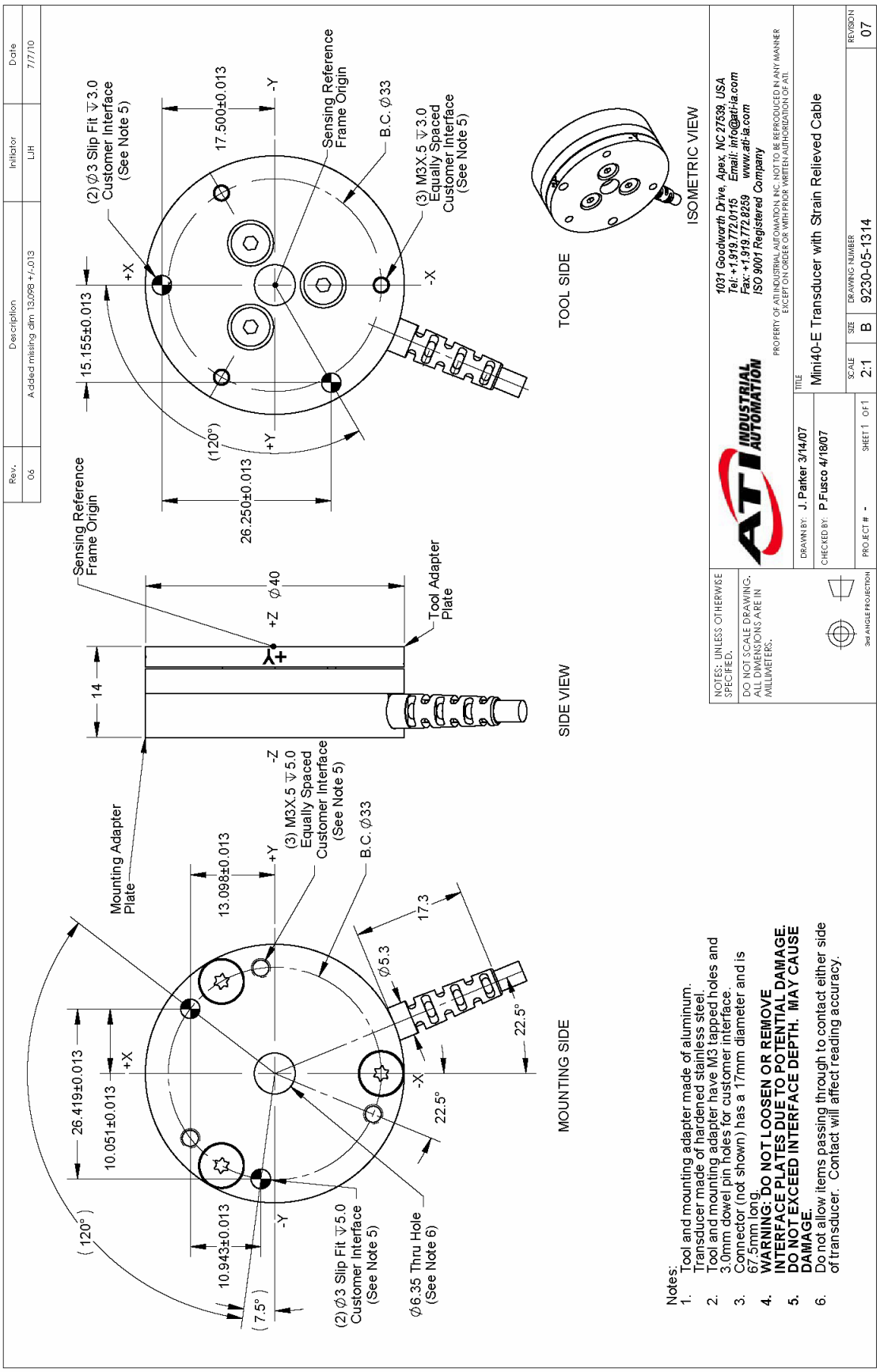
Rev.
06
Description
Added missing dim 13.098 +/-.013
Initiator
LJH
Date
7/7/10
(2) Ø3 Slip Fit ∓3.0
Customer Interface
(See Note 5)
17.500±0.013
Sensing Reference
Frame Origin
B.C. Ø33
(3) M3X.5 ∓3.0
Equally Spaced
Customer Interface
(See Note 5)
15.155±0.013
(120°)
26.250±0.013
Sensing Reference
Frame Origin
Ø40
14
Tool Adapter
Plate
Mounting Adapter
Plate
(3) M3X.5 ∓5.0
Equally Spaced
Customer Interface
(See Note 5)
13.098±0.013
B.C. Ø33
17.3
Ø5.3
22.5°
26.419±0.013
10.051±0.013
10.943±0.013
(7.5°)
(120°)
(2) Ø3 Slip Fit ∓5.0
Customer Interface
(See Note 5)
Ø6.35 Thru Hole
(See Note 6)
TOOL SIDE
SIDE VIEW
MOUNTING SIDE
ISOMETRIC VIEW
Notes:
1. Tool and mounting adapter made of aluminum.
2. Transducer made of hardened stainless steel.
3. Tool and mounting adapter have M3 tapped holes and 3.0mm dowel pin holes for customer interface.
4. Connector (not shown) has a 17mm diameter and is 67.5mm long.
4. WARNING: DO NOT LOOSEN OR REMOVE INTERFACE PLATES DUE TO POTENTIAL DAMAGE.
5. DO NOT EXCEED INTERFACE DEPTH. MAY CAUSE DAMAGE.
6. Do not allow items passing through to contact either side of transducer. Contact will affect reading accuracy.
NOTES: UNLESS OTHERWISE SPECIFIED.
DO NOT SCALE DRAWING. ALL DIMENSIONS ARE IN MILLIMETERS.
DRAWN BY: J. Parker 3/14/07
CHECKED BY: P.Fusco 4/18/07
3rd ANGLE PROJECTION
PROJECT # -
SHEET 1 OF 1
INDUSTRIAL AUTOMATION
1031 Goodworth Drive, Apex, NC 27539, USA
Tel: +1.919.772.0115 Email: info@ati-ia.com
Fax: +1.919.772.8259 www.ati-ia.com
ISO 9001 Registered Company
PROPERTY OF ATI INDUSTRIAL AUTOMATION, INC. NOT TO BE REPRODUCED IN ANY MANNER EXCEPT ON ORDER OR WITH PRIOR WRITTEN AUTHORIZATION OF ATI.
TITLE
Mini40-E Transducer with Strain Relieved Cable
SCALE 2:1
SIZE B
DRAWING NUMBER 9230-05-1314
REVISION 07

A.4: Measurement Specification of Nano 40 and Mini 17 Sensor

Metric Calibrations (SI) Mini40

Calibration	Fx,Fy	Fz	Tx,Ty	Tz	Fx,Fy	Fz	Tx,Ty	Tz
SI-20-1	20 N	60 N	1 Nm	1 Nm	1/200 N	1/100 N	1/8000 Nm	1/8000 Nm
SI-40-2	40 N	120 N	2 Nm	2 Nm	1/100 N	1/50 N	1/4000 Nm	1/4000 Nm
SI-80-4	80 N	240 N	4 Nm	4 Nm	1/50 N	1/25 N	1/2000 Nm	1/2000 Nm
	SENSING RANGES				RESOLUTION			

Metric Calibrations (SI) Nano17

Calibration	Fx,Fy	Fz	Tx,Ty	Tz	Fx,Fy	Fz	Tx,Ty	Tz
SI-12-0.12	12 N	17 N	120 Nmm	120 Nmm	1/320 N	1/320 N	1/64 Nmm	1/64 Nmm
SI-25-0.25	25 N	35 N	250 Nmm	250 Nmm	1/160 N	1/160 N	1/32 Nmm	1/32 Nmm
SI-50-0.5	50 N	70 N	500 Nmm	500 Nmm	1/80 N	1/80 N	1/16 Nmm	1/16 Nmm
	SENSING RANGES				RESOLUTION			

A.4: Schematic Diagram of Optic-fibre Sensor Interface Board

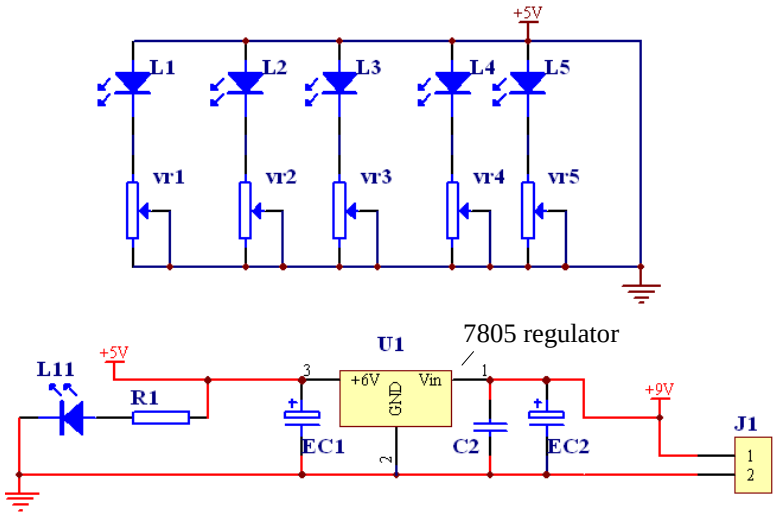

Schematic diagram of the light source circuit.

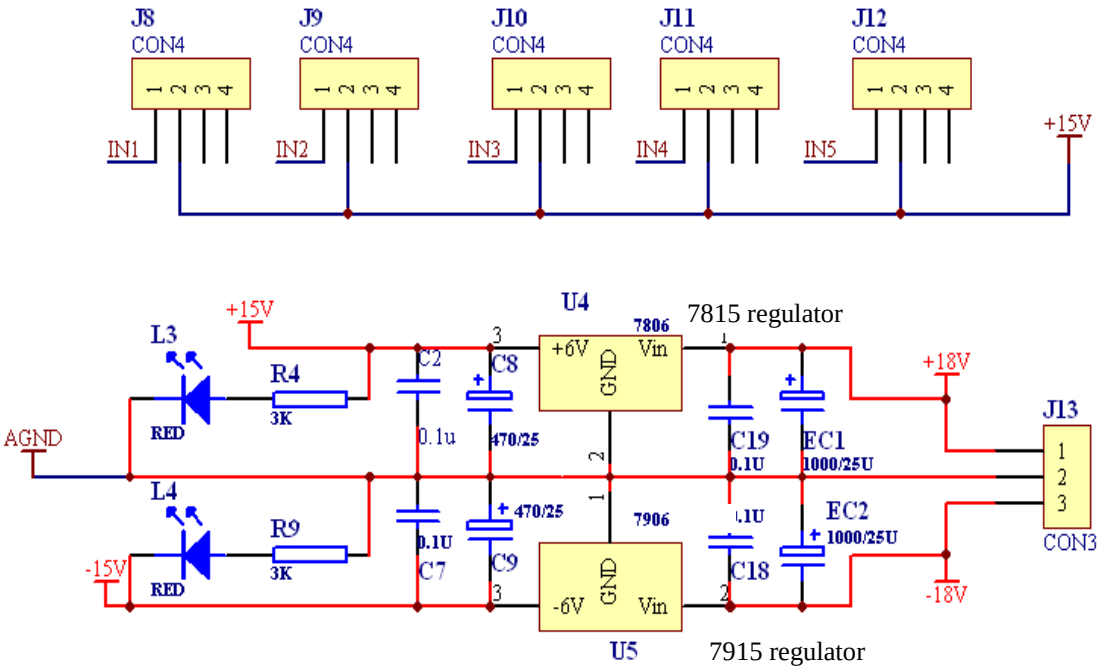

Schematic diagram of the power supply circuit for the optical detection board.

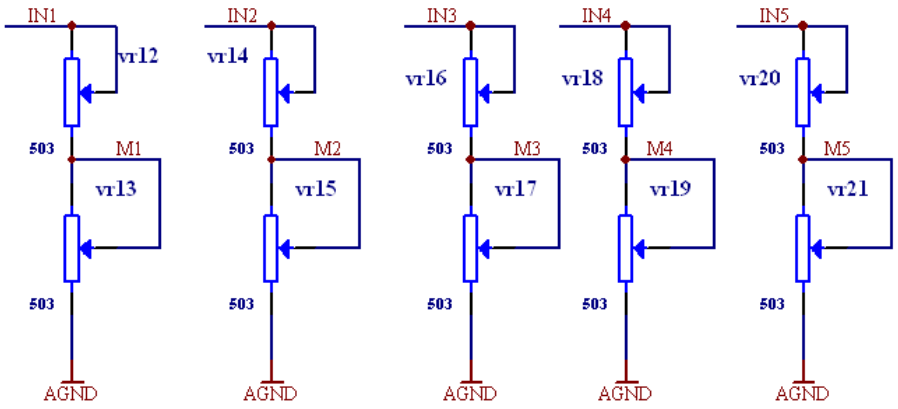

Schematic diagram of the potential dividers.

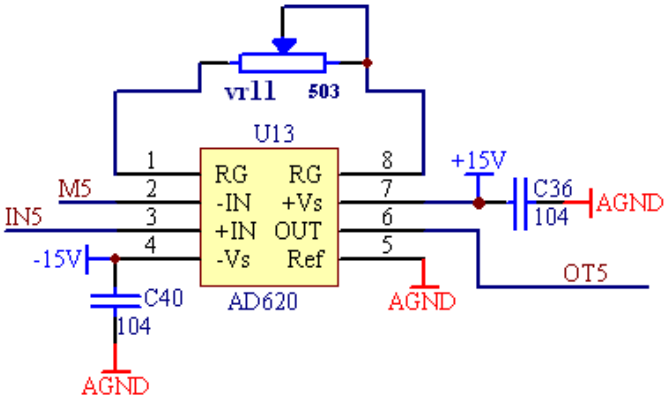

Schematic diagram of the AD620 Op-amp.

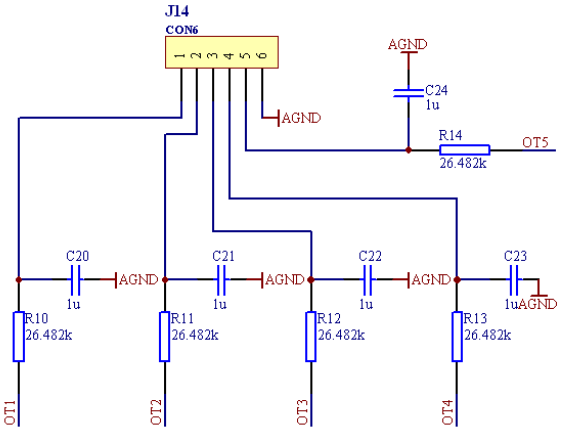

Schematic diagram of the RC low pass filter.

References

[1] ABAQUS, 2008, Abaqus Manaul version 6.8-1.
[2] Ahmadian, M. T., and Nikooyan, A. A., 2005, "Modeling and prediction of soft tissue directional stiffness using in vitro force-displacement data," International Journal of Scientific Research, 16.
[3] AmericanCancerSociety, 2011, Cancer Facts and Figures 2011., American Cancer Society, Atlanta, GA.
[4] Asiancancer.com, "http://www.asiancancer.com/cancer-diagnosis/throat-cancer-diagnosis/."
[5] Barnes, H. A., Hutton, J. F., and Walters, K., 1989, An Introduction to Rheology, Elsevier Science B.V.
[6] Beasley, R. A., and Howe, R. D., "Tactile tracking of arteries in robotic surgery," Proc. Proc. IEEE Int. Conf. Robot. Autom.
[7] Bergstrom, J. S., "Determination of Material Parameters for the 8-chain model for use with ABAQUS, LS-DYNA, and ANSYS."
[8] Bethea, B. T., Okamura, A. M., Kitagawa, M., Fitton, T. P., Cattaneo, S. M., Gott, V. L., Baumgartner, W. A., and Yuh, D. D., 2004, "Application of haptic feedback to robotic surgery," Journal of Laproendoscopic & Advanced Surgical Techniques, 14(3), pp. 191-195.
[9] Bicchi, A., Canepa, G., De Rossi, D., and al., e., "A sensor-based minimally invasive surgery tool for detecting tissue elastic properties," Proc. Proc. IEEE Int. Conf. Robot. Autom., pp. 884–888.
[10] Brouwer, I., and Ustin, J., "Measuring In-vivo Animal Sort Tissue Properties for haptic Modelling in Surgical Simulation," Proc. Medicine Meets Virtual Reality 2001, J. D. W. e. al., ed., IOS Press.
[11] Brown, J. D., 2003, "In-Vivo and In-Situ Compressive Properties of Porcine Abdominal Soft Tissues," Studies in Health Technology and Informatics - Medicine Meets Virtual Reality, 94, pp. 26-32.
[12] Brown, J. D., Rosen, J., and Kim, Y. S., "In vivo and in situ compressive properties of porcine abdominal soft tissues," Proc. Medicine Meets Virtual Reality II, pp. 26–32.
[13] Burman, M. Z., E. Joskowicz, L. Batkilin, E. Kunicher, Y. , 2003, "Bone-mounted miniature robot for surgical procedures: Concept and clinical applications," IEEE Trans on Robotics and Automation, 19(5), pp. 893-901.
[14] Caldwell, D. G., Tsagarakis, N., and Giesler, C., "An integrated tactile/shear feedback array for stimulation of finger mechanoreceptor," Proc. Proc. IEEE Int. Conf. Robot. Autom., pp. 287-292.
[15] Carra B.S., C. I., Ophir J. et al.,, 1997, "Elastography of breast lesions: initial clinical results," Radiology, 202, pp. 79-86.
[16] Carter, F. J., Frank, T. G., Davies, P. J., McLean, D., and Cuschieri, A., 2001, "Measurements and modeling of the compliance of human and porcine organs," Medical Image Analysis, 5(4), pp. 231-236.
[17] Choye P.L., 1995, "Imaging of prostate cancer," Abdominal Imaging, 20, pp. 505-515.

[18] Cotin C, D. H., Ayache N, 1999, "Real-time elastic deformations of soft tissues for surgery simulation," IEEE Trans Visualization and Computer Graphics, pp. 5(1):62–73.
[19] Culjat, M. O., King, C. H., Franco, M. L., Lewis, C. E., Bisley, J. W., Dutson, E. P., and Grundfest, W. S., "A tactile feedback system for robotic surgery," Proc. 30th Annual International IEEE EMBS Conference, pp. 1930 – 1934.
[20] Dargahi, J., Najarian, S., and Ramezanifard, R., 2007, "Graphical Display of Tactile Sensing Data with Application in Minimally Invasive Surgery," Canadian Journal of Electrical and Computer Engineering, 32(3), pp. 151-155.
[21] Dargahi, J., Parameswaran, M., and Payandeh, S. M., 2000, "A micromachined piezoelectric tactile sensor for an endoscopic grasper—Theory, fabrication and experiments," J. Microelectromech. Syst., 9(3), pp. 329-335.
[22] Dario, P., Hannaford, B., and Menciassi, A., 2003, "Smart Surgical Tools and Augmenting Devices," IEEE Transactions on Robotics and Automation, 19(5), pp. 782-792.
[23] Davies, B. L., 2000, "A Review of Robotics in Surgery," Proc Instn Mech Engrs, Part H, 214, pp. 129-140.
[24] Davies, B. L., Hibberd, R. D., Coptcoat, M. J., and al, e., 1989, "J Med Eng Technol," A surgeon robot prostatectomy--a laboratory evaluation, 13, pp. 273-277.
[25] Davis AM, D. S., Gerber L, Saunders M, Leung SF, O Sullivan B. , 2003, "Measuring postirradiation subcutaneous soft-tissue fibrosis: state-of-the-art and future directions," Semin. Radiat. Oncol, 13, pp. 203–213.
[26] Degani, A., Choset, H., Wolf, A., and Zenati, M. A., "Highly Articulated Robotic Probe for Minimally Invasive Surgery," Proc. Proc. IEEE Intl. Conf. Robot. and Automat., pp. 4167-4172.
[27] Deml, B., Ortmaier, T., and Seibold, U., "The touch, and feel in minimally invasive surgery," Proc. IEEE Int. workshop on haptic audio visual environment, and their applications, pp. 33-38.
[28] Dunn, D. C., 1994, "Digitally assisted laparoscopic surgery," Br. J. Surg., 81, p. 474.
[29] Egorov, V., Ayrapetyan, S., and Sarvazyan, A., 2006, "Prostate Mechanical Imaging: 3-D Image Composition and Feature Calculations," IEEE Trans. Med. Imag., 25(10), pp. 1329-1340.
[30] El Sayed, T., Mota, A., Fraternali, F., and Ortiz, M., 2008, "A variational constitutive model for soft biological tissues," Journal of Biomechanics, 41(7), pp. 1458-1466.
[31] Farshad, M., Barbezat, M., Flueler, P., Schmidlin, F., Graber, P., and Niederer, P., 1999, "Material Characterization of the Pig Kidney in Relation with the Biomechanical Analysis of Renal Trauma," Journal of Biomechanics 32, pp. 417-425.
[32] Forstner R, H. H., Occhipinti KA, Powell CB, Frankel SD, Stern JL, 1995, "Ovarian cancer: staging with CT and MR imaging," Radiology, pp. 197(193):619-126.
[33] Frasson, L., Parittotokkaporn, T., Schneider, A., Davies, B. L., Vincent, J. F. V., Huq, S. E., Degenaar, P., and Baena, F. M. R., "Biologically inspired microtexturing: Investigation into the surface topography of next-generation neurosurgical probes," Proc. 30th Annual International Conference of the IEEE Engineering in Medicine and Biology Society, pp. 5611 - 5614.
[34] Fuchs, K. H., 2002, "Minimially Invasive Surgery," Endoscopy, 34, pp. 154-159.
[35] Fukuda, T., Morita, H., Arai, F., Ishihara, H., and Matsuura, H., "Micro resonator using electromagnetic actuator for tactile display," Proc. Proceedings International Symposium on Micromechatronics and Human Science, pp. 143-148.

[36] Fung, Y. C., 1993, Biomechanics: Mechanical Properties of Living Tissues, Springer-Verlag, New York.
[37] Fung, Y. C., 1994, A First Course in Continuum Mechanics, Englewood Clifs, NJ: Prentice Hall.
[38] Garra BS, C. E., Ophir J, Spratt SR, Zuurbier RA, Magnant CM, Pennanen MF., 1997, "Elastography of breast lesions: initial clinical results," Radiology, 202, pp. 79–86.
[39] Gasser, T. C., Ogden, R.W., Holzapfel, G.A.,, 2006, "Hyperelastic modeling of arterial layers with distributed collagen fibre orientations," Journal of the Royal Society Interface, 3, pp. 15–35.
[40] Gaumard.com, "http://www.gaumard.com/breast-palpation-simulator-for-clinical-teaching-s230-4/."
[41] Glozman, D., and Shoham, M., 2007, "Image-guided Robot for Flexible Needle Steering," IEEE Transactions on Robotics, 23(3), pp. 459-467.
[42] Gou-Shiang Lin, S.-K. D. C., Wei-Cheng Yeh, Lin-Jie Cheng, "A feature based tumor detection for MRI breast imaging," Proc. The 23rd International Technical Conference onCircuits/Systems, Computer and Communication.
[43] Guthart, G. S., and Salisbury, J. K. J., "The IntuitiveTM telesurgery system: Overview and application," Proc. Proc. IEEE Int. Conf. Robotics and Automation, pp. 618-621.
[44] Han, L., Alison, J., and Burcher, M., 2003, "A novel ultrasound indentation system for measuring biomechanics properties of in vivo soft tissue," Ultrasound in Medicine and Biology, 29(6), pp. 813-823.
[45] Hannaford, B., Trujillo, J., and Sinanan, M., "Computerized endoscopic surgical grasper," Proc. Medicine Meets Virtual Reality, pp. 265–271.
[46] Hayes WC, H. G., Mockros LF, Keer LM, 1972, "A mathematical analysis for indentation tests of articular cartilage," J. Biomech, 5, pp. 541–551.
[47] Hayn, H., Schwarzmann, D, 2010, Haptically Enhanced Operational Concept for a Hydraulic Excavator, InTech Press.
[48] Hayward, V., and Cruz-Hernandez, M., "Tactile Display Device Using Distributed Lateral Skin Stretch " Proc. Proceedings Haptic Interfaces for Virtual Environment and Teleoperator Systems Symposium, pp. 1309–1314.
[49] Hirose, S., and Yoneda, K., "Development of optical 6-axial force sensor and its signal calibration considering non-linear interference," Proc. in Proc. IEEE Int. Conf. Robot. Autom., pp. 46-53.
[50] Huang, Y., Zheng, Y., and Leung, S., 2005, "Quasi-linear viscoelastic properties of fibrotic neck tissues obtained from ultrasound indentation tests in vivo," Clinical Biomechanics, 20, pp. 145–154.
[51] Huang YP, Z. Y., Leung SF. , 2005, "Quasilinear viscoelastic parameters of neck tissues with fibrosis
induced by radiotherapy. ," Clin. Biomech, 20, pp. 145–154.
[52] Humphrey, J. D., 2002, " Continuum Biomechanics of Soft Biological Tissues," Proc. R. Soc. Lond, A, pp. 1-43.
[53] I. Baumann, P. K. P., W. Kunert, and G. F. Buess, 2011, "Vibrotactile characteristics of different tissues in endoscopic otolaryngologic surgery – in vivo and ex vivo measurements," Minim. Invas. Ther. Allied Technol, 10(6), pp. 323–327.
[54] J. D. Brown, J. R., Y. S. Kim, L. Chang, M. N. Sinanan, and B. Hannaford, 2003, "In-vivo and in-situ compressive properties of porcine abdominal soft tissues," Proc. Medicine Meets Virtual Reality,, pp. 26-32.

[55] J. E. Bischoff, E. S., D. Sieber, M. Kersh, H. Ploeg, Mars Munchinger, "advance material modelling in a virtual biomechanical knee," Proc. abaqus users conference, pp. 1-15.
[56] J. Heemskerk, R. V. D., W. G. Van Gemert, G. L. Beets, J. W. M. Greve,M. J.H.M. Jacobs, and N. D. Bouvy, 2005, "First results after introduction of the four-armed da Vinci Surgical System in fully robotic laparoscopic cholecystectomy," Dig. Surg, 22(6), pp. 426-431.
[57] J. Kim, M. A. S., "Characterization of viscoelastic soft tissue properties from in vivo animal experiments and inverse FE parameter estimation," Proc. MICCAI 2005, pp. 599-606.
[58] J. S. Bergstrom, M. C. B., 1998, "Constitutive Modeling of the Large Strain Time-Dependent Behaviour of Elastomers," J. Mech. Phys.Solids., pp. Vol. 46, pp. 931-954.
[59] J. Shang, D. P. N., C. Payne, J. Clark, M.H. Sodergren, A. Darzi and G.-Z. Yang, 2011, "An Articulated Universal Joint Based Flexible Access Robot for Minimally Invasive Surgery," 2011 IEEE International Conference on Robotics and AutomationShanghai,China, pp. 1147-1152.
[60] Jain, A., Deguet, A., Iordachita, I., Chintalapani, G., Blevins, J., Le, Y., Armour, E., Burdette, C., Song, D., and Fichtinger, G., 2007, "Intra-operative 3D guidance in prostate brachytherapy using a non-isocentric C-arm.," Int Conf Med Image Comput Comput Assist Interv., 10(Pt 2), pp. 9-17.
[61] Jakopec, M., Rodriguez y Baena, F., Harris, S. J., Gomes, P., Cobb, J., and Davies, B. L., 2003, "The hands-on orthopaedic robot "acrobot": Early clinical trials of total knee replacement surgery," IEEE Transactions on Robotics and Automation, 19(5), pp. 902-911.
[62] Jean-Luc Gennisson, T. e. e. B., Micka¨el Tanter, Stefan Catheline, Mathias Fink, Laurent Sandrin, C´eline Cornillon, and Bernard Querleux, 2004, "Assessment of Elastic Parameters of Human Skin Using Dynamic Elastography," ieee transactions on ultrasonics, ferroelectrics, and frequency control,, 51(8), pp. 980-989.
[63] Jichun Li, H. L., Kaspar Althoefer and lakmal Seneviratne, 2012, "A Stiffness Probe Based on Force and Vision Sensing for Soft Tissue Diagnosis," 34th Annual International IEEE /EMBS Conference,EMBC 2012Sandiego,USA, pp. 944-947.
[64] Jichun Li, H. L., P Dasgupta, B Challacombe, L.D. Seneviratne and K Althoefer, 2012, "Clinical Study of Prostate Tumour Identification Using A Rolling Indenter Robot," 5th Hamlyn Symposium on Medical Robotics London,UK.
[65] Jichun Li, J. Z., Kaspar Althoefer and lakmal Seneviratne 2012, "A Passive Robotic Platform for 3D Mechnical Imaging of Soft tissue," IEEE/ASME International Conference on Reconfigurable Mechanisms and Robots, J. D. a. X. Kong, ed.Tianjin,China, pp. 477-485.
[66] Jinhua Shao, J. W., Yizhuo Zhang, Ligang Cui, Ke Liu, and Jing Bai, 2009, "Subtraction Elastography for the Evaluation of Ablation-induced Lesions: A Feasibility Study," ieee transactions on ultrasonics, ferroelectrics, and frequency control,, 56(1), pp. 44-54.
[67] Johnson, K. L., 1985, Contact Mechanics, Cambridge, London.
[68] Jung Kim, M. A. S., "Characterization of viscoelastic soft tissue properties from in vivo animal experiments and inverse FE parameter estimation," Proc. 8th Int'l Conf. on Medical Image Computingand Computer Assisted Intervention (MICCAI), Springer, pp. 599-606.
[69] K. Althoefer, H. L., P. Puangmali, D. Zbyszewski, D. Noonan, and L. D.Seneviratne., 2010, "Force sensing in medical robotics," Mechatronics in Action, D. B. a. D. W. Russell, ed., Springer-Verlag, London, pp. 157-162.

[70] K. Masamune, E. K., Y. Masutani, M. Suzuki, T. Dohi,H. Iseki, and K. Takakura, 1995, "Development of an MRI compatible needle insertion manipulator for stereotactic neurosurgery," J Image Guid Surg, 1(4), pp. 242-248.
[71] K. Sangpradit, a. L. S., 2010, "Tissue Parameter Estimation for a Mechatronic Probe Using Inverse Finite Element Analysis," The sixteenth annual conference on Mechatronics and Machine Vision in Practice, Brunei.
[72] K. Sangpradit, H. L., K. Althoefer, and L. Seneviratne, 2009, "Tissue Identification using Inverse Finite Element Analysis of Rolling Indentation," The 2009 IEEE International Conference on Robotics and Automation, ICRA 2009 Kobe, Japan, pp. 1250-1255.
[73] K. Sangpradit, H. L., P. Dasgupta, K. Althoefer, and L. Seneviratne 2011, "Finite-Element Modeling of Soft Tissue Rolling Indentation," IEEE Transactions on Biomedical Engineering, 58(12), pp. 3319-3327.
[74] Keller, K., and Ackerman, J., "Real-time Structured Light Depth Extraction," Proc. SPIE proceedings, pp. 11-18.
[75] Kerdok, A. E., "Identification of nonlinear constitutive law parameters of breast tissue," Proc. Proceeding of 2005 summer Bioengineering Conference.
[76] Kerdok, A. E., 2006, Characterizing the Nonlinear Mechanical Response of Liver to Surgical Manipulation, PhD thesis, Harvard University, Cambridge, MA.
[77] Kerdok, A. E., Jordan, P., Liu, Y., Wellman, P. S., Socrate, S., and Howe, R. D., "Identification of Nonlinear Constitutive Law Parameters of Breast Tissue," Proc. Proc. of the 2005 Summer Bioengineering Conference, ASME.
[78] Kerdok, A. E., Ottensmeyer, M. P., and Howe, R. D., 2005, "Effects of perfusion on the viscoelastic characteristics of liver," Journal of Biomechanics.
[79] Kevin Cleary, A. M., Vance Watson,Gernot Kronreif, and Dan Stoianovici., 2006, "Interventional robotic systems: applications and technology state-of-the-art.," Minim Invasive Ther Allied Technol., 15(2), pp. 101-113.
[80] Kim, J., Tay, B., Stylopoulos, N., Rattner, D. W., and Srinivasan, M. A., "Characterization of Intra-abdominal Tissues from In Vivo Animal Experiment for Surgical Simulation," Proc. MICCAI.
[81] Kitagawa, M., Dokko, D., Okamura, A. M., and Yuh, D. D., 2005, "Effect of sensory substitution on suture-manipulation forces for robotic surgical systems",," Journal of Thoracic and Cardiovascular Surgery, 129(1), pp. 151-158.
[82] Kontarinis, D. A., Son, J. S., Peine, W., and Howe, R. D., "A tactile shape sensing and display system for teleoperated manipulation," Proc. Proc. IEEE Int. Conf. Robot. Autom., pp. 641-646.
[83] Kwoh, Y. S., Hou, J., Jonckheere, E. A., and Hayati, S., 1988, " A robot with improved absolute positioning accuracy for CT guided stereotactic brain surgery.," IEEE Trans on Biomedical Engineering, 35(2), pp. 153-160.
[84] Lau J, L. W., Zheng YP. , 2005, "Application of tissue ultrasound palpation system (TUPS) in objective scar evaluation.," Burns, 31, pp. 445–452.
[85] Laurent Sandrin, M. e. T., Jean-Luc Gennisson, Stefan Catheline, and Mathias Fink, 2002, "Shear Elasticity Probe for Soft Tissues with 1-D Transient Elastography," ieee transactions on ultrasonics, ferroelectrics, and frequency control,, 49(4).
[86] Lavoie, P., Ionescu, D., and Petriu, E. M., 2004, "3D object model recovery from 2D images using structured light," IEEE Transactions on Instrumentation and Measurement, 53(2), pp. 437- 443.
[87] LeBlanc, J. K. e. a., 2007, "Endoscopic ultrosound: how does it aid the surgeon?," Advances in Surgery, 41, pp. 17-50.

[88] Lee, Y. S., and Wise, K. D., 1982, "A batch-fabricated silicon capacitive pressure transducer with low temperature sensitivity," IEEE Trans. Electron Devices, ED-29(1), pp. 42-48.
[89] Leung SF, Z. Y., Choi CYK, Mak SSS, Chiu SKW, Zee B, Mak AFT. , 2002, " Quantitative measurement of post-irradiation neck fibrosis based on the Young modulus—description of a new method and
clinical results.," Cancer, 95, pp. 656–662.
[90] Li J, H. L., P Dasgupta, B Challacombe, L.D. Seneviratne and K Althoefer, 2011, "Results of Kidney Lesion Experiments with Haptic Probe," the 59th annual meeting of Society of Academic & Research Urology, SARS 2011Dublin, Ireland.
[91] Liu, H., Noonan, D. P., Challacombe, B. J., Dasgupta, P., Seneviratne, L. D., Althoefer, K,, 2009, "Rolling Mechanical Imaging for Tissue Abnormality Localization During Minimally Invasive Surgery," IEEE Transations on Biomedical Engineering, pp. 57(52): 404-414.
[92] Liu H , K. A., L Seneviratne, "Rolling Mechanical Imaging: A Novel Approach for Soft Tissue Modelling and Identification during Minimally Invasive Surgery," Proc. IEEE International Conference on Robotics and Automation, (IRA).
[93] Liu H, P. P., D Zbyszewski, O Elhage, P Dasgupta, J S Dai, L Seneviratne, and K Althoefer, "An indentation depth–force sensing wheeled probe for abnormality identification during minimally invasive surgery," Proc. The Institution of Mechanical Engineering, Part H.
[94] Liu H. , D. N., K. Althoefer, L. Seneviratne, "The Rolling Approach for Soft Tissue Modelling and Mechanical Imaging during Robot-Assisted Minimally Invasive Surgery," Proc. IEEE International Conference on Robotics and Automation, (ICRA).
[95] Liu H., J. L., X. Song, L.Seneviratne, K. Althoefer 2011, "Rolling Indentation Probe for Tissue Abnormality Identification during Minimally Invasive Surgery," IEEE Transactions on Robotics, 27(3), pp. 450-460.
[96] Liu Hongbin , J. L., Qi-ian Poon, Lakmal Seneviratne and Kaspar Althoefer, 2010, "Miniaturized Force-Indentation Depth Sensor for Tissue Abnormality Identification during Laparoscopic Surgery," IEEE International Conference on Robotics and Automation Anchorage, AK, pp. 3654-3659.
[97] Liu, Y., "A nonlinear finite element model of soft tissue indentation " Proc. Proceedings of Medical Simulation, International Symposium - ISMS 2004
[98] Liu, Z., and Bilston, L., 2000, "On the Viscoelastic Character of Liver Tissue: Experiments and Modeling of the Linear Behavior," Biorheology, 37, pp. 191-201.
[99] Love, G. J., Pillai, A., and Gibson, S., 2008, "Use of the mini C-arm for wrist fractures--establishing a diagnostic reference level," Radiat Prot Dosimetry, 128(3), pp. 309-311.
[100] M. Bro-Nielsen, S. C., "Soft tissue modeling in surgerysimulation for prediction of results of craniofacial operations & steps toward virtual reality training systems," Proc. Proc. 3rd Int. Workshop Rapid Prototyping in Medicine & Computer-Assisted Surgery, p. 35.
[101] M. Bro-Nielsen, S. C., "Real-time volumetric deformable models for surgery simulation using finite elements and condensation," Proc. Computer Graphics Forum, pp. 57–66.
[102] M. J. Turner, R. W. C., H. C. Martin and L. J. Topp, 1956, "Stiffness and Deflection Analysis of Complex Structures," J. of Aero. Sci., p. 23 (29).
[103] M. Kaneko, K. T., and T. Kawahara, 2005, "Dynamic Sensing of Human Eye," IEEE Int. Conf. on Robotics and Automation (ICRA2005),, pp. 2882–2887.

[104] M. Kaneko, T. K., S. Matsunaga, and S. Tanaka 2004, "Non-contact stiffness imager," Proc. of the IEEE Int. Conf. on Robotics and Automation, pp. 1562–1567.
[105] M. Tada, N. N., T. Maeno, "Material properties estimation of layered soft tissue based on MR observation and iterative FE simulation," Proc. MICCAI, spriger-Verlag, pp. 633-640.
[106] M. Wolfram, R. B., T. Engl, W. Bentas, S. Heitkamp, M. Ostwald, W., and Kramer, J. B., R. Blaheta, D. Jonas, and W. −D. Beecken,, 2003, "Robotic-assisted laparoscopic radical prostatectomy: the Frankfurt technique," World J. Urol, 21(3), pp. 128-132.
[107] M. Zhang, Y. P. Z., and A. F. T. Mak,, 1997, "Estimating the effective Young's modulus of soft tissues from indentation tests — nonlinear finete element analysis of effects of friction and large deformation," Med. Eng. Phys, 19(6), pp. 512–517.
[108] M.Hossenini, J. D., S. Najarian, and S. Motaghinasab., 2006, "Detection of tumours using a computational tactile sensing approach," The International Journal of Medical Robotics and Comouter Assited Surgery, 2(4), pp. 333-340.
[109] M.P. Ottensmeyer, J. K. S. J., 2009, "In vivo data acquisition instrument for solid organ mechanical property measurement," Lecture Notes in Computer Science, 2208, pp. 975–982.
[110] Margulies, A. G. a. a. S. S., 2004, "Are in vivo and in situ brain tissues mechanically similar?," J. Biomech, 37, pp. 1339–1352.
[111] McKnight AL, K. J., Rossman PJ, Manduca A, Hartmann LC, Ehman RL. MR 2002, "elastography of breast cancer: preliminary results," Am. J. Roentgenol, 178, pp. 1411–1417.
[112] Miller, A., Allen, P., and Fowler, D., "In-Vivo Stereoscopic Imaging System with 5 Degrees-of-Freedom for Minimal Access Surgery," Proc. Medicine Meets Virtual Reality 12, pp. 234-240.
[113] Miller, A. P., Peine, W. J., Son, J. S., and al, e., "Tactile imaging system for localizing lung nodules during video-assisted thoracoscopic surgery," Proc. Proc. IEEE Int. Conf. Robot. Autom., pp. 2996–3001.
[114] Miller, K., Chinzei, K., Orssengo, G., Bednarz, P., 2000, " Mechanical properties of brain tissue in vivo: experiment and computer simulation," Journal of Biomechanics, 33(11), pp. 1369–1376.
[115] Miller, K., 2005, "Method of testing very soft biological tissues in compression," Journal of Biomechanics 38, pp. 153–158.
[116] Miller, K., and Chinzei, K., 1997, "Constitutive modelling of brain tissue: experiment and theory," Journal of Biomechanics, 30(11/12), pp. 1115– 1121.
[117] Miller, K., and Chinzei, K., 2002, "Mechanical properties of brain tissue in tensio," Journal of Biomechanics, 35(4), pp. 483–490.
[118] Min Li, H. L., Jichun Li, Lakmal D. Seneviratne and Kaspar Althoefer, 2012, "Tissue Stiffness Simulation and Abnormality Localization using Pseudo-Haptic Feedback," IEEE Int. Conf. Robotics and Automation,ICRA2012Minnesota, USA, pp. 5359-5364.
[119] Mooney, M., 1940, "A theory of large elastic deformation," J. Appl. Phys., 11, pp. 582-592.
[120] Moore, A. J., and Newell, D. W., 2005, Neurosurgery: principles and practice, Springer, Berlin.
[121] Morgan, F. R., 1960, "The mechanical properties of collagen fibres: Stress-strain curves," J. Soc. Leather Trades Chem., 44, pp. 171-182.

[122] Mourgues, F., Devernay, F., and Coste- Manière, E., "3D reconstruction of the operating field for image overlay in 3D-endoscopic surgery," Proc. Proceedings of International Symposium on Augmented Reality, pp. 191-192.
[123] Moy, G., Wagner, C., and Fearing, R. S., "A compliant tactile display for teletaction," Proc. Proc. IEEE Int. Conf. Robot. Autom., pp. 3409-3415.
[124] Mridha M, O. S., 1986, "Noninvasive method for the assessment of subcutaneous edema. ," Med. Biol. Eng.Comput
Comput Aided Surg, 24, pp. 393–398.
[125] Murphy, D. A., Miller, J. S., Langford, D. A., and Snyder, A. B., 2006, J. Thorac. Cardiovasc. Surg., 132(4), pp. 776-781.
[126] N. Tanaka, R. U., M. Higashimori, K. Tadakuma, M. Kaneko, 2008, "Point-Type Non-Contact Stiffness Sensing of Soft Tissue with Coupling Effect," 32th Annual Int. Conf. of the IEEE Eng. in Medicine and Biology Society (EMBC2010),, pp. 5764-5767.
[127] Nobuyuki Tanaka, M. H., Makoto Kaneko, and Imin Kao, 2011, "Noncontact Active Sensing for Viscoelastic Parameters of Tissue With Coupling Effect," IEEE Transactions on Biomedical Engineering, 58(3), pp. 510-520.
[128] Okamura, A., and Simone, C., "Modeling of needle insertion forces for robot-assisted percutaneous therapy," Proc. Proc IEEE Int. Conf. on Robotics and Automation, pp. 2085-2091.
[129] Okamura, A. M., 2004, "Methods for Haptic Feedback in Teleoperated Robot-Assisted Surgery," Industrial Robot, An International Journal, 31(6), pp. 499-508.
[130] Okamura, A. M., Simone, C., and O'Leary, M. D., 2004, "Force Modelling for Needle Insertion into Soft Tissue,"" IEEE Transactions on Biomedical Engineering, 51(10), pp. 1707-1716.
[131] P. Dario and D. De Rossi, 1985, "Tactile sensors and the gripping challenge," IEEE Spectr, 22(8), pp. 46-52.
[132] P. J. Berkelman, L. L. W., R. H. Taylor, and P. Jensen,, 2000, "A miniature instrument tip force sensor for robot/human cooperative microsurgical manipulation with enhanced force feedback," Proc. 3rd Int. Conf. Med.Image Comput. Comput. Assist. Interv, pp. 897-906.
[133] P. Peng, A. S. S., R. Rajamani, A.G. Erdman, , 2010, "Novel MEMS stiffness sensor for force and elasticity measurements " Sensors and Actuators, A158, pp. 10–17.
[134] P. Puangmali, H. L., K. Althoefer, and L. D. Seneviratne, "Optical Fiber Sensor for Soft Tissue Investigation during Minimally Invasive Surgery," Proc. IEEE Int. Conf. on Robotics and Automation, pp. 2934-2939.
[135] P. Puangmali, H. L., K. Althoefer, and L. D. Seneviratne, 2008, "Optical fiber sensor for soft tissue investigation during minimally invasive surgery," Proc. IEEE Int. Conf. Robot. AutomPasadena, CA, pp. 2934–2939.
[136] P. Puangmali, K. A., L.D. Seneviratene, D. Murphy, and P. Dasgupta, 2008, "State-of-the-Art in Force and Tactile Sensing for Minimally Invasive Surgery," IEEE Sensors Journal, 8(4).
[137] P. Singh, e. a., 2007, "EUS for detection of the hepatocellular carcinoma:results of a prospective study," Gastrointest Endosc, 66, pp. 265-273.
[138] Pardeep Kumar, J. L., Hongbin Liu, Ben Challacombe, Ashish Chandra, Lakmal Seneviratne, Kaspar Althoefer and Prokar Dasgupta, 2011, "Prostate Tumour Identification Using a Force-Sensitive Rolling Indentation Probe," the 26th annual meeting of Engineering and Urology,EUS2011Wachington DC, USA, pp. A45-A46.
[139] Phipps, S., and T.H.J. Yang, F. K. H., R.L. Reuben, S.A. Mcneill, 2005, "Measurement of Tissue MeChanical Characteristics to Distinguish between Benign and Malignant Prostatic Disease," Urology, 66, pp. 447–450.

[140] Phipps, S., Yang, T. H. J., Habib, F. K., Reuben, R. L., and Mcneill, S. A., 2005, "Measurement of Tissue MeChanical Characteristics to Distinguish between Benign and Malignant Prostatic Disease," Urology, 66, pp. 447–450.
[141] Pohlenz, P., Blessmann, M., Blake, F., Gbara, A., Schmelzle, R., and Heiland, M., 2008, "Major mandibular surgical procedures as an indication for intraoperative imaging," J Oral Maxillofac Surg, 66(2), pp. 324-329.
[142] Polygerinos, P. Z., D; Schaeffter, T; Razavi, R; Seneviratne, L; A1thoefer, K, 2010, "MRI-Compatible Fiber-Optic Force Sensors for Catheterisation Procedures," IEEE Sensors Journal, pp. 91-99.
[143] Prange, M. T., and Margulies, S. S., 2002, "Regional, directional, and age dependent properties of the brain undergoing large deformation," Journal of Biomechanical Engineering—Transactions of the ASME, 124, pp. 244–252.
[144] Qasaimeh, M. A., Sokhanvar, S., Dargahi, J., and Kahrizi, M., 2009, "PVDF-Based Microfabricated Tactile Sensor for Minimally Invasive Surgery," Journal of Microelectromechanical Systems, 18(1), pp. 195-207.
[145] R. D. Howe, W. J. P., D. A. Kontarinis, and J. S. Son, 1995, "Remote palpation technology," IEEE Eng. Med. Biol. Mag, 14, pp. 318–323.
[146] Rebello, K., 2004, "Applications of MEMS in surgery," Proc. IEEE, 92(1), pp. 43–55.
[147] Rentschler, M. E., Dumpert, J., Platt, S. R., Oleynikov, D., and Farritor, S. M., "Mobile In-Vivo Biopsy Robot," Proc. Proc. IEEE Int. Conf. Robotics and Automation, pp. 4155-4160.
[148] Ridge, M. D. a. W., V., 1964, "The description of skin stiffness," Biorheology, 2, pp. 67-74.
[149] Rivlin, R. S., 1947, "Torsion of a rubber cylinder," J. Appl. Phys., 18, pp. 444-449.
[150] Rodriguez y Baena, F., 2006, "Man and the machine," Computing & Control Engineering Journal, 17(5), pp. 28-31.
[151] Rubin, M. B., and Bodner, S. R., 2002, "A Three-Dimensional Nonlinear Model for Dissipative Response of Soft Tissue," International Journal of Solids and Structures, 39, pp. 5081-5099.
[152] S. Cotin, H. D., M. Bro-Nielsen, N. Ayache, J. M.Clement, V. Tassetti, and J. Marescaux, "Geometric and physical representations for a simulator of hepatic surgery," Proc. Medicine Meets Virtual Reality, pp. 139–151.
[153] S. K. Prasad, M. K., G. S. Fischer, J. Zand, M. A. Talamini, R. H. Taylor,and A. M. Okamura, 2003, "A modular 2-dof force−sensing instrument forlaparoscopic surgery," Proc. 6th Int. Conf. Medical Image Comput.
Computer-Assisted Intervention, pp. 279-286.
[154] S. Uranüs, H. M., P. Bergmann, St. Huber, G. Höbarth, J. Pfeifer, B. Rigler, K. −H. Tscheliessnigg, and H. −J. Mischinger,, 2002, "Early experience with telemanipulative abdominal and cardiac surgery with the ZeusTM robotic system," Euro. Surg., 34(3), pp. 190–193.
[155] Salle, D., Bidaud, P., and Morel, G., "Optimal Design of a High Dexterity Modular MIS Instrument for Coronary Artery Bypass Grafting," Proc. International Conference on Robotics and Automation, pp. 1276-1281.
[156] Sankaranarayanan, G., King, H., Ko, S., Lum, M.J.H., Friedman, D.C.W., Rosen, J., Hannaford, B, 2010, "Portable Surgery Master Station for Mobile Robotic Telesurgery," 1st International ICST Conference on Robot Communication and CoordinationAthens pp. 1-8.

[157] Schwartz, J.-M., Denninger, M., Rancourt, D., Moisan, C., and Laurendeau, D., 2005, "Modelling liver tissue properties using a non-linear visco-elastic model for surgery simulation," Medical Image Analysis, 9, pp. 103–112.
[158] Shoham, M., Burman, M., Zehavi, E., Joskowicz, L., Batkilin, E., and Kunicher, Y., 2003, "Bone-Mounted Miniature Robot for Surgical Procedures: Concept and Clinical Applications," IEEE Trans. on Robotics and Automation, 19(5), pp. 893-901.
[159] Simaan, N., Taylor, R., and Flint, P., "A Dexterous System for Laryngeal Surgery," Proc. Proc. IEEE Intl. Conf. Robot. and Automat., pp. 351-357.
[160] Sokhanvar, S., Packirisamy, M., and Dargahi, J., 2007, "A multifunctional PVDFbased tactile sensor for minimally invasive surgery," Smart Mater. Struct, 16(4), pp. 989–998.
[161] Stoianovici, D., Cleary, K., Patriciu, A., Mazilu, D., Stanimir, A., Craciunoiu, N., Watson, V., and Kavoussi, L., 2003, "AcuBot: a robot for radiological interventions," IEEE Transactions on Robotics and Automation, 19(5), pp. 927-930.
[162] Stoianovici, D., Song, D., Petrisor, D., Ursu, D., Mazilu, D., and Muntener, M., 2007, "MRI Stealth" Robot for Prostate Interventions," Minimally Invasive Therapy & Allied Technologies, 16, pp. 241-248.
[163] Stoyanov, D. V., 2005, "Recovering 3D Structure and Motion for Applications in Robotic Laparoscopic Surgery," PhD Thesis, Imperial College London.
[164] Sutherland, G., McBeth, P., and Louw, D., 2003, "NeuroArm: an MR compatible robot for microsurgery," International congress series, 1256, p. 504.
[165] Suzuki, K., Najafi, K., and Wise, K. D., 1990, "A 1024-element high-performance silicon tactile imager," IEEE Trans. Electron Devices, 37(8), pp. 1852–1860.
[166] Sylvain Jaume, M. F., Benoît Macq, Lennox Hoyte, Julia R. Fielding, Andreas Schreyer, Ron Kikinis, Simon K. Warfield, 2003, "Tumor Detection in the Bladder Wall with a Measurement of Abnormal Thickness in CT Scans," Transactions on Biomedical Engineering, pp. Vol. 50, No. 53, pp 383-390.
[167] Szewczyk, S. T. S., Wan Y. ; Shih, Wei-Heng 2006, "Palpationlike soft-material elastic modulus measurement using piezoelectric cantilevers," Review of Scientific Instruments, 77(4).
[168] T A Krouskop, T. M. W., F Kallel, B S Garra,T Hall, 1998, "Elastic Moduli of Breast and Prostate Tissues Under Compression," Ultrasonic Imaging 20, pp. 260-274.
[169] T. Kawahara, S. T., and M. Kaneko, 2006, "Non-Contact Stiffness Imager," The Int. J. of Robotics Research, 25(6), pp. 537–549.
[170] T. Kawahara, Y. M., K. Akayama, M. Okajima, and M.Kaneko, 2010, "Design of Noncontact Tumor Imager for Video-Assisted Thoracic Surgery," IEEE/ASME Transactions on Mechatronics, 5(6), pp. 838-846.
[171] T. Lyyra, I. K., U. Vaatainen, H.J. Helminen, J.S. Jurvelin, X, Journal of Biomedical Material Research 48 pp.482–487, 1999., 1999, "In vivo characterization of indentation stiffness of articular cartilage in the normal human knee " Journal of Biomedical Material Research, 48, pp. 482–487.
[172] Tabaie, H. A., Reinbolt, J. A., Graper, W. P., Kelly, T. F., and Connor, M. A., 1999, "Endoscopic coronary artery bypass graft (ECABG) procedure with robotic assistance," The Heart Surgery Forum, 2(4), pp. 310-317.
[173] Tamura, A., Omori, K., Miki, K., Lee, J. B., Yang, K. H., and King, A. I., "Mechanical Characterization of Porcine Abdominal Organs," Proc. 46th Stapp Car Crash Conference, pp. 55–69.

[174] Taylor, R. H., and Stoianovici, D., 2003, "Medical Robotics in Computer-Integrated Surgery," IEEE Transactions on Robotics and Automation, 19(5), pp. 765-781.
[175] Tendick, F., and Cavusoglu, M. C., "Human Machine Interfaces for Minimally Invasive Surgery," Proc. Proc. 19th Intl. Conference IEEE/EMBS, pp. 2771-2776.
[176] Tillier, Y., 2004, "Finite element modeling for soft tissue surgery base on nonlinear elasticity behaviour," International Congress Series 1268, pp. 384-389.
[177] Tönuk E, S.-T. B., 2003, "Nonlinear elastic material property estimation of lower extremity residual limb tissue," IEEE Trans Neural Systems and Rehabilitation Engineering, pp. 11(11):43–53.
[178] Tsagarakis, N. G., Gray, J. O., Caldwell, D. G., Zannoni, C., Petrone, M., Testi, D., and Viceconti, M., 2006, "A haptic-enabled multimodal interface for the planning of hip arthroplasty," IEEE Multimedia, 13(3), pp. 40-48.
[179] V. Vuskovic, M. K., G. Szekely, M. Reidy, "Realitic force feedback for virtual reality based dianostic surgery simulation," Proc. IEEE Int. Conf. on Robotics and Automation, pp. 1592-1598.
[180] V.Vuskovic, M. K., G. Szekely, and M. Reidy, "Realistic force feedback for virtual reality based diagnostic surgery simulators," Proc. Proc. IEEE Int. Conf. Robotics and Automation, pp. 1592-1598.
[181] Vuskovic, V., Kauer, M., Szekely, G., and Reidy, M., "Realistic force feedback for virtual reality based diagnostic surgery simulators," Proc. Proc. IEEE Int. Conf. Robotics and Automation, pp. 1592-1598.
[182] W Wei, K. K., N Simaan, "A Compact Two-Armed Slave Manipulator for Minimally Invasive Surgery of the Throat," Proc. The first IEEE/RAS-EMB International Conference on Biomedical Robotics and Biomechatronics (BIOROB'2006), pp. 287-292.
[183] W.M. Vannah, D. M. D., J.A. Hastings, J.A. Stand, D.M. Harning, 1999, "A method
of residual limb stiffness distribution measurement," Journal of Rehabilitation Research and Development 36, pp. 1-7.
[184] Wagner, C., Stylopoulos, N., and Howe, R., "The role of force feedback in surgery: Analysis of blunt dissection," Proc. Proc. IEEE 10th symp. on haptic interfaces for virtual Envir&Teleoperator systems.
[185] Wagner, C. R., Lederman, S. J., and Howe, R. D., "A tactile shape display using RC servomotors," Proc. Proceedings HAPTICS, pp. 354-355.
[186] William M. Vannah, P. D. M. D., MD ; Jeffrey A . Hastings ; Joseph A . Stand, III;David M. Harning, CPO, 1999, "A method of residual limb stiffness distribution measurement," Journal of Rehabilitation Research and Development, 36(1), pp. 1-7.
[187] Woodall, P. H., 1926, Intra-Pelvic Technic OR Manipulative Surgery of the Pelvic Organs, Williams Publishing Co.
[188] X. Papademetris, A. J. S., D. P. Dione, R. T. Constable, and J. S., and Duncan, 2002, "Estimation of 3-D Left Ventricular Deformation From Medical
Images Using Biomechanical Models," IEEE Trans. on Medical
Imaging, 21(7), pp. 786-800.
[189] Xu, K., and Simaan, N., "Actuation Compensation for Flexible Surgical Snake-like Robots with Redundant Remote Actuation," Proc. Proc. IEEE Intl. Conf. Robot. and Automat., pp. 4148-4154.
[190] Y. H. Zweiri, L. D. S., K. Althoefer, 2004, "(Parameter Estimation for Excavator Arm Using Generalized Newton Method," IEEE Transactions on Robotics and Automation, pp. Vol. 20, No.24, pp.762-767.

[191] Y. Tillier, A. P., M. Durand-Reville, J. L. Chenot, 2003, "Three-dimensional finite element modelling for soft tissue surgery," International Congress Series 1256, pp. 349-355.
[192] Zheng Y P, M. A., 1996, "An ultrasound indentation system for biomechanical properties assessment of
soft tissues in-vivo," IEEE Trans. Biomed. Eng, 43, pp. 912–918.
[193] Zheng YP, C. Y., Wong K, Chan S, Mak AFT, 2000, "Biomechanical assessment of plantar foot tissue in diabetic patients using an ultrasound indentation system.," Ultrasound Med. Biol, 26, pp. 451–456.
[194] Zheng YP, L. Z., Choi APC, Lu MH, Chen X, Huang QH. , 2006, "Ultrasound palpation sensor for tissue thickness and elasticity measurement—assessment of transverse carpal ligament. ," Ultrasonics, 44, pp. e313–e317.
[195] Zheng YP, M. A. F. T., 1999, "Effective elastic properties for lower limb soft tissues from manual indentation experiment," IEEE Trans. Rehabil. Eng, 7, pp. 257–267.